

Next-to-Leading Log and Finite Quark Mass Effects with High Energy Jets at the LHC

James D Cockburn



Doctor of Philosophy
The University of Edinburgh
2017

Lay Summary

The startup of the Large Hadron Collider at CERN has marked the beginning of a new age of particle physics. We will have access to data about the most energetic particle collisions we have ever been able to produce. There are many hopes about what this data will reveal and a main one is that it will shed some light on how we can go beyond the Standard Model, which to date is our best theory for particle physics. The Standard Model has been incredibly successful but yet we know that it must be an incomplete theory because it fails to explain, for example, the force of gravity. There are a number of potential ways we could extend the Standard Model and all of them predict either the existence of new particles that we have not yet seen or predict some modifications to the properties of the particles we already know about; in many cases, both. In the latter case, these modifications can be very small and hard to detect and thus it is of paramount importance that we as a theory community provide accurate and precise predictions for how particles should behave within the bounds of the Standard Model.

In this thesis, we argue the usual method of how these predictions are made is not satisfactory when describing the collisions at such a high energy. Instead, we should think about how the calculation is done in a slightly different way which guarantees that these high energy considerations are correctly taken into account. This is done in a fairly straightforward way for most of the potential collisions at the Large Hadron Collider, but requires more effort and thought when it is being expanded to include more possibilities. It is this latter point that constitutes new work of the part of the author.

We show also that the formalism is simple enough that an approximation used in Higgs boson process no longer needs to be employed. This original result means we can therefore make predictions for this processes in a fundamentally new way.

Abstract

We discuss the properties of QCD amplitudes in the limit where all final state particles are well separated in rapidity. We study this limit in the context of the High Energy Jets (HEJ) formalism. This formalism *resums* terms in the perturbative expansion that go like $\log(\frac{s}{-t})$, which are enhanced in this limit. Such a region is reached already for modern day colliders such as the LHC and so capturing the contribution from these high energy logs is important in order to describe the data correctly. This is particularly important in, for example, VBF analyses where cuts are applied to pick out events with a large m_{jj} and in many BSM searches. Following on from this, we discuss two directions in which HEJ's accuracy has been improved.

Firstly, we look at adding descriptions of partonic subprocesses which are formally sub-leading in the jet cross section but LL in the particular subprocess itself. This required the derivation of new *effective vertices* that describe the emission of a quark/anti-quark pair in a way that is consistent with the resummation procedure. The inclusion of such processes means that HEJ is now less dependent on fixed-order calculations and that an important step towards full NLL accuracy has been achieved.

The second extension was to look at our description of events involving the emission of a Higgs boson along with jets. Specifically, we relax our requirement that the Higgs boson is produced with a rapidity that is far away from the rapidities of the accompanying jets and derive a new effective vertex from the study of the $qg \rightarrow qgH$ amplitude. Furthermore, the full dependence on the quark mass that appears in the loops connecting the gluons to the Higgs is kept, meaning that HEJ is unique in its ability to provide resummed predictions for this process with finite quark mass effects. The formalism is also simple enough to allow for extra final state jets in the process, a calculation that is currently beyond the reach of fixed order approaches.

Declaration

I declare that this thesis was composed by myself, that the work contained herein is my own except where explicitly stated otherwise in the text, and that this work has not been submitted for any other degree or professional qualification except as specified.

(James D Cockburn, 2017)

Acknowledgements

Thanks first and foremost must go to my wonderful parents who have never once discouraged me from following any path in life other than the one I wanted to go down. Without their constant love and support, I could never have got to where I am today. This thesis is as much theirs as it is mine and I hope they will find comfort in the fact that all my pondering has turned into something useful!

I also owe a great deal to the rest of the ‘PPT crew’ that started their PhD journeys at the same time as me. Andries, Gustav, Susi, James, Ava and slightly-late-to-the-party Rafa - thank you. You made the transition into PhD life very smooth, efficient and dare I say, a jolly good laugh. I’ve learnt so much from all of you over these past three-and-a-half years and I couldn’t have finished it without you.

The largest thank you I have to offer must go to my supervisor, Dr Jenni Smillie. I could not have asked for a more patient, willing, enthusiastic, fun and intelligent person to guide me. I have often suspected that I would not have had anywhere near as good a time doing my PhD if it was not for her. She has never made me feel inadequate or that I did not belong and having the visible belief of one’s supervisor is a huge part of successful postgraduate study.

Lastly, a huge thank you to the rest of the High Energy Jets collaboration of past and present - Jeppe, Jack, Helen, Andreas and Tuomas. Some combination of you were always there to answer any questions I ever had and your constant drive inspired me to persevere even when the going was tough.

Contents

Abstract	ii
Declaration	iii
Acknowledgements	iv
1 Background and Theoretical Basis	1
1.1 LHC and the Standard Model.....	1
1.2 QCD.....	3
1.2.1 Lagrangian Formalism and Dirac Fermions.....	3
1.2.2 Gauge Symmetry.....	5
1.2.3 QCD Lagrangian.....	8
1.3 From Lagrangians to Scattering Amplitudes.....	10
1.3.1 Path Integral Formulation.....	11
1.3.2 LSZ Formula.....	14
1.3.3 Correlation Functions from Path Integrals.....	17
1.3.4 Calculating a Scattering Amplitude.....	20
1.4 Feynman Rules (in QCD).....	22
1.4.1 $qQ \rightarrow qQ$ at Leading Order.....	26
1.5 Cross Sections in Proton-Proton Collisions.....	30

1.6	Spinor Helicity	33
2	High Energy Jets	41
2.1	The Problem with Perturbation Theory in the High Energy Limit..	41
2.1.1	$qQ \rightarrow qQ$ at LO and NLO in the High Energy Limit.....	43
2.2	HEJ Amplitudes	50
2.2.1	$gg \rightarrow gg$ in the High Energy Limit	50
2.2.2	Regge Theory and the Connection to High Energy $2 \rightarrow n$ Amplitudes	54
2.2.3	$qQ \rightarrow qgQ$ in the High Energy Limit.....	56
2.3	Resummation Technique	59
2.3.1	Lipatov Ansatz	60
2.3.2	Combining Real and Virtual Corrections at All Orders.....	61
2.4	Monte Carlo Implementation	63
2.4.1	The Motivation Behind Monte Carlo.....	64
2.4.2	Monte Carlo in High Energy Jets	67
2.4.3	Concerning Partons and Jets.....	69
2.4.4	Scale Variations.....	71
2.5	Experimental Analyses	72
3	Beyond Leading Log with High Energy Jets	76
3.1	Motivations for NLL	76
3.2	Unordered Emissions in Pure Jets.....	77
3.3	Calculations of NLL Partonic Subprocesses	80
3.3.1	Calculation of $gg \rightarrow qQ\bar{Q}$ in the High Energy Limit.....	80
3.3.2	Calculation of $qq' \rightarrow qQ\bar{Q}q'$ in the High Energy Limit	86

3.3.3	Checks and Verifications of Amplitudes	91
3.4	Computational Aspects	100
3.5	Results	101
4	Higgs Plus Jets with Finite Quark Mass Effects	108
4.1	The Infinite Top Mass Limit	108
4.2	Calculations of $H + \text{jets}$ with Finite Quark Mass Effects.....	111
4.2.1	$qQ \rightarrow qHQ$	111
4.2.2	$gq \rightarrow Hgq$	114
4.2.3	Checks and Verifications of Amplitudes	129
4.3	Computational Aspects	138
4.4	Results	138
5	Conclusions	146
A	Form of the H Functions in the $gq \rightarrow Hgq$ Box Integral	149
	Bibliography	156

List of Figures

(1.1)	The Standard Model of Particle Physics. Image sourced from the Wikipedia page on the Standard Model.	2
(1.2)	Example Feynman diagrams. The top-left diagram is called the s-channel, the top right the t-channel and the bottom the u-channel. All momenta flow from left to right.	25
(1.3)	Two quarks of different flavour scattering via the exchange of a gluon in the t-channel.	26
(1.4)	An example of a PDF set and how the value of the PDF changes depending on the scale probed. Figure from a review by the PDG [41]	32
(2.1)	Comparison of the full Leading Order calculation and the MRK limit of the process $ud \rightarrow ud$. A high value of Δ means that the final state particles are well separated in rapidity.	44
(2.2)	A selection of NLO diagrams for $qQ \rightarrow qQ$. We need only be interested in the bottom two.	45
(2.3)	By ‘cutting’ our NLO diagram like this, we can find the imaginary part of the amplitude by considering a product of LO diagrams.	47
(2.4)	The three diagrams (s , t , and u channels) for $qg \rightarrow qg$ scattering at LO.	51
(2.5)	A schematic representation of an example MRK amplitude. This figure is originally used in [6].	55
(2.6)	The five possibilities for an extra gluon emission. This figure is originally used in [6].	56
(2.7)	The emission of a gluon from a quark line. By taking the limit $k \ll p$, we obtain the Eikonal rule.	57

(2.8)	A schematic view of a HEJ amplitude. The original image is present in [7].	60
(2.9)	If the momentum p_2 is small enough, we cannot detect the gluon emission and so treat it as a real correction to the $2 \rightarrow 2$ process.	62
(2.10)	A square with sides of length $2R$ enclosing a circle of radius R . We can estimate the value of π by picking random points in the square and seeing whether or not they also lie in the circle.	65
(2.11)	The value of α_s as evaluated at different energy scales Q^2 . At low energies, the value becomes large enough that a perturbative treatment of QCD is no longer valid. Original figure is present in [29].	70
(2.12)	Differential cross section in m_{12} bins in the ATLAS study [12]	73
(2.13)	Differential cross section in HT (the scalar sum of all jet momenta) bins in a four jet ATLAS study [13]	74
(2.14)	Plot of an azimuthal decorrelation observable in average p_\perp in the ATLAS analysis [11].	75
(3.1)	A schematical view of an unordered emission amplitude.	78
(3.2)	Schematic diagram involving $g \rightarrow q\bar{q}$ impact factor.	81
(3.3)	All LO graphs for $qg \rightarrow qQ\bar{Q}$	82
(3.4)	Effective description of $qQ \rightarrow qq'\bar{q}'Q$	86
(3.5)	All LO graphs for $qq' \rightarrow qQ\bar{Q}q'$	87
(3.6)	Effective vertex approach to the $qg \rightarrow qQ\bar{Q}$ amplitude (red) compared to the full LO (green).	92
(3.7)	Effective vertex approach to the $qg \rightarrow qQ\bar{Q}$ amplitude (red) compared to the full LO (green) multiplied by the invariant mass of the quark/anti-quark pair.	93
(3.8)	Effective vertex approach to the $qq' \rightarrow qQ\bar{Q}q'$ amplitude (red) compared to the full LO (green).	94
(3.9)	Effective vertex approach to the $qq' \rightarrow qQ\bar{Q}q'$ amplitude (red) compared to the full LO (green) multiplied by the invariant mass of the quark/anti-quark pair.	94
(3.10)	Effective vertex approach to the $gg \rightarrow gQ\bar{Q}$ amplitude (red) compared to the full LO (green) multiplied by the invariant mass of the quark/anti-quark pair.	96

(3.11)	Effective vertex approach to the $qg \rightarrow qQ\bar{Q}g$ amplitude (red) compared to the full LO (green) multiplied by the invariant mass of the quark/anti-quark pair.	96
(3.12)	Effective vertex approach to the $gg \rightarrow gQ\bar{Q}g$ amplitude (red) compared to the full LO (green) multiplied by the invariant mass of the quark/anti-quark pair.	97
(3.13)	Effective vertex approach to the $qg \rightarrow qgQ\bar{Q}$ amplitude (red) compared to the full LO (green) multiplied by the invariant mass of the quark/anti-quark pair.	98
(3.14)	Effective vertex approach to the $qq' \rightarrow qgQ\bar{Q}q'$ amplitude (red) compared to the full LO (green) multiplied by the invariant mass of the quark/anti-quark pair.	99
(3.15)	Effective vertex approach to the $qq' \rightarrow qQ\bar{Q}qq'$ amplitude (red) compared to the full LO (green) multiplied by the invariant mass of the quark/anti-quark pair.	100
(3.16)	A breakdown of contributing parts to the jet cross section before (top) and after (bottom) implementing the effective vertex description of the new partonic subprocesses and the unordered events, in bins of the invariant mass between the most forward and backward jets.	104
(3.17)	Figure 6 of [9] redone with corrections included. The red lines are the results from running the full HEJ program, the green if one only considers the resummed parts of the program and black points are the data. From the top let; no corrections, unordered corrections, sub-leading partonic processes corrections, both corrections. In the last figure, we see how these corrections mean that there is barely any distinction between ‘resummed’ and ‘full’ HEJ anymore.	105
(3.18)	Figure 3a of [11] redone with corrections included. The red lines are the results from running the full HEJ program, the green if one only considers the resummed parts of the program and black points are the data. From the top let; no corrections, unordered corrections, sub-leading partonic processes corrections, both corrections. In the last figure, we see how these corrections mean that there is barely any distinction between ‘resummed’ and ‘full’ HEJ anymore.	106
(3.19)	Figure 4 of [13] redone with corrections included. From the top let; no corrections, unordered corrections, sub-leading partonic processes corrections, both corrections.	107

(4.1)	Diagrammatic representation of $qQ \rightarrow qHQ$ with an effective vertex for the production of the Higgs.	112
(4.2)	Diagrammatical representation of factorised $gq \rightarrow gHq$ expression.	115
(4.3)	A selection of LO graphs for $gq \rightarrow Hgq$	116
(4.4)	Comparison between the HEJ effective vertex, the full LO result and the result of the $qQ \rightarrow qHQ$ LO calculation reweighted by a colour factor for a central H in $gq \rightarrow Hgq$ with full top mass dependence.	130
(4.5)	Comparison between the HEJ effective vertex, the full LO result and the result of the $qQ \rightarrow qHQ$ LO calculation reweighted by a colour factor for an outside H in $gq \rightarrow Hgq$ with full top mass dependence.	131
(4.6)	Comparison of infinite top, finite top and finite top plus finite bottom HEJ matrix elements with a central Higgs.	132
(4.7)	Comparison of infinite top, finite top and finite top plus finite bottom HEJ matrix elements with an outside Higgs.	132
(4.8)	Comparison between the HEJ effective vertex and the full LO result of the $gu \rightarrow Hgggu$ amplitude for a forward H with an infinite top mass.	134
(4.9)	Comparison between the HEJ effective vertex and the full LO result of the $gu \rightarrow gHgu$ amplitude for a central H with an infinite top mass.	135
(4.10)	Comparison between the HEJ effective vertex and the full LO result of the $gg \rightarrow Hggg$ amplitude for a forward H with an infinite top mass.	136
(4.11)	Comparison between the HEJ effective vertex and the full LO result of the $gg \rightarrow gHgg$ amplitude for a central H next to the extremal forward parton with an infinite top mass.	136
(4.12)	Comparison between the HEJ effective vertex and the full LO result of the $gg \rightarrow ggHg$ amplitude for a central H next to the extremal backward parton with an infinite top mass.	137
(4.13)	Comparison between the HEJ effective vertex and the full LO result of the $gg \rightarrow gggH$ amplitude for a backward H with an infinite top mass.	137
(4.14)	Comparison of infinite top mass, finite top mass and finite top + bottom mass cross sections in $gu \rightarrow guH$, binned in Higgs p_T . . .	140

(4.15)	Comparison of infinite top mass, finite top mass and finite top + bottom mass cross sections in $gu \rightarrow guH$, binned in rapidity difference between the gluon and up quark	140
(4.16)	Cross section breakdown in $gg \rightarrow ggH$ into forward Higgs production. backward Higgs production and central Higgs with infinite top mass.	141
(4.17)	Comparison of infinite top mass, finite top mass and finite top + bottom mass cross sections in $gg \rightarrow ggH$, binned in Higgs p_T . .	142
(4.18)	Comparison of infinite top mass, finite top mass and finite top + bottom mass cross sections in $gg \rightarrow ggH$, binned in rapidity difference between the gluon and up quark.	142
(4.19)	Comparison of infinite top mass, finite top mass and finite top + bottom mass cross sections in $gg \rightarrow gggH$, binned in Higgs p_T . .	143
(4.20)	Comparison of infinite top mass, finite top mass and finite top + bottom mass cross sections in $gg \rightarrow gggH$, binned in the maximum p_T of a gluon entering into the Higgs vertex.	144
(4.21)	Comparison of infinite top mass, finite top mass and finite top + bottom mass cross sections in $pp \rightarrow H + \geq 2j$, binned in the p_T of the Higgs.	145
(4.22)	Comparison of infinite top mass, finite top mass and finite top + bottom mass cross sections in $pp \rightarrow H + \geq 2j$, binned in the rapidity difference between the most forward/backward jets. . . .	145

List of Tables

(1.1) QCD Feynman Rules for propagators and vertices	27
(2.1) Estimates of π via a simple Python Monte Carlo program for different numbers of trials.	65

Todo list

Make last figure prettier - longer, less wide, better labelling 103

Chapter 1

Background and Theoretical Basis

In this section, we present an overview of Particle Physics and Quantum Field Theory (QFT) upon which the work contained in this thesis depends. We begin by discussing the Standard Model (SM) of Particle Physics and how modern experiments at the Large Hadron Collider (LHC) test it. We then focus on Quantum Chromodynamics (QCD), which is the part of the SM that describes the interactions of quarks and gluons, the fundamental particles that come together to form protons, neutrons and a whole range of other composite particles [41]. Finally, we delve into the Spinor Helicity formalism [28] to introduce notation and derive results which will allow for a simple and clear method of doing the work presented in the later chapters of this thesis.

1.1 LHC and the Standard Model

The SM, shown in figure 1.1, is currently our best theoretical model for understanding the fundamental particles of nature and their interactions. It is also one of the most rigorously tested models in the history of physics and to date it has stood up to all the tests thrown at it [27]. For instance, the measurement of the anomalous magnetic dipole moment of the electron agrees with that predicted by the model to ten significant figures [8]. Despite these successes, however, we know that the SM cannot be a *complete* model of our universe. For instance, it does not include gravity in its formulation. On top of that, cosmological measurements like that of the velocities of spinning



Figure 1.1 *The Standard Model of Particle Physics. Image sourced from the Wikipedia page on the Standard Model.*

galaxies and the expansion rate of the universe imply that there is a whole other sector we are currently ignorant of; that of Dark Matter and Dark Energy [14]. Indeed, some estimates imply that approximately 96% of the universe consists of these mysterious quantities [39]. Clearly, we need to find a way forward in order to develop a theory ‘Beyond the Standard Model’ that can describe them. One possibility is that non-SM particles could interact with SM particles in a manner whereby we would need to be able to calculate SM predictions to a large degree of precision to be able to determine if there are there. Theorists and experimentalists must continue to come together in order to face this challenge; theorists by improving how calculations are conducted and experimentalists by reducing experimental uncertainties and collecting ever more data.

The LHC has given physicists the opportunity to probe the SM at the highest energies yet, ultimately being able to reach a centre-of-mass energy of 14 TeV. This is approximately 7 times higher than what was achievable at its spiritual predecessor, the Tevatron at Fermilab [38]. The headline story for the LHC, of course, was its discovery of the Higgs boson in 2012, the physical remnant of

‘Electroweak Symmetry Breaking’ (EWSB) [10, 36]. In effect, the masses of the fundamental particles are generated via interactions with the Higgs field and so it is often said that the discovery of the Higgs is the discovery of the ‘origin of mass’. At this stage, we do not know whether the Higgs boson that has been discovered is exactly the one as predicted by the Standard Model. Much more research now needs to be done in order to determine its fundamental properties, such as the strength of its coupling to the massive gauge bosons, before we can know one way or the other. This presents the very exciting theoretical challenge of providing accurate predictions for Higgs processes, and Chapter 4 of this thesis will dive into this issue further. The theory that we will mostly concern ourselves with, however, is not that of EW physics but rather QCD. The following sections will provide an overview of the theory in order to discuss some important aspects and also to provide a basic introduction to QFT, which underpins the entirety of the SM.

1.2 QCD

QCD is described by a non-Abelian $SU(3)$ gauge group within the SM and provides the theoretical underpinning for the *strong interaction*, the interaction between *quarks* and *gluons*. This then confines our study to the purple area and the very top of the red area shown in figure 1.1. This may seem restrictive, but because the LHC collides protons which consist of quarks and gluons, it is clearly QCD that is the underlying theory we need to use to understand the collisions that happen there.

1.2.1 Lagrangian Formalism and Dirac Fermions

We temporarily delay discussing how the Lagrangian is used in particle physics (QCD in particular for this thesis) so as to review the background of the formalism. The fundamental quantity is the *action*, the time integral of the Lagrangian L ;

$$S = \int L dt. \tag{1.1}$$

In a local field theory, we can write the Lagrangian as an integral over all space of

the *Lagrangian Density*, \mathcal{L} , which can depend on a set of fields and the derivatives of those fields, $\mathcal{L} = \mathcal{L}(\phi_i, \partial_\mu \phi_i)$. From this point onwards, we will refer to the ‘Lagrangian density’ as just the ‘Lagrangian’. We therefore have;

$$S = \int \mathcal{L}(\phi_i, \partial_\mu \phi_i) dt d^3x = \int \mathcal{L}(\phi_i, \partial_\mu \phi_i) d^4x, \quad (1.2)$$

where we note that we work in units such that $c = \hbar = 1$. The *principle of least action* states that as a system evolves from one configuration to another, it does so in a way that minimises the action; $\delta S = 0$. By considering a small change on the right-hand side of the previous equation, we arrive at the famous *Euler-Lagrange* equation of motion;

$$\partial_\mu \left(\frac{\partial \mathcal{L}}{\partial(\partial_\mu \phi_i)} \right) - \frac{\partial \mathcal{L}}{\partial \phi_i} = 0. \quad (1.3)$$

Our QCD field content is quarks and gluons, so they must be included in the Lagrangian in such a way that the appropriate equations of motion are recovered from it. We will begin with quarks. They are fermionic particles and so (when not interacting or ‘free’) will obey the Dirac equation;

$$(i\cancel{\partial} - m)\psi(x) = 0, \quad (1.4)$$

where $\cancel{\partial} = \gamma^\mu \partial_\mu$ and m is the mass of the quark. Suppressed here is the fact that this is actually a matrix equation in spinor space; ψ is a four-component spinor vector and the γ^μ are a set of four-by-four matrices with the anti-commutation relation $\{\gamma^\mu, \gamma^\nu\} = 2\eta^{\mu\nu}$. An explicit form for the matrices γ^μ will be presented later in the chapter since it is not necessary to have one at this point. We introduce a conjugate field $\bar{\psi}(x) = \psi^\dagger(x)\gamma^0$ and write a Lagrangian;

$$\mathcal{L} = \bar{\psi}(x)(i\cancel{\partial} - m)\psi(x), \quad (1.5)$$

where now we can evaluate the Euler-Lagrange equation taking $\bar{\psi}$ as our field to vary to yield the Dirac equation for ψ , as we wanted. The reason $\bar{\psi}$ is used as a conjugate field as opposed to the more obvious ψ^\dagger comes from the requirement that the Lagrangian is invariant under a Lorentz transformation; in other words, \mathcal{L} is a Lorentz scalar. We could also, of course, take the variation

of this Lagrangian with respect to ψ and doing so we get;

$$\bar{\psi}(x)(i\cancel{\partial} + m) = 0, \quad (1.6)$$

which is the same equation in Hermitian conjugate form. The Dirac equation has plane wave solutions of the form;

$$\psi(x) = u(\vec{p}) e^{-ip \cdot x} + v(\vec{p}) e^{ip \cdot x}, \quad (1.7)$$

where p is the four-momentum and \vec{p} the three-momentum. In practice it is the u and v spinors that are used in calculations and they are interpreted as describing fermions and anti-fermions respectively. One of the great successes of the Dirac equation was that it predicts the existence of anti-fermions. Imagine that we are in a frame such that $\vec{p} = 0$. Since $p \cdot x = Et - \vec{p} \cdot \vec{x}$ and $E = \sqrt{\vec{p}^2 + m^2}$, then the second term in equation 1.7 will have an exponential e^{imt} - a state with negative energy¹. Because Quantum Mechanics requires a complete set of basis states, we can't simply throw the solution away as 'unphysical'. The solutions have to be interpreted as either positive energy fermions moving backwards in time or negative energy anti-fermions moving forward in time. We will see later how the former interpretation lends itself rather neatly to a graphical representation of scattering involving fermionic particles. In any case, subbing this form for $\psi(x)$ into the Dirac equation, we find the following conditions;

$$(\cancel{\partial} - m)u(\vec{p}) = 0, \quad (1.8a)$$

$$(\cancel{\partial} + m)v(\vec{p}) = 0. \quad (1.8b)$$

1.2.2 Gauge Symmetry

We briefly mentioned that QCD is a gauge theory with gauge group $SU(3)$. This is a non-abelian group, which we will see later leads to a whole host of interesting effects. For the time being, however, we will switch to the abelian group $U(1)$,

¹To be more precise about it, the sign of i chosen in the Schrödinger equation was a matter of convention and so strictly speaking it's not just the sign of the exponential that determines that this is an anti-fermion. Rather, it is because we have *both* plus and minus sign solutions and we are required to consider both of them.

which is actually the group we need for describing Quantum Electrodynamics (QED). The reason for this is so that we can derive some results in this simpler case which will allow us to jump to the more complicated $SU(3)$ easier. In either case, the symmetry we require in the Lagrangian is that it is unchanged if we redefine our charges according to a group transformation, $\psi \rightarrow U\psi$. For a global redefinition where our operator U does not depend on x , this is trivially true since the U s are by definition unitary. However, if we generalise to a local redefinition;

$$\begin{aligned}\mathcal{L}' &= \bar{\psi}(x)U^\dagger(x)(i\not{\partial} - m)U(x)\psi(x) \\ &= \bar{\psi}(x)(i\not{\partial} - m)\psi(x) + i\bar{\psi}(x)U^\dagger(x)\gamma^\mu [\partial_\mu U(x)]\psi(x) \neq \mathcal{L}.\end{aligned}\tag{1.9}$$

The problem has appeared because of the derivative in our Lagrangian. What we would like is a different derivative term that includes the partial derivative but along with an extra part to cancel away the extra term we picked up. Equivalently, we search for a so-called *covariant derivative* that transforms as;

$$D'_\mu = U(x)D_\mu U^\dagger(x).\tag{1.10}$$

Such an object can be constructed, but we have to introduce another field, A_μ , that transforms non-trivially. Before we do so, however, let's take the specific example of the $U(1)$ group and evaluate explicitly what the extra term we need to remove looks like. If we call the group generator Λ , then;

$$U(x) = e^{iq\Lambda(x)},\tag{1.11}$$

where q is an overall scale factor, which is associated with the group charge. Then the extra term is proportional to;

$$\partial_\mu U(x) = iq(\partial_\mu \Lambda(x))e^{iq\Lambda(x)}.\tag{1.12}$$

Let us then define our covariant derivative in the following way;

$$D_\mu = \partial_\mu + iqA_\mu(x).\tag{1.13}$$

Then, under the gauge transformation;

$$\begin{aligned} D'_\mu \psi'(x) &= (\partial_\mu + iqA'_\mu(x))e^{iq\Lambda(x)}\psi(x) \\ &= U(x)(\partial_\mu + iq[A'_\mu(x) + (\partial_\mu\Lambda(x))])\psi(x), \end{aligned} \quad (1.14)$$

and therefore we can recover invariance so long as;

$$A'_\mu(x) = A_\mu(x) - \partial_\mu\Lambda(x), \quad (1.15)$$

which we recognise precisely as a gauge transformation of the vector potential A^μ . The process of constructing a covariant derivative in this manner is called the *principle of minimal coupling* and allows us to construct it in any given gauge group. Thus, we simply replace the partial derivative in our Lagrangian with the covariant derivative to get a locally gauge invariant Lagrangian;

$$\begin{aligned} \mathcal{L}_{Dirac+Interaction} &= \bar{\psi}(x)(i\not{D} - m)\psi(x) \\ &= \bar{\psi}(x)(i\not{\partial} - m)\psi(x) + iq\bar{\psi}(x)\not{A}(x)\psi(x). \end{aligned} \quad (1.16)$$

From the requirement of local gauge invariance alone, we see from the second term that there is necessarily an interaction between our matter content and our gauge bosons. However, our current form of the Lagrangian doesn't yet describe the dynamics of the gauge field itself and so we should add that in. We know that such a term must be gauge and Lorentz invariant so let's attempt to construct an additional object that satisfies these symmetries from our new field. Consider what would happen if we included a derivative of the field A_μ in our formalism and applied the gauge transformation;

$$\partial'_\mu A'_\nu(x) = \partial_\mu(A_\nu(x) - \partial_\nu\Lambda(x)). \quad (1.17)$$

This is clearly not gauge invariant, but if we take a combination anti-symmetric

in μ, ν ;

$$\begin{aligned}\partial'_\mu A'_\nu(x) - \partial'_\nu A'_\mu(x) &= \partial_\mu(A_\nu(x) - \partial_\nu\Lambda(x)) - \partial_\nu(A_\mu(x) - \partial_\mu\Lambda(x)) \\ &= \partial_\mu A_\nu(x) - \partial_\nu A_\mu(x) \equiv F_{\mu\nu},\end{aligned}\tag{1.18}$$

where the last line follows from the fact that derivatives commute with each other. The object $F_{\mu\nu}$ is called the *field strength tensor* and notice that we could also have constructed it the following way;

$$F_{\mu\nu} = -\left(\frac{i}{q}\right)[D_\mu, D_\nu],\tag{1.19}$$

which is a form that will be useful when generalising to other gauge groups. The last requirement is to insert this into our Lagrangian in a Lorentz invariant fashion² and also make explicit that there are potentially many fermions that can interact with the $U(1)$ gauge bosons in this way;

$$\mathcal{L}_{QED} = \sum_{f \in \text{flavours}} \bar{\psi}_f(x)(i\not{D} - m)\psi_f(x) - \frac{1}{4}F_{\mu\nu}F^{\mu\nu},\tag{1.20}$$

where we have added an arbitrary normalisation factor to our new term for convenience.

1.2.3 QCD Lagrangian

The question of how to go from QED to QCD is equivalent to the question of what extra considerations need to be made if we work with the group $SU(3)$ rather than $U(1)$. The first difference is that $SU(3)$ has $3^2 - 1 = 8$ generators and so 8 independent rotation directions for our operator U . Thus, a (local) group transformation will have the form;

$$U(x) = e^{ig_s\Lambda^a(x)t^a},\tag{1.21}$$

²Actually, we should really also include a term $\sim \epsilon^{\alpha\beta\mu\nu}F_{\alpha\beta}F_{\mu\nu}$ since this too is Lorentz invariant, but such a term is parity violating and this thesis will only concern itself only with theories that are parity-symmetric.

where t^a are the generators of the group. Additionally, in the fundamental representation of $SU(3)$, the Dirac spinors must be a 3-vector;

$$\psi = \begin{pmatrix} q^r \\ q^b \\ q^g \end{pmatrix}, \quad (1.22)$$

where q is a specific flavour of quark (the entire theory has all of them, of course) and r, g, b are colour labels, denoting the $SU(3)$ charge (or, more simply, the ‘colour charge’). Now we apply the principle of minimal coupling from the previous section to find a covariant derivative for this gauge group, being explicit with our colour space notation;

$$D_\mu = \partial_\mu \mathbb{1} + ig_s t^a A_\mu^a(x). \quad (1.23)$$

Each of the 8 gauge fields has to transform in the same way as before so as to make the covariant derivative perform its function correctly;

$$A_\mu^{a'} = A_\mu^a + \partial_\mu \Lambda^a(x), \quad (1.24)$$

and the final step is to construct the field strength tensor;

$$\begin{aligned} F_{\mu\nu} &= - \left(\frac{i}{g_s} \right) [D_\mu, D_\nu] \\ &= - \left(\frac{i}{g_s} \right) [\partial_\mu + ig_s A_\mu^a t^a, \partial_\nu + ig_s A_\nu^b t^b] \\ &= [A_\mu^a t^a, \partial_\nu] + [\partial_\mu, A_\nu^b t^b] + ig_s A_\mu^a A_\nu^b [t^a, t^b] \\ &= A_\mu^a t^a \partial_\nu - (\partial_\nu A_\mu^a) t^a + (\partial_\mu A_\nu^b) t^b - A_\nu^b t^b \partial_\mu + ig_s A_\mu^a A_\nu^b [t^a, t^b] \\ &= t^c (\partial_\mu A_\nu^c - \partial_\nu A_\mu^c) + ig_s A_\mu^a A_\nu^b (if^{abc} t^c) \\ &= t^a (\partial_\mu A_\nu^a - \partial_\nu A_\mu^a - g_s A_\mu^b A_\nu^c f^{abc}) \\ &= t^a F_{\mu\nu}^a, \end{aligned} \quad (1.25)$$

where the f^{abc} are the structure constants of $SU(3)$. The non-abelian nature has introduced an extra term alongside the derivatives in the field strength tensor and this has an interesting physical consequence; namely, that our Lagrangian

will contain terms where the gauge bosons can interact with each other. This extra term has another immediate consequence; $F_{\mu\nu}$ is no longer gauge invariant. Indeed;

$$\begin{aligned}
F'_{\mu\nu} &= -\left(\frac{i}{g_s}\right) [D'_\mu, D'_\nu] \\
&= -\left(\frac{i}{g_s}\right) [UD_\mu U^\dagger, UD_\nu U^\dagger] \\
&= -\left(\frac{i}{g_s}\right) U[D_\mu, D_\nu]U^\dagger \\
&= UF_{\mu\nu}U^\dagger,
\end{aligned} \tag{1.26}$$

and unlike the Abelian case, we cannot simply pass the U s through the field strength tensor because of the non-commuting generators. We see that actually the invariant quantity is the *trace* in colour space;

$$tr(F'_{\mu\nu}) = tr(UF_{\mu\nu}U^\dagger) = tr(F_{\mu\nu}U^\dagger U) = tr(F_{\mu\nu}). \tag{1.27}$$

Remembering our need for our Lagrangian to be a Lorenz scalar as well, we are now in a position to write down the Lagrangian for QCD;

$$\mathcal{L}_{QCD} = \sum_{f \in \text{flavours}} \sum_{i,j=1}^3 \bar{q}_f^i(x)(i\not{D} - m_f)_{ij}q_f^j(x) - \frac{1}{2}tr(F_{\mu\nu}F^{\mu\nu}). \tag{1.28}$$

1.3 From Lagrangians to Scattering Amplitudes

In the last section, we showed by considering symmetries we want our theory to have and the equations of motion for our fields that we were able to write down a Lagrangian. What we have not yet explained is why that was useful. Here, we provide an overview of the *path integral formalism* for QFT which will provide us with a way of computing *scattering amplitudes* in our field theory.

1.3.1 Path Integral Formulation

We will consider non-relativistic Quantum Mechanics as our starting point for the derivation of the Path Integral formalism. The results we obtain in this regime will be immediately generalisable to a QFT so we lose nothing by considering this. The motivating principle behind the Path Integral is to try and calculate the transition amplitude between two general quantum mechanical states. If the states are completely defined by a set of co-ordinates $\{q^i\} = q$, then the transition amplitude from a state q_a at time zero to q_b at time T is;

$$A(q_a, q_b; T) = \langle q_b; t = T | q_a; t = 0 \rangle. \quad (1.29)$$

From solving the Schrödinger equation, we know that there is a unitary operator that takes a state at one time and evolves it to another time under the influence of a time-independent Hamiltonian operator \hat{H} ;

$$\hat{U}(t - t_0) = e^{-i\hat{H}(t-t_0)}. \quad (1.30)$$

Our transition amplitude can then be written;

$$A(q_a, q_b; T) = \langle q_b | \hat{U}(T) | q_a \rangle = \langle q_b | e^{-i\hat{H}T} | q_a \rangle. \quad (1.31)$$

Let us now break the problem up in time. We split up the time interval T into n equal elements $\varepsilon = T/n$ such that the operator for the full time span is made up of the continual application of an operator evolving the state in steps of ε ; $\hat{U}(T) = \hat{U}(\varepsilon)^n$. Along with this, we will also insert $n - 1$ identity operators $\mathbb{1} = \int dq_j |q_j\rangle \langle q_j|$, allowing us to write our amplitude as;

$$A(q_a, q_b; T) = \int \prod_{j=1}^{n-1} (dq_j) \langle q_b | e^{-i\hat{H}\varepsilon} | q_{n-1} \rangle \cdots \langle q_{i+1} | e^{-i\hat{H}\varepsilon} | q_i \rangle \cdots \langle q_1 | e^{-i\hat{H}\varepsilon} | q_a \rangle. \quad (1.32)$$

We now take n to be large and expand one of the matrix elements in this product

in ε ;

$$\langle q_{i+1} | e^{-i\hat{H}\varepsilon} | q_i \rangle = \langle q_{i+1} | 1 - i\varepsilon\hat{H} + \mathcal{O}(\varepsilon^2) | q_i \rangle. \quad (1.33)$$

Consider a Hamiltonian of the form $\hat{H} = \hat{K}(\hat{p}) + \hat{V}(\hat{q})$, that is, a Hamiltonian with a kinetic term depending only on the momenta of the system, p , and a potential that depends only on the co-ordinates q . Taking just the potential term, we see the matrix element 1.33 is;

$$\begin{aligned} \langle q_{i+1} | \hat{V}(\hat{q}) | q_i \rangle &= V(q_i) \delta(q_i - q_{i+1}) \\ &= V\left(\frac{q_i + q_{i+1}}{2}\right) \int \frac{dp_i}{2\pi} e^{ip_i(q_{i+1} - q_i)}, \end{aligned} \quad (1.34)$$

where the potential has been democratically evaluated at the average of the two points. For the kinetic part, we must insert a complete set of momentum eigenstates for it to act upon;

$$\begin{aligned} \langle q_{i+1} | \hat{K}(\hat{p}) | q_i \rangle &= \int \frac{dp_i}{2\pi} \langle q_{i+1} | \hat{K}(\hat{p}) | p_i \rangle \langle p_i | q_i \rangle \\ &= \int \frac{dp_i}{2\pi} K(p_i) \langle q_{i+1} | p_i \rangle \langle p_i | q_i \rangle \\ &= \int \frac{dp_i}{2\pi} K(p_i) e^{iq_{i+1}p_i} e^{-iq_i p_i} \\ &= \int \frac{dp_i}{2\pi} K(p_i) e^{ip_i(q_{i+1} - q_i)}. \end{aligned} \quad (1.35)$$

Therefore, our form for the Hamiltonian allows us to write;

$$\langle q_{i+1} | \hat{H}(\hat{q}, \hat{p}) | q_i \rangle = \int \frac{dp_i}{2\pi} H\left(\frac{q_i + q_{i+1}}{2}, p_i\right) e^{ip_i(q_{i+1} - q_i)}. \quad (1.36)$$

Such a formula is not correct in general, however. The left-hand side depends on the non-commuting operators \hat{q} , \hat{p} and the right-hand side only on the eigenvalues of these operators. If our Hamiltonian were to contain terms that depend on both of these operators in some general order then we would expect to get different physics based on how exactly those operators are ordered. We can get around

this by requiring that our Hamiltonian is in *Weyl ordered* form, which is the form that by definition yields the equality 1.36. Any general Hamiltonian can be brought into this form by use of the commutation relation $[\hat{q}, \hat{p}] = i$. For example, say the Hamiltonian had an operator like $\hat{q}\hat{p}$;

$$\begin{aligned}\hat{q}\hat{p} &= \frac{1}{2}(\hat{q}\hat{p} + \hat{q}\hat{p}) \\ &= \frac{1}{2}(\hat{q}\hat{p} + \hat{p}\hat{q} + i) \\ &= \hat{H}(\hat{q}\hat{p}, \hat{p}\hat{q})_{WO} + \frac{i}{2}.\end{aligned}\tag{1.37}$$

We see from this that a Weyl ordered Hamiltonian has the property that the operators \hat{q}, \hat{p} appear in a symmetric fashion. We therefore have for any Weyl ordered Hamiltonian and small ε ;

$$\langle q_{i+1} | e^{-i\varepsilon \hat{H}(\hat{q}, \hat{p})_{WO}} | q_i \rangle = \int \frac{dp_i}{2\pi} e^{-i\varepsilon H\left(\frac{q_i + q_{i+1}}{2}, p_i\right)} e^{ip_i(q_{i+1} - q_i)}.\tag{1.38}$$

Putting this in for every matrix element 1.33 in 1.32, then;

$$\begin{aligned}A(q_a, q_b; T) &= \int \prod_{j=1}^{n-1} \left(\frac{dp_j dq_j}{2\pi} e^{-i\varepsilon H\left(\frac{q_j + q_{j+1}}{2}, p_j\right)} e^{ip_j(q_{j+1} - q_j)} \right) \\ &= \int \prod_{j=1}^{n-1} \left(\frac{dp_j dq_j}{2\pi} \right) \exp \left(i\varepsilon \sum_{j=1}^{n-1} \left[p_j \left(\frac{q_{j+1} - q_j}{\varepsilon} \right) - H \left(\frac{q_j + q_{j+1}}{2}, p_j \right) \right] \right).\end{aligned}\tag{1.39}$$

If we now formally take the limit $n \rightarrow \infty$ (and so $\varepsilon \rightarrow 0$), then $(q_{i+1} - q_i)/\varepsilon \rightarrow \dot{q}$, our discrete sum in the exponential goes over to an integral with measure dt and our p_j, q_j integrals become *Path Integrals*;

$$A(q_a, q_b; T) = \int \mathcal{D}q(t) \mathcal{D}p(t) \exp \left(i \int_0^T dt [p\dot{q} - H(q, p)] \right).\tag{1.40}$$

The way to interpret the path integral here is that it is an integration over all paths in phase space with the boundary conditions $q(0) = q_a$ and $q(T) = q_b$ (note

there is no constraint on the momenta p at the endpoints). It is precisely the integration measure in 1.39 evaluated at each point in time. The integral over p can be done by considering the stationary points of it, which is where;

$$\dot{q} - \frac{\partial H}{\partial p} = 0 \rightarrow \dot{q} = \frac{\partial H}{\partial p}. \quad (1.41)$$

We can solve this differential equation for p in terms of q, \dot{q} and so we are left with;

$$\begin{aligned} A(q_a, q_b; T) &= \int \mathcal{D}q(t) \exp \left(i \int_0^T dt [p(q, \dot{q})\dot{q} - H(q, \dot{q})] \right) \\ &= \int \mathcal{D}q(t) \exp \left(i \int_0^T dt L(q, \dot{q}) \right) \\ &= \int \mathcal{D}q(t) \exp (iS). \end{aligned} \quad (1.42)$$

We therefore see that knowing the Lagrangian for a system in principle allows for us to calculate path integrals in the theory. We can immediately generalise the result we have here to QFT, where instead of the co-ordinates q, \dot{q} we have a dependence on a field, ϕ , and the derivative of the field, $\partial_\mu \phi$, and our boundary conditions relate to specific configurations of the fields ϕ_a, ϕ_b ;

$$A(\phi_a, \phi_b; T) = \int \mathcal{D}\phi \exp \left(i \int_0^T d^4x \mathcal{L}(\phi, \partial_\mu \phi) \right). \quad (1.43)$$

1.3.2 LSZ Formula

In QFT calculations, we will work with well-defined in and out states which are states containing a set number of known particles. In order to construct these states, we first have to quantise our fields. The method to do this is called *canonical quantisation* and a full description of this will not be given here. The interested reader should consult the excellent discussion in [42] or [46]. The upshot is that our field ψ is upgraded to a quantum mechanical operator $\hat{\psi}$ which creates particles with well-defined momentum. Since we are going to work with

fermions, we quantise the Dirac field 1.7;

$$\hat{\psi}(x) = \int \frac{d^3\vec{p}}{(2\pi)^3 2E_{\vec{p}}} \sum_{s \in \text{spins}} \left[\hat{a}_s(\vec{p}) u^{(s)} e^{-ip \cdot x} + \hat{b}_s^\dagger(\vec{p}) v^{(s)}(\vec{p}) e^{ip \cdot x} \right], \quad (1.44)$$

along with the corresponding equation for the conjugate field $\bar{\psi}$. We can interpret the operator $\hat{a}_s(\vec{p})(\hat{b}_s^\dagger(\vec{p}))$ as the operator that destroys (creates) a particle (anti-particle) with momentum \vec{p} and spin s . We can invert this equation to find forms for these operators in terms of the fields;

$$\hat{a}_s^\dagger(\vec{p}) = \int d^3x e^{-ip \cdot x} \bar{\psi}(x) \gamma^0 u^{(s)}(\vec{p}), \quad (1.45a)$$

$$\hat{b}_s^\dagger(\vec{p}) = \int d^3x e^{-ip \cdot x} \bar{\psi}^{(s)}(\vec{p}) \gamma^0 \psi(x). \quad (1.45b)$$

All of these results are only valid for a free theory, so we need a way to relate them to an interacting theory. If we measure our incoming state well before the scattering takes place, we can expect our field to behave as a free field. A similar statement applies to the final state long after the scattering. In other words, we can create these results for our operators as the limit of a more general, time-dependent operator;

$$\hat{a}^\dagger(\vec{p}) = \lim_{t \rightarrow \pm\infty} \hat{a}^\dagger(\vec{p}, t), \quad (1.46)$$

where the operators are now *defined* through 1.45. For simplicity, we now consider a process where two fermions interact in the initial state to yield two fermions in the final state, but the results we obtain will clearly be immediately generalisable to $2 \rightarrow n$ scattering. We construct our initial and final states in the following way;

$$|i\rangle = \lim_{t \rightarrow -\infty} \hat{a}^\dagger(\vec{p}_1, t) \hat{a}^\dagger(\vec{p}_2, t) |0\rangle, \quad (1.47a)$$

$$|f\rangle = \lim_{t \rightarrow +\infty} \hat{a}^\dagger(\vec{k}_1, t) \hat{a}^\dagger(\vec{k}_2, t) |0\rangle, \quad (1.47b)$$

where $|0\rangle$ is the vacuum state with no particles present. The object we are

interested in computing is;

$$\begin{aligned}\langle f|i\rangle &= \langle 0|\hat{a}(\vec{k}_1, \infty)\hat{a}(\vec{k}_2, \infty)\hat{a}^\dagger(\vec{p}_1, -\infty)\hat{a}^\dagger(\vec{p}_2, -\infty)|0\rangle \\ &= \langle 0|T\left(\hat{a}(\vec{k}_1, \infty)\hat{a}(\vec{k}_2, \infty)\hat{a}^\dagger(\vec{p}_1, -\infty)\hat{a}^\dagger(\vec{p}_2, -\infty)\right)|0\rangle,\end{aligned}\quad (1.48)$$

where T is a time-ordering operator, placing all operators at larger times to the left of the expression. We aim to express this formula in terms of the field ψ . In order to do so, consider the object;

$$\begin{aligned}\hat{a}^\dagger(\vec{p}, \infty) - \hat{a}^\dagger(\vec{p}, -\infty) &= \int_{-\infty}^{+\infty} dt \partial_0 a^\dagger(\vec{p}, t) \\ &= \int dt \int d^3x \partial_0 \left(e^{-ip \cdot x} \bar{\psi}(x) \gamma^0 u^{(s)}(\vec{p}) \right) \\ &= \int d^4x \bar{\psi}(x) \left(\overleftarrow{\partial}_0 - ip_0 \right) \gamma^0 e^{-ip \cdot x} u^{(s)}(\vec{p}) \\ &= \int d^4x \bar{\psi}(x) \left(\overleftarrow{\partial}_0 \gamma^0 + ip_j \gamma^j - im \right) e^{-ip \cdot x} u^{(s)}(\vec{p}) \quad (1.49) \\ &= \int d^4x \bar{\psi}(x) \left(\overleftarrow{\partial}_0 \gamma^0 - \overrightarrow{\partial}_j \gamma^j - im \right) e^{-ip \cdot x} u^{(s)}(\vec{p}) \\ &= \int d^4x \bar{\psi}(x) \left(\overleftarrow{\partial}_0 \gamma^0 + \overleftarrow{\partial}_j \gamma^j - im \right) e^{-ip \cdot x} u^{(s)}(\vec{p}) \\ &= (-i) \int d^4x \bar{\psi}(x) \left(i \overleftarrow{\not{\partial}} + m \right) e^{-ip \cdot x} u^{(s)}(\vec{p}),\end{aligned}$$

where we used $(\not{p} - m)u(\vec{p}) = 0$ in the fourth line and integration by parts in the second-to-last line. Notice that the factor in the last integral is precisely the one we get from the equation of motion for $\bar{\psi}$ and so the integral would be zero in the free theory as we would expect. The upshot of this calculation is that;

$$\hat{a}^\dagger(\vec{p}, -\infty) = \hat{a}^\dagger(\vec{p}, \infty) + i \int d^4x \bar{\psi}(x) \left(i \overleftarrow{\not{\partial}} + m \right) e^{-ip \cdot x} u^{(s)}(\vec{p}), \quad (1.50)$$

and via Hermitian conjugation;

$$\hat{a}(\vec{p}, \infty) = \hat{a}(\vec{p}, -\infty) + i \int d^4x \bar{u}^{(s)}(\vec{p}) e^{ip \cdot x} \left(-i \overrightarrow{\not{\partial}} + m \right) \psi(x). \quad (1.51)$$

By substituting these results into our expression for $\langle f|i \rangle$ we get;

$$\begin{aligned}
\langle f|i \rangle = & \langle 0| T \left[\left(\hat{a}^\dagger(\vec{k}_1, \infty) + i \int d^4 x_1 \bar{\psi}(x_1) \left(i \overleftarrow{\not{\partial}} + m \right) e^{-ik_1 \cdot x_1} u^{(r')}(\vec{k}_1) \right) \right. \\
& \times \left(\hat{a}^\dagger(\vec{k}_2, \infty) + i \int d^4 x_2 \bar{\psi}(x_2) \left(i \overleftarrow{\not{\partial}} + m \right) e^{-ik_2 \cdot x_2} u^{(s')}(\vec{k}_2) \right) \\
& \times \left(\hat{a}(\vec{p}_1, -\infty) + i \int d^4 y_1 \bar{u}^{(r)}(\vec{p}_1) e^{ip_1 \cdot y_1} \left(-i \overrightarrow{\not{\partial}} + m \right) \psi(y_1) \right) \\
& \left. \times \left(\hat{a}(\vec{p}_2, -\infty) + i \int d^4 y_2 \bar{u}^{(s)}(\vec{p}_2) e^{ip_2 \cdot y_2} \left(-i \overrightarrow{\not{\partial}} + m \right) \psi(y_2) \right) \right] |0 \rangle.
\end{aligned} \tag{1.52}$$

All terms containing operators will now act on the vacuum and so drop out of the expression, since we define $\hat{a}(\vec{p})|0\rangle = 0$. What is left is the *LSZ Formula* for this process;

$$\begin{aligned}
\langle f|i \rangle = & (i)^4 \int d^4 x_1 d^4 x_2 d^4 y_1 d^4 y_2 e^{i(p_1 \cdot y_1 + p_2 \cdot y_2 - k_1 \cdot x_1 - k_2 \cdot x_2)} \\
& [\bar{u}^{(r)}(p_1)(-i \overrightarrow{\not{\partial}} + m)]_\alpha [\bar{u}^{(s)}(p_2)(-i \overrightarrow{\not{\partial}} + m)]_\beta \\
& \langle 0| T (\bar{\psi}_\alpha(y_1) \bar{\psi}_\beta(y_2) \psi_{\alpha'}(x_1) \psi_{\beta'}(x_2)) |0 \rangle \\
& [(i \overleftarrow{\not{\partial}} + m)u^{(r')}(k_1)]_{\alpha'} [(i \overleftarrow{\not{\partial}} + m)u^{(s')}(k_2)]_{\beta'},
\end{aligned} \tag{1.53}$$

where we have written out explicit spinor indices to make clear which operators act on which fields. Therefore, if we know how to calculate the time ordered product of fields then we also know how to calculate the scattering amplitude $\langle f|i \rangle$. We will now see how we can use the path integral formulation to get this.

1.3.3 Correlation Functions from Path Integrals

Consider a path integral of a general field ϕ of the form;

$$P = \int_{\phi(-T, \vec{x}) = \phi_a(\vec{x})}^{\phi(T, \vec{x}) = \phi_b(\vec{x})} \mathcal{D}\phi(x) \phi(x_1) \phi(x_2) \exp \left(i \int_{-T}^T d^4 x \mathcal{L} \right). \tag{1.54}$$

We rewrite the integral in a convenient manner;

$$\int \mathcal{D}\phi(x) = \int \mathcal{D}\phi_1(\vec{x}) \int \mathcal{D}\phi_2(\vec{x}) \int \mathcal{D}\phi(x) \delta(\phi(x_1^0, \vec{x}) - \phi_1(\vec{x})) \delta(\phi(x_2^0, \vec{x}) - \phi_2(\vec{x})). \quad (1.55)$$

This decomposition means that the main integral $\mathcal{D}\phi(x)$ is constrained at the times x_1^0 and x_2^0 , but the intermediate configurations ϕ_1, ϕ_2 must be integrated over. This allows for us to write our integral as;

$$\begin{aligned} P &= \int \mathcal{D}\phi_1(\vec{x}) \phi_1(\vec{x}_1) \int \mathcal{D}\phi_2(\vec{x}) \phi_2(\vec{x}_2) \\ &\times \int \mathcal{D}\phi(x) \exp \left(i \int_{\max[x_1^0, x_2^0]}^T d^4x \mathcal{L} \right) \\ &\times \int \mathcal{D}\phi(x) \exp \left(i \int_{\min[x_1^0, x_2^0]}^{\max[x_1^0, x_2^0]} d^4x \mathcal{L} \right) \\ &\times \int \mathcal{D}\phi(x) \exp \left(i \int_{-T}^{\min[x_1^0, x_2^0]} d^4x \mathcal{L} \right) \end{aligned} \quad (1.56)$$

We will take $x_2^0 > x_1^0$ for now and later on automatically generate the other possibility via use of the time ordering operator. Each of the three integrals over $\phi(x)$ is simply a transition amplitude; $\langle q_b | U(t_1 - t_0) | q_a \rangle$. Therefore;

$$\begin{aligned} P &= \int \mathcal{D}\phi_1(\vec{x}) \phi_1(\vec{x}_1) \int \mathcal{D}\phi_2(\vec{x}) \phi_2(\vec{x}_2) \\ &\times \langle \phi_b(\vec{x}) | e^{-i\hat{H}(T-x_2^0)} | \phi_2(\vec{x}) \rangle \\ &\times \langle \phi_2(\vec{x}) | e^{-i\hat{H}(x_2^0-x_1^0)} | \phi_1(\vec{x}) \rangle \\ &\times \langle \phi_1(\vec{x}) | e^{-i\hat{H}(x_1^0+T)} | \phi_a(\vec{x}) \rangle . \end{aligned} \quad (1.57)$$

Now, the factors $\phi_i(\vec{x}_i)$ can be interpreted as the eigenvalue of the Schrödinger

operator $\hat{\phi}_S(\vec{x}_i)$ acting on the state $|\phi_i(\vec{x}_i)\rangle$. Thus;

$$\begin{aligned}
P &= \int \mathcal{D}\phi_1(\vec{x}) \int \mathcal{D}\phi_2(\vec{x}) \\
&\times \langle \phi_b(\vec{x}) | e^{-i\hat{H}(T-x_2^0)} \hat{\phi}_S(\vec{x}_2) | \phi_2(\vec{x}) \rangle \\
&\times \langle \phi_2(\vec{x}) | e^{-i\hat{H}(x_2^0-x_1^0)} \hat{\phi}_S(\vec{x}_1) | \phi_1(\vec{x}) \rangle \\
&\times \langle \phi_1(\vec{x}) | e^{-i\hat{H}(x_1^0+T)} | \phi_a(\vec{x}) \rangle .
\end{aligned} \tag{1.58}$$

We can now use the completeness relation on the ϕ_1, ϕ_2 states and are left with;

$$P = \langle \phi_b(\vec{x}) | e^{-i\hat{H}(T-x_2^0)} \hat{\phi}_S(\vec{x}_2) e^{-i\hat{H}(x_2^0-x_1^0)} \hat{\phi}_S(\vec{x}_1) e^{-i\hat{H}(x_1^0+T)} | \phi_a(\vec{x}) \rangle . \tag{1.59}$$

At this point, we recognise that we can relate the Heisenberg operator to the Schrödinger operators via $\hat{\phi}_H(x) = e^{i\hat{H}t} \hat{\phi}_S(\vec{x}) e^{-i\hat{H}t}$ and therefore;

$$P = \langle \phi_b(\vec{x}) | e^{-i\hat{H}T} T \left(\hat{\phi}_H(x_2) \hat{\phi}_H(x_1) \right) e^{-i\hat{H}T} | \phi_a(\vec{x}) \rangle , \tag{1.60}$$

where the time ordering operator has been inserted so that we are also including the possibility that $x_1^0 > x_2^0$. The last step is to take the limit where T becomes large. Doing this naively, however, will leave us with an ill-defined limit, so we take the limit $T \rightarrow \infty(1-i\delta)$ with δ small and positive. Then;

$$e^{-i\hat{H}T} | \phi_a \rangle = \sum_n e^{-i\hat{H}T} | n \rangle \langle n | \phi_a \rangle \rightarrow \sum_n e^{-iE_n(\infty(1-i\delta))} | n \rangle \langle n | \phi_a \rangle = | 0 \rangle \langle 0 | \phi_a \rangle , \tag{1.61}$$

where in the last step we have assumed that the vacuum state has zero energy and thus is the only one that survives out of the sum. Therefore;

$$\lim_{T \rightarrow \infty(1-i\delta)} P = \langle 0 | T \left(\hat{\phi}_H(x_2) \hat{\phi}_H(x_1) \right) | 0 \rangle \times \langle 0 | \phi_a \rangle \langle \phi_b | 0 \rangle . \tag{1.62}$$

Comparing this to 1.53, we see that we have reproduced it up to the factors of the overlap between the states ϕ_a, ϕ_b and the vacuum. We can simply divide these out by evaluating the path integral without the factors of the field. We therefore

have the result;

$$\langle 0|T\left(\hat{\phi}_H(x_2)\hat{\phi}_H(x_1)\right)|0\rangle = \lim_{T\rightarrow\infty(1-i\delta)} \frac{\int \mathcal{D}\phi(x) \phi(x_1)\phi(x_2) \exp\left(i\int_{-T}^T d^4x \mathcal{L}\right)}{\int \mathcal{D}\phi(x) \exp\left(i\int_{-T}^T d^4x \mathcal{L}\right)} \quad (1.63)$$

1.3.4 Calculating a Scattering Amplitude

We are almost at the point where we can calculate a scattering amplitude. We have the LSZ formula as a ‘master equation’ and we’ve shown how the time-ordered product of fields can be calculated by path integrals. What remains, then, is a method for calculating such integrals. To do this, we define a *generating functional*;

$$\mathcal{Z}_0 \equiv \int \mathcal{D}\phi e^{i\int d^4x (\mathcal{L}_0 + J\phi)}, \quad (1.64)$$

where \mathcal{L}_0 is a free Lagrangian, the Lagrangian for a field with no interactions (i.e. the field satisfies the free equation of motion at all times). J is a source term that will turn out to be very useful for our calculations. To demonstrate the procedure, we will take a simple explicit example of the Lagrangian for a real scalar field;

$$\mathcal{L}_{0,RS} = \frac{1}{2}\partial^\mu\phi\partial_\mu\phi - \frac{1}{2}m^2\phi^2. \quad (1.65)$$

We saw in the previous section that we had to analytically continue the time to get a well-defined limit. This effect can equally be achieved by making the substitution $m^2 \rightarrow m^2 - i\delta$ and so we will do that. Performing a Fourier transform

on the source and field, we can write our free action as;

$$\begin{aligned}
S_{0,RS}(J) &\equiv \int d^4x (\mathcal{L}_{0,RS} + J\phi) \\
&= \frac{1}{2} \int \frac{d^4k}{(2\pi)^4} \left(\tilde{\phi}(k)(k^2 - m^2 + i\delta)\tilde{\phi}(-k) + \tilde{J}(k)\tilde{\phi}(-k) + \tilde{J}(-k)\tilde{\phi}(k) \right).
\end{aligned} \tag{1.66}$$

We shift our variable to $\tilde{\eta}(k) = \tilde{\phi}(k) + \frac{1}{k^2 - m^2 + i\delta}\tilde{J}(k)$ in order to complete the square and therefore arrive at;

$$S_{0,RS} = \frac{1}{2} \int \frac{d^4k}{(2\pi)^4} \left(\tilde{\eta}(k)(k^2 - m^2 + i\delta)\tilde{\eta}(-k) - \frac{\tilde{J}(k)\tilde{J}(-k)}{k^2 - m^2 + i\delta} \right). \tag{1.67}$$

The only η dependence is in the first quadratic term. We recognise this as a Gaussian functional integral over η and so will correspond to the overall normalisation of \mathcal{Z}_0 which can be adjusted by properly defining the measure of the functional integral such that $\mathcal{Z}_0(J=0) = 1$. Even if we don't adjust like this, we saw from the previous section that we need a ratio of correlation functions and would cancel out anyway when computing objects that are of interest in scattering amplitudes. We choose to do the adjustment and so;

$$\mathcal{Z}_0 = \exp \left(-\frac{i}{2} \int \frac{d^4k}{(2\pi)^4} \frac{\tilde{J}(k)\tilde{J}(-k)}{k^2 - m^2 + i\delta} \right). \tag{1.68}$$

In configuration space, we can write this result as;

$$\mathcal{Z}_0 = \exp \left(-\frac{1}{2} \int d^4x \int d^4y J(x) D_F(x-y) J(y) \right). \tag{1.69}$$

with;

$$D_F(x-y) = \int \frac{d^4k}{(2\pi)^4} e^{-ik(x-y)} \frac{i}{k^2 - m^2 + i\delta}. \tag{1.70}$$

This object is called the *Feynman propagator* and will appear often in calculations. The last ingredient is to devise a technique for calculating a general correlation function from the generating functional. This is achieved with

functional derivatives, defined such that;

$$\frac{\delta}{\delta J(x)} J(y) = \delta^4(x - y), \quad \frac{\delta}{\delta J(x)} \int d^4y J(y) \phi(y) = \phi(x). \quad (1.71)$$

Computing a two-point function in the free theory, then;

$$\begin{aligned} \int \mathcal{D}\phi \phi(x_1) \phi(x_2) e^{i \int d^4x \mathcal{L}_0} &= \frac{1}{i} \frac{\delta}{\delta J(x_1)} \frac{1}{i} \frac{\delta}{\delta J(x_2)} \int \mathcal{D}\phi e^{i \int d^4x (\mathcal{L}_0 + J\phi)} \Big|_{J=0} \\ &= \frac{1}{i} \frac{\delta}{\delta J(x_1)} \frac{1}{i} \frac{\delta}{\delta J(x_2)} \mathcal{Z}_0(J) \Big|_{J=0}. \end{aligned} \quad (1.72)$$

Such a procedure can be extended to an arbitrary number of fields in our correlation function. After taking the derivatives, this expression yields $D_F(x_1 - x_2)$ and so we see why the nomenclature ‘propagator’ is used; the two-point correlation function in the free theory is described as the propagation of a particle between the two points.

1.4 Feynman Rules (in QCD)

Though there are more considerations we should make in order to be completely accurate, we will instead leave the general QFT discussion here and move onto the main method for how particle physics calculations are performed; the evaluation of correlation functions in an interaction Lagrangian. For the reader interested in the fuller story, we defer to [42] or [46].

We can always split a general Lagrangian into a ‘free’ part, which we have seen can be solved exactly, and an interacting part; $\mathcal{L} = \mathcal{L}_0 + \mathcal{L}_I$. Sticking with our

real scalar field, our generating functional would have the form;

$$\begin{aligned}\mathcal{Z}(J) &= \int \mathcal{D}\phi e^{i \int d^4x (\mathcal{L} + J\phi)} \\ &= \int \mathcal{D}\phi e^{i \int d^4x \mathcal{L}_1} e^{i \int d^4x (\mathcal{L}_0 + J\phi)}.\end{aligned}\tag{1.73}$$

As an example, we take our interaction Lagrangian to have the form $g\phi^3$. In the generating functional, we can replace instances of ϕ with functional derivatives;

$$\mathcal{Z}_1 \propto \exp \left(ig \int d^4y \left(\frac{1}{i} \frac{\delta}{\delta J(y)} \right)^3 \right) \mathcal{Z}_0.\tag{1.74}$$

This equation cannot be solved exactly, but if g is small enough we can expand the exponential and order-by-order perform the functional derivatives, stopping at some point. In this way, we are considering that the interaction term is a perturbation to the free Lagrangian and hence the method is called *perturbation theory*. It should be clear to see that as the calculation proceeds to higher and higher orders in perturbation theory, the number of terms to deal with gets uncontrollably large. Thankfully, for many processes it is generally true that the first few orders tend to be enough to give us a good description and so higher order terms are not ‘needed’. However, there are some instances where perturbation theory breaks down and that provides the main motivation for the work in this thesis. Overlooking that for now, we would appear to have a formula which we can generally apply. This is the case, but having to keep track of all the terms that come from our functional derivatives and distinguishing which of these terms are the same as others is a very time-consuming and error-prone task. Luckily, *Feynman rules* and *Feynman graphs* provide us with an excellent, intuitive tool to deal with perturbation theory.

The Feynman rules are a set of instructions for drawing a Feynman diagram, which itself represents a mathematical equation that can be written down and evaluated yielding part or possibly all of the transition amplitude $\langle f|i \rangle$ at a given order in perturbation theory. The Feynman rules themselves will depend on the Lagrangian of any given theory we are interested in calculating in. To demonstrate the procedure for generating Feynman rules and diagrams, let us

consider a simple Lagrangian of the form;

$$\mathcal{L}_{example} = \frac{1}{2}\partial_\mu\phi\partial^\mu\phi - \frac{1}{2}m^2\phi + \frac{g}{3!}\phi^3. \quad (1.75)$$

The process then proceeds schematically as follows;

1. Identify the entire field content of the Lagrangian. In this case, we have only one field ϕ . For each field, identify the propagator terms, which are terms that contain exactly two of the field. For our Lagrangian, these are the first two terms. If such a collection of terms exists, we can represent the propagation of a field from one point to another diagrammatically by some line. For our example, we will simply represent the propagation of ϕ from one point to another by a solid black line.
2. All other terms represent interactions, with the number of fields in each term corresponding to the number of fields present in the interaction. Here, we have only one interaction term with three instances of the field ϕ , which means our only allowed interaction is between three particles of the field ϕ .
3. Consider the type of process to be described. For instance, we could be interested in working out the transition amplitude for two particles of the field ϕ to scatter off each other into again two particles of the field ϕ (more compactly, a $2 \rightarrow 2$ process).
4. Assuming for the time being we are interested in the lowest order of perturbation theory, draw all possible diagrams with the lowest number of interaction points for the process (also sometimes known as *tree level*), subject to the propagation and interaction rules discussed. We will use the convention where time is flowing from left to right through the diagram. It is almost always more useful to work in momentum space, so also label the particles with some momentum values.

For our example theory, the set of diagrams at leading order as specified by following these rules are as shown in figure 1.2.

The topology of these diagrams is commonly seen in ones produced from real-world theories as well and they have the special names *s*-channel, *t*-channel and *u*-channel. These names come from the *Mandelstam variables* which refer to

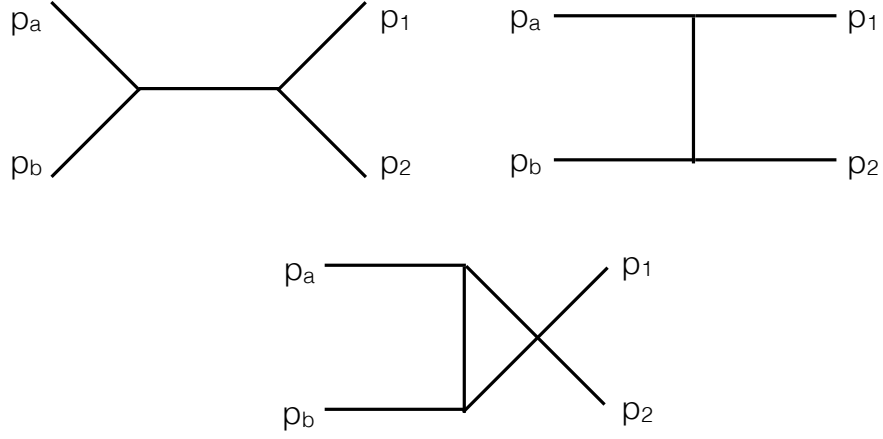


Figure 1.2 *Example Feynman diagrams. The top-left diagram is called the s-channel, the top right the t-channel and the bottom the u-channel. All momenta flow from left to right.*

the invariant mass present in the intermediate propagator in each diagram, fixed by momentum conservation at each vertex; $s = (p_a + p_b)^2$, $t = (p_a - p_1)^2$ and $u = (p_a - p_2)^2$.

Now that we have seen the general procedure for drawing diagrams, we need mathematical rules to convert these diagrams into calculable expressions. These are the famous *Feynman rules* and while there is a general way of deriving them for any given theory we will jump straight to the rules we need for the theory of QCD that the rest of the thesis depends upon;

1. *External Fermion Lines.* For an external quark, associate a factor $u(p)$ for incoming and $\bar{u}(p)$ for outgoing. For external anti-quarks, associate a factor $\bar{v}(p)$ for incoming and $v(p)$ for outgoing. To ensure consistent multiplication in the spinor indices, follow a quark line backwards through the diagram.
2. *External Gluon Lines.* Associate a factor $\varepsilon_\mu(p)$ for incoming and $\varepsilon_\mu^*(p)$ for outgoing. These objects are the so-called *polarisation vectors* of the gluons and arise from solving the equation of motion for them.
3. *Internal propagators.* For each internal propagator, associate the relevant factor as detailed in table 1.1
4. *Vertices.* For each vertex, associate the relevant factor as detailed in table 1.1

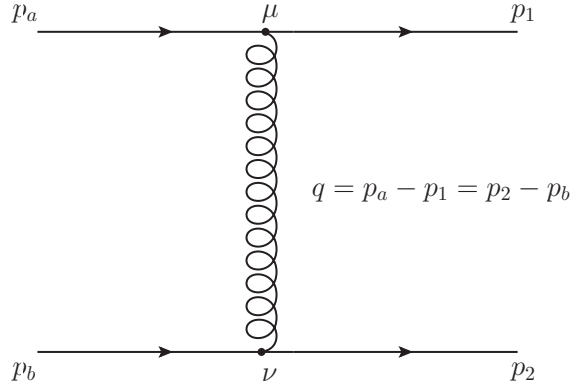


Figure 1.3 Two quarks of different flavour scattering via the exchange of a gluon in the t -channel.

5. *Unconstrained momenta.* Beyond first order in perturbation theory, Feynman graphs will contain momenta that are not fixed by momentum conservation, resulting in what are called *loops*. For each such momenta k , include an integration $\int \frac{d^4 k}{(2\pi)^4}$.
6. *Extra signs.* Each fermion or anti-fermion loop comes with a factor of (-1) and each anti-fermion line that flows from the initial state to the final state also comes with a factor of (-1) . These rules result from the fact the fermion operators anti-commute and an explicit demonstration of precisely why we need these extra considerations will not be shown.

Following these rules and adding together all diagrams results in the quantity iM , where M is the *matrix element* or *amplitude* $\langle f|i \rangle$ at the calculated order in the coupling expansion. Later on, we will see exactly how this relates to a physical quantity.

1.4.1 $qQ \rightarrow qQ$ at Leading Order

As an explicit exercise in performing QCD calculations with Feynman rules, let us take an example of an up quark scattering off a down quark into again an up quark and a down quark. This process is particularly simple because there is only one contributing Feynman diagram, shown in figure 1.3.



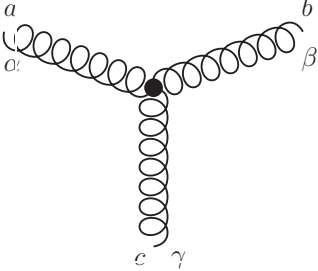
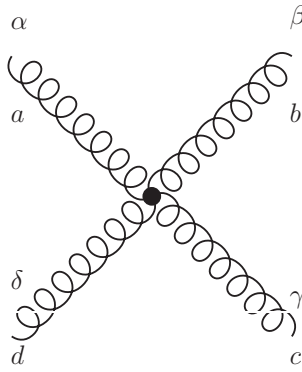
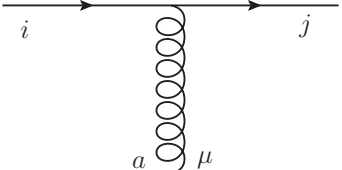
Diagrammatic Element	Description	Feynman Rule
	Quark Propagator with fundamental colour index $i \rightarrow j$, momentum p and mass m_f	$\frac{i\delta_{ij}}{\not{p} - m_f} = \frac{i\delta_{ij}(\not{p} + m_f)}{p^2 - m_f^2}$
	Gluon Propagator with adjoint colour index $a \rightarrow b$ and momentum p	$\frac{-i\delta^{ab}\eta^{\mu\nu}}{p^2}$
	Three-Gluon Vertex. All momenta taken as incoming, with k_1 associated with the gluon with adjoint index a , k_2 with b and k_3 with c	$-g_s f^{abc}(\eta^{\alpha\beta}(k_1 - k_2)^\gamma + \eta^{\beta\gamma}(k_2 - k_3)^\alpha + \eta^{\gamma\alpha}(k_3 - k_1)^\beta)$
	Four-Gluon Vertex with adjoint indices a, b, c, d	$-ig_s^2(f^{ade}f^{cde}(\eta^{\alpha\gamma}\eta^{\beta\delta} - \eta^{\alpha\delta}\eta^{\beta\gamma}) + f^{ace}f^{bde}(\eta^{\alpha\beta}\eta^{\gamma\delta} - \eta^{\alpha\delta}\eta^{\gamma\beta}) + f^{ade}f^{bce}(\eta^{\alpha\beta}\eta^{\delta\gamma} - \eta^{\alpha\gamma}\eta^{\delta\beta}))$
	Quark-Gluon Vertex with fundamental indices i, j and adjoint index a	$-ig_s \gamma^\mu t_{ij}^a$

Table 1.1 *QCD Feynman Rules for propagators and vertices*

Applying the Feynman rules, we arrive at the expression for the amplitude;

$$\begin{aligned}
iM &= \bar{u}(p_2)(-ig_s t^b \gamma^\nu)u(p_b) \left(\frac{-i\eta_{\mu\nu}\delta^{ab}}{(p_a - p_1)^2} \right) \bar{u}(p_1)(-ig_s t^a \gamma^\mu)u(p_a) \\
&= \left(\frac{t^b \delta^{ab} t^a i g_s^2}{(p_a - p_1)^2} \right) \bar{u}(p_2) \gamma_\mu u(p_b) \bar{u}(p_1) \gamma^\mu u(p_a) \\
&= \left(\frac{t^a \delta^{ab} t^b i g_s^2}{\hat{t}} \right) \bar{u}(p_2) \gamma_\mu u(p_b) \bar{u}(p_1) \gamma^\mu u(p_a),
\end{aligned} \tag{1.76}$$

where we have for now suppressed the colour and spin dependence of the quark spinors. In general, there is no control over the colours and spins of the particles in our experiment and so we should take this into account. We will need to average over all initial state spins/colours and sum over all final state spins/colours. From the general laws of Quantum Mechanics [25], we ultimately know that any physical quantity must be proportional to $|M|^2$. Since each helicity and colour configuration are physically distinguishable (that is, they do not interfere with each other quantum mechanically, we are just ignorant of what the states are), this sum/average must be done at the $|M|^2$ level;

$$|\bar{M}|^2 = \frac{1}{9} \times \frac{1}{4} \times \frac{g_s^4}{\hat{t}^2} \times \sum_{\text{colours}} \sum_{\text{spins}} |\tilde{M}|^2, \quad (1.77)$$

where we have stripped some factors that don't depend on the spins/colours out of the matrix elements. We will begin by performing the spin sum. It will be useful to keep track of spinor indices in this calculation, which are implicitly summed over, and introduce the notation $u(p) \equiv u_p$ to get;

$$\begin{aligned} \sum_{\text{spins}} |\tilde{M}|^2 &= \sum_{\text{spins}} [\bar{u}_2^{i_1} \gamma_\mu^{i_1 j_1} u_b^{j_1}] [\bar{u}_1^{i_2} \gamma^{\mu, i_2 j_2} u_a^{j_2}] [\bar{u}_2^{i_3} \gamma_\nu^{i_3 j_3} u_b^{j_3}]^\dagger [\bar{u}_1^{i_4} \gamma^{\nu, i_4 j_4} u_a^{j_4}]^\dagger \\ &= \sum_{\text{spins}} [\bar{u}_2^{i_1} \gamma_\mu^{i_1 j_1} u_b^{j_1}] [\bar{u}_1^{i_2} \gamma^{\mu, i_2 j_2} u_a^{j_2}] [\bar{u}_b^{i_3} \gamma_\nu^{i_3 j_3} u_2^{j_3}] [\bar{u}_a^{i_4} \gamma^{\nu, i_4 j_4} u_1^{j_4}], \end{aligned} \quad (1.78)$$

where we have used $(\gamma^0)^\dagger = \gamma^0$ and $(\gamma^\mu)^\dagger = \gamma^0 \gamma^\mu \gamma^0$. At this point we introduce the important result;

$$\sum_{\text{spins}} u_p \bar{u}_p = \not{p} + m, \quad (1.79)$$

which amounts to the statement that the set of u functions are complete. To reduce the amount of terms we will have to deal with, we will take the mass of the quarks in our calculation to be zero. This is a good approximation if the momentum of the particles involved in the scattering is much larger than the value of the mass and we will always assume this is the case unless otherwise stated in the entirety of this thesis. Using this result to rewrite our amplitude

and being careful with spinor indices, we see;

$$\begin{aligned}
\sum_{spins} |\tilde{M}|^2 &= [\not{p}_b^{j_1 i_3} \gamma_{\nu}^{i_3 j_3} \not{p}_2^{j_3 i_1} \gamma_{\mu}^{i_1 j_1}] [\not{p}_a^{j_2 i_4} \gamma^{\nu, i_4 j_4} \not{p}_1^{j_4 i_2} \gamma^{\mu, i_2 j_2}] \\
&= Tr[\gamma_{\alpha} \gamma_{\nu} \gamma_{\beta} \gamma_{\mu}] p_b^{\alpha} p_2^{\beta} \times Tr[\gamma^{\rho} \gamma^{\nu} \gamma^{\sigma} \gamma^{\mu}] p_{a,\rho} p_{1,\sigma}.
\end{aligned} \tag{1.80}$$

What remains is to evaluate the traces of the products of gamma matrices. There are a whole host of so-called *trace theorems* [42], of which we quote one result;³

$$Tr[\gamma^{\alpha} \gamma^{\nu} \gamma^{\beta} \gamma^{\mu}] = 4(\eta^{\alpha\nu} \eta^{\beta\mu} - \eta^{\alpha\beta} \eta^{\nu\mu} + \eta^{\alpha\mu} \eta^{\nu\beta}). \tag{1.81}$$

Applying this result to our calculation, we arrive at;

$$\begin{aligned}
\sum_{spins} |\tilde{M}|^2 &= 16(p_{b,\nu} p_{2,\mu} - p_b \cdot p_2 \eta_{\nu\mu} + p_{b,\mu} p_{2,\nu}) \times (p_a^{\nu} p_1^{\mu} - p_a \cdot p_1 \eta^{\nu\mu} + p_a^{\mu} p_1^{\nu}) \\
&= 32((p_b \cdot p_a)(p_1 \cdot p_2) + (p_b \cdot p_1)(p_2 \cdot p_a)),
\end{aligned} \tag{1.82}$$

which is a simple result. The final ingredient of the amplitude is the colour sum. Since this is the first time we are performing such a calculation. It is instructive

³This result only applies in a 4-dimensional spacetime, which we have in this problem, but can be generalised to general dimensions if required.

to do this in detail. We write out the colour indices in full [44];

$$\begin{aligned}
\sum_{\text{colours}} |\tilde{M}|^2 &\sim \sum_{\text{colours}} [t_{q_1, q_a}^a \delta^{ab} t_{q_2, q_b}^b] [t_{q_1, q_a}^c \delta^{cd} t_{q_2, q_b}^d]^\dagger \\
&= \sum_{a, b, c, d, q_1, q_a, q_2, q_b} [t_{q_1, q_a}^a \delta^{ab} t_{q_2, q_b}^b] [t_{q_a, q_1}^c \delta^{cd} t_{q_b, q_2}^d] \\
&= \sum_{a, c, q_1, q_a, q_2, q_b} [t_{q_1, q_a}^a t_{q_2, q_b}^a] [t_{q_a, q_1}^c t_{q_b, q_2}^c] \\
&= \sum_{a, c} \text{Tr}(t^a t^c) \text{Tr}(t^a t^c) \\
&= \sum_{a, c} \frac{1}{2} \delta^{ac} \frac{1}{2} \delta^{ac} \\
&= \sum_a \frac{1}{4} \delta^{aa} \\
&= 2.
\end{aligned} \tag{1.83}$$

Combining the results, we find an expression for the full amplitude;

$$\begin{aligned}
|M|^2 &= \frac{16g_s^4}{9\hat{t}^2} ((p_b \cdot p_a)(p_1 \cdot p_2) + (p_b \cdot p_1)(p_2 \cdot p_a)) \\
&= g_s^4 \times \frac{4}{9} \left(\frac{\hat{s}^2 + \hat{u}^2}{\hat{t}^2} \right).
\end{aligned} \tag{1.84}$$

As a matter of interest, this result is the same as the one we would get from electron-muon scattering, except with a different coupling strength and an overall colour factor. We should expect this because our process did not involve any parts where the gluon interacts with itself and so behaves similarly to a photon in this interaction. If we were to do a next-to-leading order calculation, however, this would no longer be true and QCD loop calculations are, in general, difficult to compute.

1.5 Cross Sections in Proton-Proton Collisions

In a collider experiment, the physical quantity is the *cross section*, not the squared matrix element itself. The two are intimately related, however, by *Fermi's Golden*

Rule, which in this case states;

$$d\hat{\sigma} = S \times \frac{|M|^2}{F} \times (2\pi)^4 \delta^{(4)}(p_a + p_b - \sum_{f=1}^n p_f) \times \prod_{i=1}^n \frac{d^3 \vec{p}_i}{2E_i (2\pi)^3}. \quad (1.85)$$

$|M|^2$ is the matrix element squared for the considered process and contains all the dynamical information. $F = 4\sqrt{(p_a \cdot p_b)^2 - m_a m_b}$ is the factor that accounts for the flux of incoming particles. The delta function ensures momentum conservation in the process. The remaining integrals are *phase space* integrals over the final particles and finally S is a statistical factor which serves to avoid over-counting in processes with indistinguishable outgoing particles - for each group of s identical particles in the final state, S gains a factor $1/s!$. In theory, then, we can plug in any matrix element calculated at a certain order in our perturbation theory and perform the phase space integrals to yield the cross section for any process we desire. In practice, this is not as simple as it sounds. For instance, as the number of final state particles is increased, an analytic integration over their momenta becomes more and more difficult (the matrix elements as well become more difficult to compute - a point we will pick up on again later). Furthermore, in QCD we can't collide two quarks together with a well-defined energy as our matrix element calculation might suggest because of a property called *confinement* - because of how the strong force interacts, it is impossible to observe a free quark or gluon⁴. Instead, we have to collide hadrons together (for the LHC, specifically protons) which are a dynamic soup of quarks, anti-quarks and gluons (from here on, *partons*). However, if the energy of the collider is large enough (which it certainly is in the LHC) then we can model a proton - proton collision as a collision of two partons within each of the protons, each of which carrying some fraction of the total proton momentum. This treatment is essentially a probabilistic one and has led to the development of *Parton Distribution Functions* (PDFs) [45] which in itself is an area of intense research. For our purposes though, we need not discuss in detail the field of PDFs and instead just use the property that we can write our total proton-proton cross section as some convolution;

$$d\sigma_{pp} = \sum_{f_a, f_b} \int_0^1 dx_a \int_0^1 dx_b f_a(x_a) f_b(x_b) \times d\hat{\sigma}_{partonic}, \quad (1.86)$$

⁴Though confinement has been phenomenologically established, it is not understood from a purely theoretical viewpoint. This is essentially because it would involve calculating without the use of perturbation theory, which is a very tough ask. It is therefore an outstanding problem set by the Clay Mathematics Institute to prove confinement.

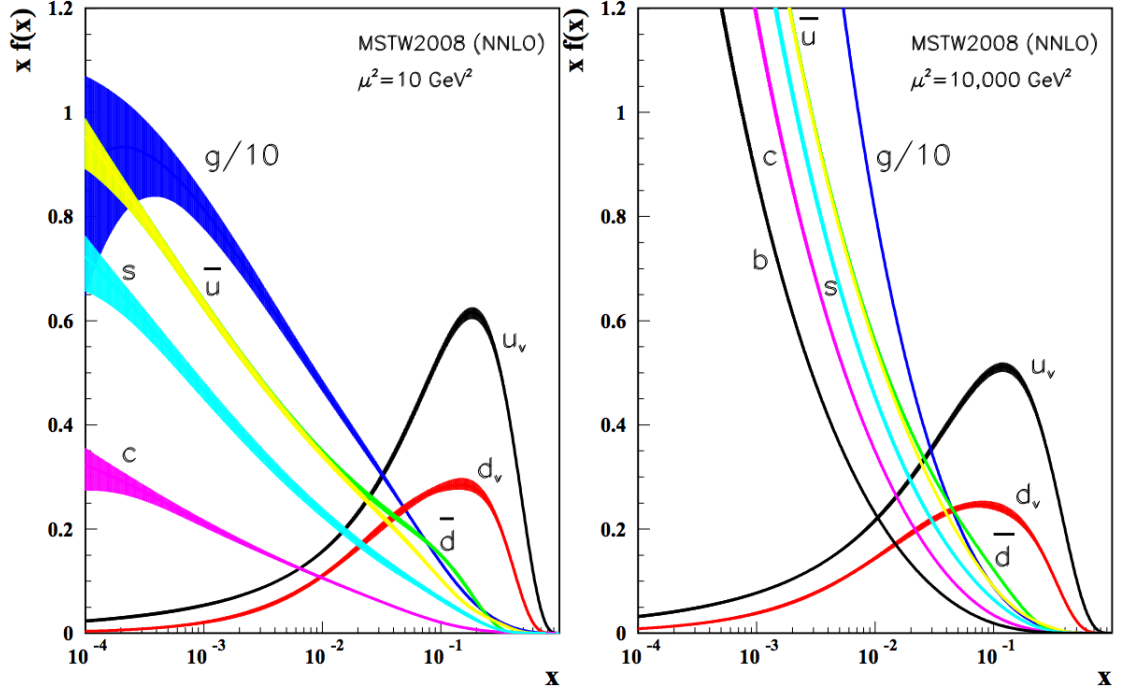


Figure 1.4 *An example of a PDF set and how the value of the PDF changes depending on the scale probed. Figure from a review by the PDG [41]*

where we interpret x_a, x_b as the fraction of the total momentum carried by the parton from each of the protons and $f_a(x_a), f_b(x_b)$ as the value of the PDF for a parton of flavour a, b carrying a momentum fraction x_a, x_b . This current formula doesn't explain all the necessary considerations, however. For example, we should expect that the form of the distributions functions has some dependence of the energy scale of the scattering, which we will call Q^2 . The reason for this is that, as Q^2 is increased, one is able to probe the interior of the proton more and more and thus the likelihood of picking out a certain parton of a certain momentum will depend on that. An example is shown in figure 1.4 where the behaviour of the PDF with respect to x is clearly different depending on the scale. A better equation would then be;

$$d\sigma_{pp} = \sum_{f_a, f_b} \int_0^1 dx_a \int_0^1 dx_b f_a(x_a, Q^2) f_b(x_b, Q^2) \times d\hat{\sigma}_{partonic}, \quad (1.87)$$

for some value of Q^2 . As to what that value should be, however, is somewhat mysterious - given a hard scattering, what is the relevant scale at which the PDF

is probed at? The ambiguity of this leads to the calculation of *scale variations*, which we will return to in a later chapter. Before that, we must also consider how confinement affects the final state of our scattering. The partonic cross section would lead us to believe that there are free partons after the scattering that we could detect, which goes against the principle of confinement. Indeed, we observe that the final state of partonic scatterings consists of objects called *jets*, which are ‘cones’ of hadrons and other particles caused by the *hadronization* of the partons produced in a scattering. A further discussion of the difference between partons and jets will also be discussed in a later chapter, but let us for now consider some ‘n-jet function’ which ‘passes’ an event (i.e. has value equal to 1) if there are n jets present in the final state and ‘fails’ (has value 0) otherwise. Such a function will be a so-called *exclusive* function, because only events with exactly n jets will contribute, but we could also imagine an *inclusive* function that will ‘pass’ events with at least n jets. We could therefore write;

$$d\sigma_{pp \rightarrow n\text{-jet}}^{inc/exc} = \sum_{f_a, f_b} \int_0^1 dx_a \int_0^1 dx_b f_a(x_a, Q^2) f_b(x_b, Q^2) \times d\hat{\sigma}_{partonic} \times \mathcal{J}(n\text{-jet}^{inc/exc}). \quad (1.88)$$

Generally speaking, it is not known how many jets n will be produced by a scattering leaving m partons in the final state and this (along with the more fundamental question of how to even properly *define* a jet) is again an area of significant research. The up-shot is that, for many reasons, the calculation of QCD cross sections is difficult and not without ambiguity. We will later see how, despite this, we can still get physically relevant results from the theory.

1.6 Spinor Helicity

We conclude the chapter by discussing the *spinor helicity formalism* for the calculation of amplitudes. The formalism makes the expression of amplitudes involving massless particles⁵ less cumbersome and we will make repeated use of it throughout the remainder of this thesis. *Helicity* is the projection of a particle’s spin along its momentum vector and can have two values; ‘negative’ when the spin is anti-aligned and ‘positive’ when it is aligned. We would clearly like to describe

⁵It can also be extended to include massive particles, but it is not its primary use and we will always be working with massless entities (either effectively or exactly) in this work.

this projection using some operator. This can be achieved by introducing a new gamma matrix $\gamma^5 = i\gamma^0\gamma^1\gamma^2\gamma^3$, which can be used to project out helicity states as follows;

$$u_{\pm}(p_i) = (1 \pm \gamma^5)u(p_i) \equiv |i^{\pm}\rangle \quad (1.89a)$$

$$v_{\mp}(p_i) = (1 \pm \gamma^5)v(p_i) \equiv |i^{\pm}\rangle \quad (1.89b)$$

$$\bar{u}_{\pm}(p_i) = \bar{u}(p_i)(1 \mp \gamma^5) \equiv \langle i^{\pm}| \quad (1.89c)$$

$$\bar{v}_{\mp}(p_i) = \bar{v}(p_i)(1 \mp \gamma^5) \equiv \langle i^{\pm}|. \quad (1.89d)$$

We also define the basic spinor products as;

$$\bar{u}_{-}(p_i)u_{+}(p_j) = \bar{v}_{+}(p_i)v_{-}(p_j) = \langle i^{-}|j^{+}\rangle \equiv \langle ij\rangle \quad (1.90a)$$

$$\bar{u}_{+}(p_i)u_{-}(p_j) = \bar{v}_{-}(p_i)v_{+}(p_j) = \langle i^{+}|j^{-}\rangle \equiv [ij]. \quad (1.90b)$$

The final object we will need to deal with is a *current* which has the form $\bar{u}\gamma^{\mu}u$. Because γ^5 anti-commutes with the other gamma matrices, only currents where the two spinors have the same helicity are non-zero;

$$\bar{u}_{\pm}(p_i)\gamma^{\mu}u_{\pm}(p_j) = \langle i^{\pm}|\mu|j^{\pm}\rangle \equiv J_{ij}^{\pm,\mu} \quad (1.91)$$

There are many identities that these objects satisfy [26] and we list here a select

few that we will use repeatedly in our calculations;

$$\langle ij \rangle = -\langle ji \rangle \quad (1.92a)$$

$$[ij] = -[ji] \quad (1.92b)$$

$$\langle ij \rangle^* = [ji] \quad (1.92c)$$

$$\langle i^+ | \mu | j^+ \rangle^\dagger = \langle j^+ | \mu | i^+ \rangle \quad (1.92d)$$

$$\langle i^\pm | \mu | i^\pm \rangle = 2p_i^\mu \quad (1.92e)$$

$$\langle i^+ | \mu | j^+ \rangle = \langle j^- | \mu | i^- \rangle \quad (1.92f)$$

$$\langle i^+ | \mu | j^+ \rangle \langle k^+ | \mu | l^+ \rangle = 2 \langle jl \rangle [ki] \quad (1.92g)$$

$$\langle ij \rangle [ji] = 2p_i \cdot p_j = s_{ij} \quad (1.92h)$$

$$\not{p}_i = |i^+\rangle \langle i^+| + |i^-\rangle \langle i^-| \quad (1.92i)$$

$$\langle ij \rangle \langle kl \rangle = \langle ik \rangle \langle jl \rangle + \langle il \rangle \langle kj \rangle. \quad (1.92j)$$

Given their importance to this thesis, we devote some space here to the derivation of some of these results. The easiest way to do so is to pick an explicit representation for the spinors and gamma matrices and work in individual components. It is instructive to work in *light cone coordinates* where we make the substitution $p^\pm = E \pm p_z$ and parameterise momenta transverse to the beam axis as $p_\perp = p_x + ip_y$. For outgoing particles with four-momentum p , we use;

$$u^+(p) = \begin{pmatrix} \sqrt{p^+} \\ \sqrt{p^-} \frac{p_\perp}{|p_\perp|} \\ 0 \\ 0 \end{pmatrix} \quad (1.93a)$$

$$u^-(p) = \begin{pmatrix} 0 \\ 0 \\ \sqrt{p^-} \frac{p_\perp^*}{|p_\perp|} \\ -\sqrt{p^+} \end{pmatrix} \quad (1.93b)$$

For incoming particles with 4-momentum p moving along the positive light cone

direction, we use:

$$u^+(p) = \begin{pmatrix} \sqrt{p^+} \\ 0 \\ 0 \\ 0 \end{pmatrix} \quad (1.94a)$$

$$u^-(p) = \begin{pmatrix} 0 \\ 0 \\ 0 \\ -\sqrt{p^+} \end{pmatrix} \quad (1.94b)$$

For incoming particles with 4-momentum p moving in the negative light cone direction, we use:

$$u^+(p) = \begin{pmatrix} 0 \\ -\sqrt{p^-} \\ 0 \\ 0 \end{pmatrix} \quad (1.95a)$$

$$u^-(p) = \begin{pmatrix} 0 \\ 0 \\ -\sqrt{p^-} \\ 0 \end{pmatrix} \quad (1.95b)$$

We also use the following representation of the gamma matrices;

$$\gamma^0 = \begin{pmatrix} 0 & 0 & 1 & 0 \\ 0 & 0 & 0 & 1 \\ 1 & 0 & 0 & 0 \\ 0 & 1 & 0 & 0 \end{pmatrix} \quad (1.96a)$$

$$\gamma^1 = \begin{pmatrix} 0 & 0 & 0 & -1 \\ 0 & 0 & -1 & 0 \\ 0 & 1 & 0 & 0 \\ 1 & 0 & 0 & 0 \end{pmatrix} \quad (1.96b)$$

$$\gamma^2 = \begin{pmatrix} 0 & 0 & 0 & i \\ 0 & 0 & -i & 0 \\ 0 & -i & 0 & 0 \\ i & 0 & 0 & 0 \end{pmatrix} \quad (1.96c)$$

$$\gamma^3 = \begin{pmatrix} 0 & 0 & -1 & 0 \\ 0 & 0 & 0 & 1 \\ 1 & 0 & 0 & 0 \\ 0 & -1 & 0 & 0 \end{pmatrix} \quad (1.96d)$$

With our conventions defined, we can move on to some derivations. An identity that is used often is $\langle i^\pm | \mu | i^\pm \rangle = 2p_i^\mu$ so this would be a sensible one to prove. If we have an incoming particle with momentum p , then the first element of the product is (we'll take positive helicity particles);

$$\langle i^+ | 0 | i^+ \rangle = (u_i^+)^\dagger \gamma^0 \gamma^0 u_i^+ = (u_i^+)^\dagger u_i^+ = p_i^+. \quad (1.97)$$

By inspection, we see that such a product will only be non-zero if the multiplication $\gamma^0 \gamma^\mu$ applied to u_i^+ is such that there is a non-zero component in the first component of the resulting spinor. In other words, the product $\gamma^0 \gamma^\mu$ must have a non-zero entry in the top-left. Explicit calculation of $\gamma^0 \gamma^1$ and $\gamma^0 \gamma^2$ show this not to be the case, and so;

$$\langle i^+ | 1 | i^+ \rangle = \langle i^+ | 2 | i^+ \rangle = 0. \quad (1.98)$$

Finally, the product $\gamma^0 \gamma^3$ does have a non-zero entry in the top-left which is equal

to 1 and thus;

$$\langle i^+ | 3 | i^+ \rangle = \langle i^+ | 0 | i^+ \rangle = p_i^+. \quad (1.99)$$

Converting p_i^+ to $E + p_z$ and remembering that the particle is massless and has no transverse component if it is incoming (i.e. $E = |p_z|$), then indeed we see that $\langle i^\pm | \mu | i^\pm \rangle = 2p_i^\mu$. The calculation for outgoing particles is longer because of the presence of the transverse term, but again this relationship is seen to hold. The other identity we will make particularly regular use of is $\langle ij \rangle [ji] = s_{ij}$. To prove this, let us take p_i to be incoming and along the positive direction and p_j to be incoming and along the negative direction. Direct calculation then yields;

$$\begin{aligned} \langle ij \rangle &= \bar{u}_i^- u_j^+ = \sqrt{p_i^+ p_j^-} \\ [ji] &= \bar{u}_j^+ u_i^- = \sqrt{p_i^+ p_j^-}, \end{aligned} \quad (1.100)$$

and thus $\langle ij \rangle [ji] = p_i^+ p_j^- = (E_i + E_i)(E_j + E_j) = 4E_i E_j = s_{ij}$. Again, the calculation involving outgoing particles is longer but the result is still seen to hold.

As an actual practical demonstration of the technique, let us repeat the calculation in the previous section in this new language. We will once again sum over all spins (equivalent to summing over all helicities), but for clarity let's work first with the case that all particles have positive helicity. Then;

$$\begin{aligned} iM_{++++} &= \langle 2^+ | (-ig_s t^b \gamma^\nu) | b^+ \rangle \left(\frac{-i\eta_{\mu\nu} \delta^{ab}}{(p_a - p_1)^2} \right) \langle 1^+ | (-ig_s t^a \gamma^\mu) | a^+ \rangle \\ &= \left(\frac{t^b \delta^{ab} t^a i g_s^2}{\hat{t}} \right) \langle 2^+ | \mu | b^+ \rangle \langle 1^+ | \mu | a^+ \rangle \\ &= \left(\frac{t^b \delta^{ab} t^a i g_s^2}{\hat{t}} \right) 2 \langle ba \rangle [12]. \end{aligned} \quad (1.101)$$

Since there are two helicity states for each particle, we would expect there to be $2^4 = 16$ different helicity configurations we would have to calculate. However, since the currents J_{2b} and J_{1a} disappear if the quark helicity is not

conserved, we only have 4 non-zero configurations. Furthermore, our relation $\langle i^+ | \mu | j^+ \rangle = \langle j^- | \mu | i^- \rangle$ reduces this to only two independent configurations. For example, the configuration where all particles have negative helicity is the same as the one with all positive helicity, except that we need to take the Hermitian conjugate of the currents. Once we take the absolute value squared of this quantity, this conjugation is irrelevant and so the amplitude contains no new information. Therefore, the only other matrix element we need to calculate is the one where the two quarks come in with opposite helicities;

$$\begin{aligned}
iM_{+-+-} &= \left(\frac{t^b \delta^{ab} t^a i g_s^2}{\hat{t}} \right) \langle 2^- | \mu | b^- \rangle \langle 1^+ | \mu | a^+ \rangle \\
&= \left(\frac{t^b \delta^{ab} t^a i g_s^2}{\hat{t}} \right) \langle b^+ | \mu | 2^+ \rangle \langle 1^+ | \mu | a^+ \rangle \\
&= \left(\frac{t^b \delta^{ab} t^a i g_s^2}{\hat{t}} \right) 2 \langle 2a \rangle [1b].
\end{aligned} \tag{1.102}$$

The colour sum and average must still be performed, of course, but other than that we can simply take the modulus squared, add and average over the helicities;

$$\begin{aligned}
|M|^2 &= \frac{1}{4} \times \frac{2}{9} \times (|M_{++++}|^2 + |M_{+--+}|^2 + |M_{-++-}|^2 + |M_{----}|^2) \\
&= \frac{1}{18} \times (2|M_{++++}|^2 + 2|M_{+--+}|^2) \\
&= g_s^4 \times \frac{4}{9} \left(\frac{\langle ba \rangle [12][ab] \langle 21 \rangle + \langle 2a \rangle [1b][a2] \langle b1 \rangle}{\hat{t}^2} \right) \\
&= g_s^4 \times \frac{4}{9} \left(\frac{s_{ab}s_{12} + s_{a2}s_{1b}}{\hat{t}^2} \right) \\
&= g_s^4 \times \frac{4}{9} \left(\frac{\hat{s}^2 + \hat{u}^2}{\hat{t}^2} \right),
\end{aligned} \tag{1.103}$$

where in the last line we used momentum conservation to equate s_{ab} with s_{12} and s_{a2} with s_{1b} and then substituted in the relevant Mandelstam variable. This is, of course, the same result as before except we did not have to go through the trouble of evaluating the traces of gamma matrices, which is a procedure that can be quite error-prone. Furthermore, we have gained some physical insight into why the terms \hat{s} and \hat{u} appear in the numerator; the former comes from the helicity configuration where the quarks have the same helicity and the latter from

the configuration where they are opposite. This simple example showed how easy the formalism is to work with and in the next chapter we will see how it is also powerful, in the sense that we will be able to express all-order matrix elements within it.

Chapter 2

High Energy Jets

We have shown how we can calculate physical quantities in a QFT by treating the interaction terms in a Lagrangian as a perturbation to the free Lagrangian. The expansion parameter is the strength of the coupling, usually denoted by g_s in QCD, and if this parameter is small enough¹, we can expect that the first few orders of perturbation theory should give us an accurate result. This implicitly assumes, however, that each term in the perturbative series is itself quite small. If these terms were too large, then we would run the risk of the perturbative series being non-convergent and so never be able to have a good description of the process. The natural question to ask is whether it is generally true that the terms in the perturbative series are small enough. We will see in this chapter that this is not always the case and how a technique known as *resummation* can take this into account.

2.1 The Problem with Perturbation Theory in the High Energy Limit

In order to proceed, we must define what is meant by the High Energy limit. For a $2 \rightarrow n$ process, we define it as the limit where the invariant mass between any two particles is large and all transverse momenta in the problem are fixed and

¹At the level of the physical cross section, because of the combination of phase space and Fermi's Golden Rule factors, it is often said that the relevant parameter is actually $\alpha_s = g_s^2/4\pi$, which is even smaller.

much smaller than this. Formally;

$$\forall_{i,j} : s_{ij} \rightarrow \infty, \quad |p_{i\perp}| \sim |p_{j\perp}|, \quad (2.1)$$

where we have defined $p_\perp = p_x + ip_y$ and i, j run over all final state partons. This limit is also referred to as the *Multi-Regge Kinematic* (MRK) limit. We will investigate what effect this limit has on our calculations and why we should be worried about our perturbative expansion. In order to do so, let us first make some statements about the Mandelstam variables in a $2 \rightarrow 2$ process. We introduce the *rapidity* of a particle;

$$y = \frac{1}{2} \ln \left(\frac{E + p_z}{E - p_z} \right), \quad (2.2)$$

which is a convenient parameter to work with in this limit. Given the rapidity of a particle and its angle with respect to the beam line (defined as the z -axis), we can parametrise an outgoing momentum in the following fashion;

$$p_i = |p_{i\perp}| (\cosh(y_i), \cos(\phi_i), \sin(\phi_i), \sinh(y_i)). \quad (2.3)$$

This allows for the following evaluation of the Mandelstam variable \hat{s} ;

$$\hat{s} = (p_1 + p_2)^2 = 2|p_{1\perp}||p_{2\perp}| (\cosh(\Delta y) - \cos(\Delta\phi)), \quad (2.4)$$

with $\Delta y = y_1 - y_2$ and $\Delta\phi = \phi_1 - \phi_2$. Since the MRK limit takes \hat{s} to infinity while keeping the transverse momentum fixed, we must have that the cosh becomes large and so $|\Delta y| \rightarrow \infty$. In other words, the MRK limit is the limit where all pairs of outgoing particles are separated by a large rapidity gap. Since we require that the transverse components of the momenta are much smaller in comparison to \hat{s} , then we must have that $p_{a,z} \approx p_{1,z}$, $p_{b,z} \approx p_{2,z}$, $E_a \approx E_1$ and $E_b \approx E_2$. We

therefore have that, in the MRK limit;

$$\hat{s} \approx |p_{1\perp}| |p_{2,\perp}| \exp(\Delta y) \quad (2.5a)$$

$$\hat{t} = (p_a - p_1)^2 \approx -|p_{1\perp}|^2 \quad (2.5b)$$

$$\hat{u} = (p_a - p_2)^2 \approx (p_1 - p_2)^2 = -\hat{s}. \quad (2.5c)$$

We conclude from this that (since all transverse momenta are assumed to have approximately equal magnitude) it is the quantity $\frac{\hat{s}}{-\hat{t}} \approx \exp(\Delta y)$ that is the relevant variable for high energy scattering. Alternatively, we take Δy to be the relevant variable and relate this to $\log(\frac{\hat{s}}{-\hat{t}})$ - this is the basis for what we will call the *Leading Logarithmic* approach to scattering amplitudes.

2.1.1 $qQ \rightarrow qQ$ at LO and NLO in the High Energy Limit

Since we already have the full leading order result as given in equation 1.84, we can simply apply the MRK limit to that. This gives;

$$|M_{qQ \rightarrow qQ}^{MRK}|^2 = g_s^4 \times \frac{8}{9} \times \frac{\hat{s}^2}{|k_{1\perp}|^2 |k_{2\perp}|^2}. \quad (2.6)$$

We see that we lose some information about the amplitude (we ‘lost’ \hat{u} , which we saw came from the scattering of opposite helicity quarks and approximated the full \hat{t}) but it is the correct expression in the relevant limit, as evidenced in figure 2.1, where we plot the full LO and MRK limit of the $ud \rightarrow ud$ amplitude. The momenta are parametrised such that $p_1 = (40 \cosh(\Delta), 40, 0, 40 \sinh(\Delta))$ and $p_2 = (40 \cosh(-\Delta), -40, 0, 40 \sinh(-\Delta))$. We also deduce that $M \sim \hat{s}$, a scaling relationship that we will return to later.

For the next-to-leading order calculation, there are a number of diagrams that need to be taken into account, a selection of which are shown in figure 2.2. If we were interested in the full NLO expression, we would have to work out the contribution from each diagram and sum them up along with the LO calculation. However, we are now interested in expressions that are relevant in the MRK

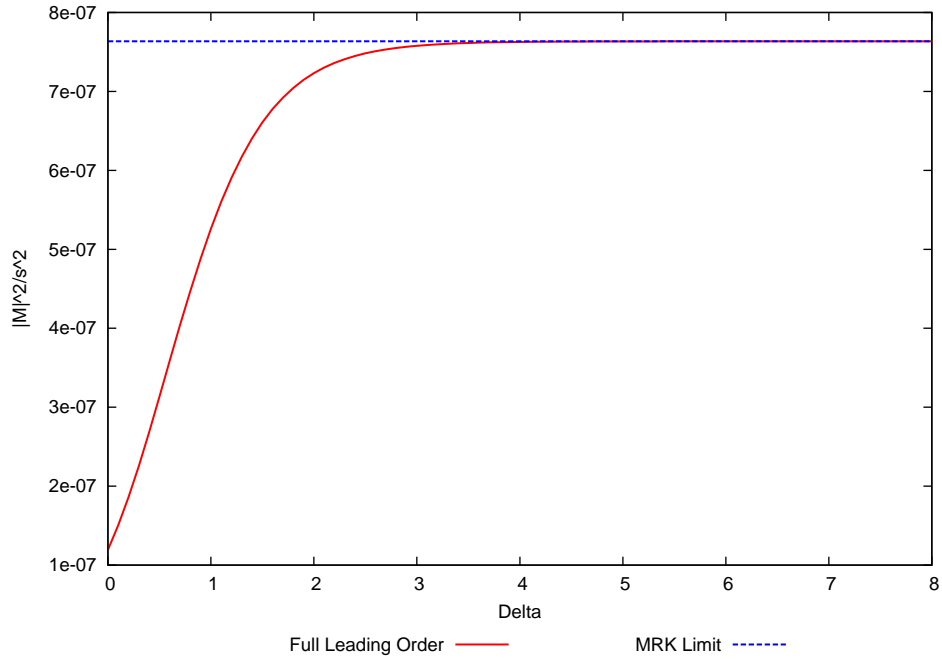


Figure 2.1 *Comparison of the full Leading Order calculation and the MRK limit of the process $ud \rightarrow ud$. A high value of Δ means that the final state particles are well separated in rapidity.*

regime only, so we should identify which diagrams are leading in that limit²; namely, diagrams that have a dependence on the rapidity gap between the two extremal partons. Therefore, we can expect that only loops that have ‘knowledge’ of this can give rise to an expression leading in $\log(\frac{\hat{s}}{-\hat{t}})$ - hence the terminology ‘Leading Log’ (LL). Self-energy diagrams of the quarks, such as the one on the top right of figure 2.2 clearly cannot be LL since the momenta of the other quark line does not enter into it and cannot influence the loop integral. A similar argument holds for the vertex correction diagrams, such as the one in the top left. For the self-energy diagram of the gluon (middle-right of the diagram) the propagators entering the loop are of the order of the transverse scale, which we keep fixed in comparison to a growing \hat{s} and so again cannot be leading. This leaves only the bottom two diagrams to be calculated, of which we need only to do one because we can relate one to the other (up to a colour factor we can just read off) via crossing symmetry. We choose to calculate the bottom-left diagram.

²This seems like a gauge dependent statement and indeed it is, but the argument that follows is valid for all covariant gauges which are the only ones we will use.

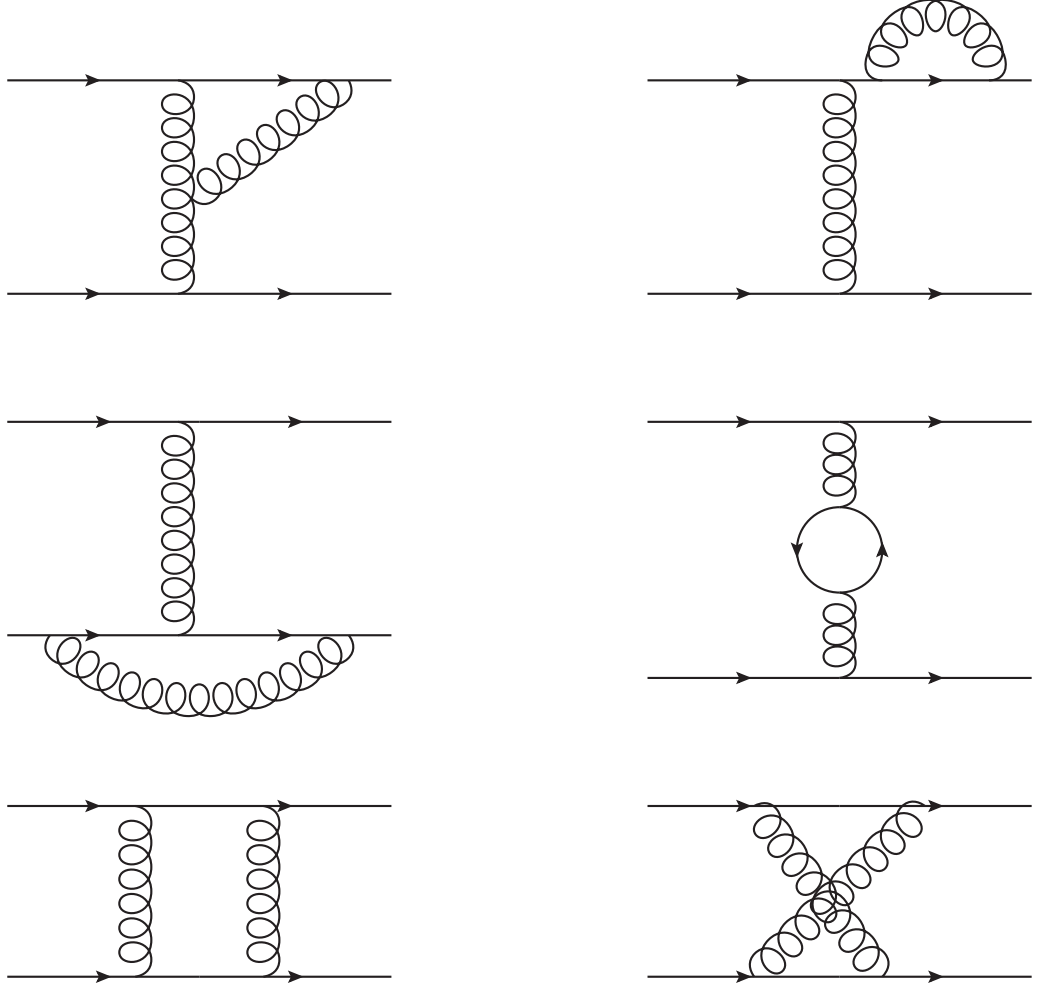


Figure 2.2 A selection of NLO diagrams for $qQ \rightarrow qQ$. We need only be interested in the bottom two.

Feynman diagrams that involve loops are, in general, difficult to calculate. There is a loop momentum which we need to integrate over that appears in a number of fermionic and gluonic propagators, the former leading to having to manage some cumbersome spinor algebra. Fortunately, there is a way to simplify the calculation for ourselves by use of the *Cutkosky rules* [20]. We can define the matrix S which encodes all possible ways a state $|i\rangle$ can evolve to a state $|f\rangle$, with elements;

$$S_{fi} = \delta_{fi} + i(2\pi)^4 \delta^4 \left(\sum_{i \in \text{initial}} p_i - \sum_{j \in \text{final}} p_j \right) M_{fi}, \quad (2.7)$$

where the δ_{fi} represents a process where no interaction occurs and the M_{fi} is the scattering matrix element we have been working with before. In matrix notation,

this can be written $S = \mathbb{1} + iT$ for the appropriate definition of T . Clearly, since the probability that an in state ends up in a particular out state, summed over all possible out states must be unity, the matrix S must be unitary; $S^\dagger S = \mathbb{1}$. This immediately leads to the non-trivial requirement;

$$2\text{Im}(T) = T^\dagger T. \quad (2.8)$$

We can project out a certain initial and final state;

$$\begin{aligned} 2\text{Im}(T_{fi}) &= \langle f|T^\dagger T|i\rangle \\ &= \sum_k \langle f|T^\dagger|k\rangle \langle k|T|i\rangle \\ &= \sum_k T_{kf}^* T_{ki} \\ &= \sum_k (2\pi)^4 \delta^4 \left(\sum_i p_i - \sum_k p_k \right) M_{kf}^* M_{ki}. \end{aligned} \quad (2.9)$$

where in the second line we have inserted a complete set of intermediate states $|k\rangle$.

This is a general statement about the full scattering amplitude. However, if we break this down into an order-by-order expression in the coupling, the statement allows one to relate diagrams at next-to-leading order (the left-hand side) to the product of other diagrams of leading order (the right-hand side). Using the Cutkosky rules, then, we can diagrammatically represent the imaginary part of the amplitude we are trying to work out as something like figure 2.3; we ‘cut’ the diagram vertically, setting the quark propagators the cut crosses on-shell and treating the process as a product of two leading order processes. Algebraically, this yields;

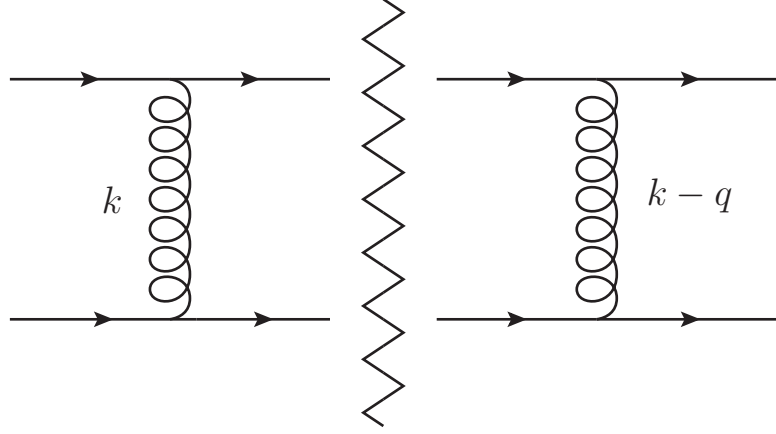


Figure 2.3 By ‘cutting’ our NLO diagram like this, we can find the imaginary part of the amplitude by considering a product of LO diagrams.

$$\begin{aligned}
\text{Im}(M_{NLO,1}) &= \frac{1}{2} \int d(\text{phase space}) M_{LO}(k) M_{LO}^\dagger(k - q) \\
&= \frac{1}{2} \int \frac{d^4 l}{(2\pi)^3} \frac{d^4 l'}{(2\pi)^3} \delta(l^2) \delta(l'^2) (2\pi)^4 \delta^4(p_a - p_b - l - l') M_{LO}(k) M_{LO}^\dagger(k - q) \\
&= \frac{1}{8\pi^2} \int d^4 k \delta((p_a - k)^2) \delta((p_b + k)^2) M_{LO}(k) M_{LO}^\dagger(k - q).
\end{aligned} \tag{2.10}$$

In the MRK limit, the leading order matrix element went like;

$$M_{LO,MRK} \sim g_s^2 \frac{2\hat{s}}{|k_\perp|^2}, \tag{2.11}$$

so it would be useful to write our integration over k^μ in terms of an explicit integration over k_\perp . We can do this by using a Sudakov parametrisation;

$$k^\mu = \rho p_a^\mu + \lambda p_b^\mu + k_\perp^\mu, \tag{2.12}$$

which allows us to switch our integration variables to ρ, λ and k_\perp , with the relation $d^4 k = \frac{1}{2} \hat{s} d\rho d\lambda d^2 k_\perp$. The High Energy Limit tells us that in this paramterisation,

both ρ and λ are much smaller than 1. Thus;

$$\begin{aligned}
\text{Im}(M_{NLO,1}) &= \frac{g_s^4 \hat{s}}{4\pi^2} \int d\rho d\lambda d^2 k_\perp \delta(-\hat{s}(1-\rho)\lambda + |k_\perp|^2) \\
&\quad \delta(\hat{s}(1+\lambda)\rho + |k_\perp|^2) \frac{\hat{s}}{|k_\perp|^2} \frac{\hat{s}}{|k_\perp - q_\perp|^2} \\
&\approx \frac{g_s^4 \hat{s}^3}{4\pi^2} \int d\rho d\lambda d^2 k_\perp \delta(-\hat{s}\lambda + |k_\perp|^2) \delta(\hat{s}\rho + |k_\perp|^2) \frac{1}{|k_\perp|^2} \frac{1}{|k_\perp - q_\perp|^2} \\
&= \frac{g_s^4 \hat{s}}{4\pi^2} \int d\rho d\lambda d^2 k_\perp \delta(-\lambda + |k_\perp|^2/\hat{s}) \delta(\rho + |k_\perp|^2/\hat{s}) \frac{1}{|k_\perp|^2} \frac{1}{|k_\perp - q_\perp|^2} \\
&= \frac{g_s^4 \hat{s}}{4\pi^2} \int d^2 k_\perp \frac{1}{|k_\perp|^2} \frac{1}{|k_\perp - q_\perp|^2}.
\end{aligned} \tag{2.13}$$

Since we are explicitly searching for terms proportional to $\Delta y = \ln\left(\frac{\hat{s}}{-\hat{t}}\right)$, then the calculation of the imaginary part immediately yields the real part, since;

$$\ln\left(\frac{\hat{s}}{-\hat{t}}\right) = \ln\left|\frac{\hat{s}}{\hat{t}}\right| - i\pi. \tag{2.14}$$

In effect, the pure existence of an imaginary part shows that this loop diagram contains this logarithm. Our real part, therefore, is;

$$\text{Re}(M_{NLO,1}) = \ln\left|\frac{\hat{s}}{\hat{t}}\right| \frac{-g_s^4 \hat{s}}{4\pi^3} \int d^2 k_\perp \frac{1}{|k_\perp|^2} \frac{1}{|k_\perp - q_\perp|^2}. \tag{2.15}$$

Kinematically, the other diagram we need to calculate is equivalent to this diagram under the exchange $\hat{s} \rightarrow \hat{u}$. But since in the MRK limit $\hat{s} \approx -\hat{u}$, the diagrams have the same form up to a minus sign. If there was no colour structure, the total amplitude would therefore be zero! However, we do have a

colour structure which we must now treat;

$$\begin{aligned}
C_{NLO,1} - C_{NLO,2} &= t_{q_2 q_\alpha}^b t_{q_\alpha q_b}^a t_{q_1 q_\beta}^b t_{q_\beta q_a}^a - t_{q_2 q_\alpha}^a t_{q_\alpha q_b}^b t_{q_1 q_\beta}^b t_{q_\beta q_a}^a \\
&= [t^b, t^a]_{q_2 q_b} t_{q_1 q_\beta}^b t_{q_\beta q_a}^a \\
&= \frac{i f^{bac}}{2} t_{q_2 q_b}^c ([t^b, t^a]_{q_1 q_a} + \{t^b, t^a\}_{q_1 q_a}) \\
&= \frac{i f^{bac}}{2} t_{q_2 q_b}^c [t^b, t^a]_{q_1 q_a} \\
&= \frac{-f^{bac} f^{bad}}{2} t_{q_2 q_b}^c t_{q_1 q_a}^d \\
&= \frac{-C_A \delta^{cd}}{2} t_{q_2 q_b}^c t_{q_1 q_a}^d \\
&= \frac{-C_A}{2} C_{Tree},
\end{aligned} \tag{2.16}$$

where $C_A = N = 3$ is a constant associated to the $SU(3)$ group. We see that the colour factor here is simply a constant multiplied by the tree level colour factor. With a small amount of manipulation and using $\hat{t} \approx -q_\perp^2$, we can then write the leading part of the NLO amplitude as proportional to the tree-level amplitude;

$$M_{NLO} = M_{LO} \ln \left(\frac{\hat{s}}{-\hat{t}} \right) \hat{\alpha}(q_\perp^2), \tag{2.17}$$

with;

$$\hat{\alpha}(q_\perp^2) = \frac{C_A \alpha_s}{4\pi^2} \int d^2 k_\perp \frac{-q_\perp^2}{k_\perp^2 (k_\perp - q_\perp)^2}. \tag{2.18}$$

This form of the amplitude clearly shows the dependence on the large logarithm. Even though $\hat{\alpha}$ contains a factor of α_s which should be small in order for our perturbation theory to make sense, the log is large enough to overcome this suppression such that the product $\alpha_s \ln \left(\frac{\hat{s}}{-\hat{t}} \right)$ is of order 1. Therefore, as a matter of principle, this correction is as important as the leading order contribution and should not be ignored. In fact, terms proportional to $\alpha_s^n \ln^{n-1} \left(\frac{\hat{s}}{-\hat{t}} \right)$ continue to appear at *every order* [33] and so, by the same argument, we should not ignore these contributions either. We therefore find ourselves in need of an all-order treatment of scattering amplitudes in the High Energy Limit. We will now see how the High Energy Jets (HEJ) framework does this.

2.2 HEJ Amplitudes

We have seen how taking the full MRK limit on the $qQ \rightarrow qQ$ amplitude allowed us to derive a result for the NLO virtual corrections to the process. The simplicity of that procedure should give us hope to find a way of generalising the result to obtain the virtual corrections at all orders. If we want to describe all LHC processes, however, we have a few more things to consider beforehand. Firstly, we need to account for different parton types in the incoming state. It is not clear a priori whether $qg \rightarrow qg$ and $gg \rightarrow gg$ should behave as nicely in this limit, since the LO contribution contains more diagrams than the t-channel one alone. Secondly, we should account for extra final states; i.e., generalise to a $2 \rightarrow n$ process. This will also be important when we want to calculate real corrections to our amplitudes, which is a subject we haven't yet touched upon. We will tackle each of these concerns individually.

2.2.1 $qg \rightarrow qg$ in the High Energy Limit

We can demonstrate how the High Energy Limit relates quarks to gluons by taking the limit on the LO $qg \rightarrow qg$ amplitude and comparing it to the $qQ \rightarrow qQ$ amplitude. There are a total of 3 diagrams we must consider which are shown in figure 2.4. Keeping with how the $qQ \rightarrow qQ$ amplitude was calculated, we will consider the helicity configuration $q^+g^+ \rightarrow q^+g^+$. Since we have an external gluon now we also have gluon polarisation vectors in our calculation. Such vectors have a gauge redundancy and so we must choose a certain gauge to work in. If we take the incoming gluon to have momentum p_b and the outgoing to have momentum p_2 , it turns out to be useful to use the following parametrisation for the vectors

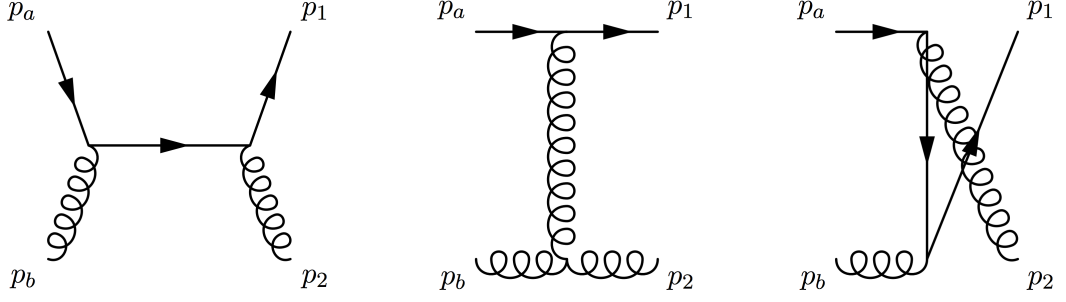


Figure 2.4 The three diagrams (s , t , and u channels) for $qg \rightarrow qg$ scattering at LO.

[5, 26];

$$\varepsilon_{2\rho}^{+*} = \frac{\langle 2^+ | \rho | b^+ \rangle}{\sqrt{2} \langle b2 \rangle}, \quad (2.19a)$$

$$\varepsilon_{2\rho}^{-*} = -\frac{\langle b^+ | \rho | 2^+ \rangle}{\sqrt{2} [b2]}, \quad (2.19b)$$

$$\varepsilon_{b\rho}^+ = -\frac{\langle 2^+ | \rho | b^+ \rangle}{\sqrt{2} [2b]}, \quad (2.19c)$$

$$\varepsilon_{b\rho}^- = \frac{\langle b^+ | \rho | 2^+ \rangle}{\sqrt{2} \langle 2b \rangle}. \quad (2.19d)$$

We conduct the calculation by moving from left to right in figure 2.4 and thus begin with the s -channel diagram. The Feynman rules give us;

$$\begin{aligned} M_s &= \bar{u}_1^+ (-ig_s \gamma^\nu T_{1q}^2) \left(\frac{i(\not{p}_a + \not{p}_b)}{\hat{s}} \right) (-ig_s \gamma^\mu T_{qa}^b) u_a^+ \varepsilon_{2\nu}^{+*} \varepsilon_{b\mu}^+ \\ &= \frac{ig_s^2 T_{1q}^2 T_{qa}^b}{2\hat{s} \langle b2 \rangle [2b]} \langle 2^+ | \nu | b^+ \rangle \langle 2^+ | \mu | b^+ \rangle \langle 1^+ | \gamma^\nu (\not{p}_a + \not{p}_b) \gamma^\mu | a^+ \rangle \\ &= \frac{-ig_s^2 T_{1q}^2 T_{qa}^b}{\hat{s} \hat{t}} \langle 2^+ | \nu | b^+ \rangle \langle 2^+ | \mu | b^+ \rangle p_a^\mu \langle 1 | \nu | a \rangle, \end{aligned} \quad (2.20)$$

where in the last line we have used the completeness relation to expand the \not{p} terms along with some of our spinor helicity identities. The t -channel diagram

gives us;

$$M_t = \bar{u}_1^+ (-ig_s \gamma^\mu T_{1a}^g) u_a \left(\frac{-i\eta_{\mu\nu}}{\hat{t}} \right) f^{g2b} (-g_s) (\eta^{\nu\rho} (2p_2 - p_b)^\sigma - \eta^{\rho\sigma} (p_2 + p_b)^\nu + \eta^{\sigma\nu} (2p_b - p_2)^\rho) \varepsilon_{2\rho}^{+*} \varepsilon_{b\sigma}^+, \quad (2.21)$$

but, since $p_{2/b}$ dotted with any of the polarisation vectors is zero and the two polarisation vectors themselves dotted together (with the chosen helicities) is also zero, we see that;

$$M_t = 0. \quad (2.22)$$

It is important to realise that this result only holds because of the gauge we picked for our gluons; only the final result which is the sum of all diagrams is the gauge invariant quantity. Thus though it may seem surprising at first that the t -channel diagram is zero given that we are trying to show that the High Energy Limit is dominated by t -channel poles, it is simply an expression of the freedom of our gauge choice. The final diagram is the u-channel;

$$\begin{aligned} M_u &= \bar{u}_1^+ (-ig_s \gamma^\nu T_{1q}^b) \left(\frac{i(\not{p}_a - \not{p}_2)}{\hat{u}} \right) (-ig_s \gamma^\mu T_{qa}^2) u_a^+ \varepsilon_{b\nu}^{+*} \varepsilon_{2\mu}^+ \\ &= \frac{ig_s^2 T_{1q}^b T_{qa}^2}{2\hat{u} \langle b2 \rangle [2b]} \langle 2^+ | \nu | b^+ \rangle \langle 2^+ | \mu | b^+ \rangle \langle 1^+ | \gamma^\nu (\not{p}_a - \not{p}_2) \gamma^\mu | a^+ \rangle \\ &= \frac{-ig_s^2 T_{1q}^b T_{qa}^2}{\hat{u} \hat{t}} \langle 2^+ | \nu | b^+ \rangle \langle 2^+ | \mu | b^+ \rangle p_a^\mu \langle 1 | \nu | a \rangle. \end{aligned} \quad (2.23)$$

We see therefore that;

$$M_{q^+g^+ \rightarrow q^+g^+}^{LO} = \frac{-ig_s^2}{\hat{t}} \langle 2^+ | \nu | b^+ \rangle \langle 2^+ | \mu | b^+ \rangle p_a^\mu \langle 1^+ | \nu | a^+ \rangle \left(\frac{T_{1q}^2 T_{qa}^b}{\hat{s}} + \frac{T_{1q}^b T_{qa}^2}{\hat{u}} \right). \quad (2.24)$$

We recall now that in the High Energy Limit, $\hat{u} \approx -\hat{s}$. We can also approximate

that;

$$\langle 2^+ | \mu | b^+ \rangle p_a^\mu \approx 2p_b \cdot p_a = \hat{s}. \quad (2.25)$$

Applying the limit to our result and we see that;

$$M_{q^+g^+ \rightarrow q^+g^+}^{LO,HE} = \frac{g_s^2 f^{2bc} T_{1a}^c}{\hat{t}} \langle 2^+ | \nu | b^+ \rangle \langle 1^+ | \nu | a^+ \rangle, \quad (2.26)$$

and therefore the amplitude is expressible as proportional to a t -channel pole. Furthermore, by taking the absolute square of this along with the colour sum, we find that;

$$|M_{q^+g^+ \rightarrow q^+g^+}^{LO,HE}|^2 = \frac{C_A}{C_F} |M_{q^+Q^+ \rightarrow q^+Q^+}^{LO,HE}|^2, \quad (2.27)$$

where, for the $SU(3)$ group, we have $C_A = 3$ and $C_F = \frac{4}{3}$. We therefore have that the High Energy Limit relates quarks to gluons in a very simple way; namely, via the multiplication of a colour factor. We find that this result holds for the other ‘helicity conserving’ amplitudes (i.e., the amplitudes where both the quark and gluon do not flip helicities in the scattering) and that the ‘helicity non-conserving’ amplitudes are identically zero, so we can in fact generalise this to;

$$|M_{qg \rightarrow qg}^{LO,HE}|^2 = \frac{C_A}{C_F} |M_{qQ \rightarrow qQ}^{LO,HE}|^2. \quad (2.28)$$

Of course, this equality only holds in the full High Energy limit and so we should expect differences with our approximation and the full LO calculation away from the limit. However, we can improve this slightly by instead multiplying by a momentum dependent colour factor. Such a factor was found in [5] and named the *Colour Acceleration Multiplier*;

$$\tilde{C}_A = \frac{1}{2} \left(C_A - \frac{1}{C_A} \right) \left(\frac{p_b^-}{p_2^-} + \frac{p_2^-}{p_b^-} \right). \quad (2.29)$$

It is clear that this tends to C_A in the limit where $p_2^- \sim p_b^-$. By using this multiplication factor instead of the straight C_A allows for the approximation to be more accurate away from the strict high energy limit and we therefore employ

this in the rest of this thesis (and, indeed, in the HEJ formalism itself).

2.2.2 Regge Theory and the Connection to High Energy

$2 \rightarrow n$ Amplitudes

It is instructive here to take a short detour into the realm of Regge theory which relates to properties of general scattering processes. In particular, before the advent of a full QCD theory to work with, the relativistic form of Regge theory allowed for some predictions to be made about strongly interacting particles. More specifically, it predicts that in the High Energy Limit we are working with, the amplitude of a given scattering process should behave as the Mandelstam variable s raised to the power of the spin of the particle exchanged in the t -channel (denoted by $\alpha(t)$);

$$M_{\text{Regge}} \sim s^{\alpha(t)}. \quad (2.30)$$

A more complete description of the history of the use of Regge theory applied to strong dynamics can be found in [33]. For our purposes, we need only remark that the expression generalises if there is instead a ‘chain’ of exchanged particles in the t -channel like that shown in figure 2.5, and we describe such a configuration as ‘Multi-Regge Kinematical’;

$$M_{\text{Multi-Regge}} \sim s_{12}^{\alpha(t_1)} s_{23}^{\alpha(t_2)} \dots s_{n-1,n}^{\alpha(t_{n-1})}. \quad (2.31)$$

We have already seen in $qQ \rightarrow qQ$ scattering that the amplitude did indeed, in the MRK limit, behave as s^1 . Since our only two choices of particles involved in t -channel exchange are the spin-one gluon and the spin-half quark, clearly all leading amplitudes in this limit must only have gluons exchanged. The only thing that can be emitted off of a t -channel gluon is another gluon (any quark must be accompanied by an anti-quark, with an intermediate t -channel quark propagator) and so we need only consider extra gluon emissions from our base $2 \rightarrow 2$ processes to capture all the leading contributions. Such configurations are also referred to as ‘Fadin-Kuraev-Lipatov’ or simply ‘FKL’ configurations, named after the three scientists who developed the formalism. Use of this fact and the study of amplitudes within the strict MRK limit [6, 22] show that the analytical

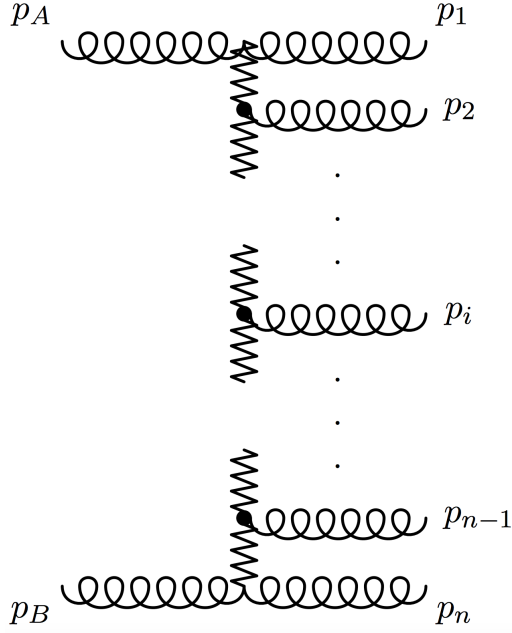


Figure 2.5 *A schematic representation of an example MRK amplitude. This figure is originally used in [6].*

form of the amplitude is;

$$|M_{f_1 f_2 \rightarrow f_1 g \dots g f_2}^{MRK}|^2 = \left(\frac{4\hat{s}^2}{N_c^2 - 1} \right) \frac{g^2 C_{f_1}}{|p_{1\perp}|^2} \left(\prod_{i=2}^{n-1} \frac{4g^2 C_A}{|p_{i\perp}|^2} \right) \frac{g^2 C_{f_2}}{|p_{n\perp}|^2}, \quad (2.32)$$

where C_{f_1}, C_{f_2} are C_F, C_A depending on whether the incoming particles are quarks or gluons respectively. However, like we saw when we took the explicit limit of the $qQ \rightarrow qQ$ amplitude, this limit is only really physically useful for a small amount of the available phase space that the LHC explores. On the other hand, the analytic expression is remarkably simple and at high gluon multiplicities it is much more practical to calculate than a full LO expression. Ideally, we would like to have something that bridges the gap between these two points; an expression that follows more closely the full LO matrix element in the LHC phase space whilst at the same time being simple enough such that we can evaluate it for processes with large numbers of final state gluons. The formulation of such amplitudes is one of the cornerstones of HEJ.

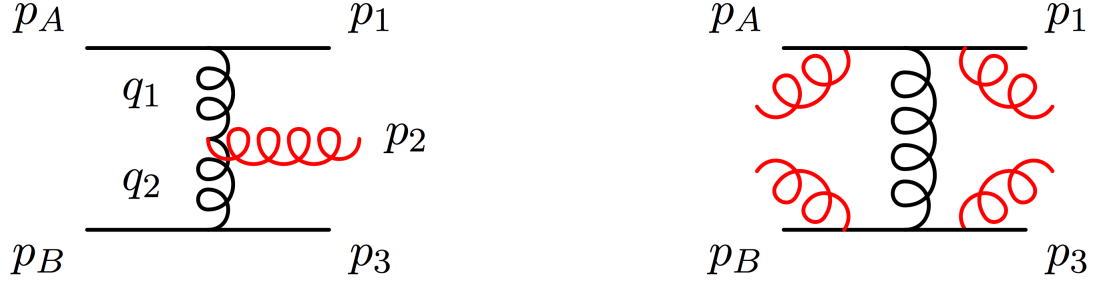


Figure 2.6 The five possibilities for an extra gluon emission. This figure is originally used in [6].

2.2.3 $qQ \rightarrow qgQ$ in the High Energy Limit

A good basis for finding a simple formulation for gluon emission away from the full MRK limit is to consider an extra emission in our qQ scattering process, since the only possible choice there is $qQ \rightarrow qgQ$. There are a total of five diagrams for this which are shown in 2.6. Before we take on the calculation, let us first take a detour to discuss the *Eikonal Approximation*.

The Eikonal Approximation is a way of simplifying the structure of some vertex functions in the limit where a momentum becomes very small. We will show that this approximation is also valid for situations where a momentum is not small in an absolute sense but small compared to other momenta in the problem. This is best seen by considering an example. Take a quark-quark-gluon vertex like the one shown in figure 2.7, where the quark line connects to a larger diagram on the left-hand side and the gluon is a final state particle. The Feynman rules for such a part of the diagram give an expression that goes like $\bar{u}(p)\gamma^\mu(\not{p} + \not{k})/(p+k)^2$. If we imagine that our quark is not deflected much by this emission, then we can take the limit $k \ll p$. This gives;

$$\begin{aligned}
 \frac{\bar{u}(p)\gamma^\mu(\not{p} + \not{k})}{(p+k)^2} &\approx \frac{\bar{u}(p)\gamma^\mu \not{p}}{2p \cdot k} \\
 &= \frac{\bar{u}(p)\gamma^\mu \gamma^\alpha p_\alpha}{2p \cdot k} \\
 &= \frac{\bar{u}(p)(2\eta^{\mu\alpha} - \gamma^\alpha \gamma^\mu)p_\alpha}{2p \cdot k} \\
 &= \bar{u}(p) \frac{p^\mu}{p \cdot k},
 \end{aligned} \tag{2.33}$$

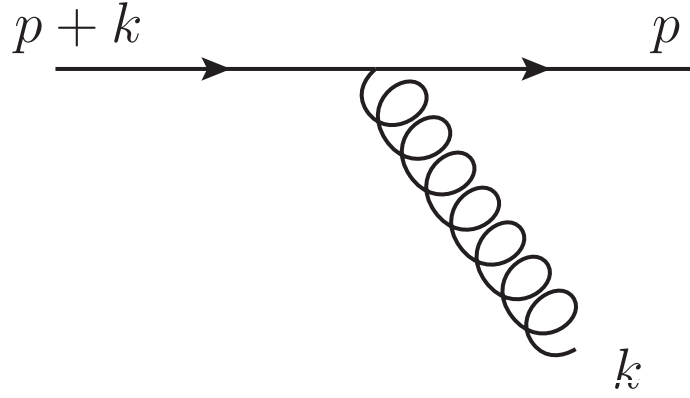


Figure 2.7 *The emission of a gluon from a quark line. By taking the limit $k \ll p$, we obtain the Eikonal rule.*

where in the last line we have used $\bar{u}(p)\not{p} = 0$ by virtue of the Dirac equation. A similar result holds if we replace our quarks with gluons as well, so the approximation is ‘blind’ to the spin of the particle emitting the gluon, an effect that allows us to very easily relate quarks and gluons in the high energy limit even as the final state multiplicity increases. We thus see that the leading terms in the High Energy limit are equivalent to the leading terms in the Eikonal limit.

Using this approximation, we can calculate the four diagrams with a gluon emitted off the extremal legs straightforwardly. The result of adding all these contributions together gives;

$$M_{eik} = M_{qQ \rightarrow qQ}(ig_s)\varepsilon_\rho^* \left(C_1 \frac{p_1^\rho}{p_1 \cdot p_2} - C_2 \frac{p_a^\rho}{p_a \cdot p_2} + C_3 \frac{p_3^\rho}{p_3 \cdot p_2} - C_4 \frac{p_b^\rho}{p_b \cdot p_2} \right). \quad (2.34)$$

The form of the approximation makes it clear that the (kinematic part of the) amplitude must be proportional to the $qQ \rightarrow qQ$ amplitude. The last diagram, however, involves emission off the t-channel exchanged gluon and so it’s not clear if this will be simply proportional to the $qQ \rightarrow qQ$ result as well. The relevant part of this diagram is;

$$M_{3g} \sim \langle 1|\mu|a \rangle (-g_s)(\eta^{\mu\rho}(q_1 + p_2)^\nu + \eta^{\rho\nu}(-p_2 + q_2)^\mu + \eta^{\nu\mu}(-q_2 - q_1)^\rho) \langle 3|\nu|b \rangle \varepsilon_\rho^*, \quad (2.35)$$

where $q_1 = p_a - p_1$ and $q_2 = p_a - p_1 - p_2 = p_3 - p_b$. In the high energy limit, we have already discussed how the extremal partons in the amplitude have momenta similar to the incoming particles; in other words, $p_1 \sim p_a$ and $p_3 \sim p_b$. In turn, this means that $\langle 1|\mu|a\rangle \sim 2p_a^\mu$ and $\langle 3|\nu|b\rangle \sim 2p_b^\nu$. Applying these approximations to our amplitude, then;

$$\begin{aligned} M_{3g} &\sim (-g_s)\varepsilon_\rho^*(2p_b^\rho(s_{1a} + 2s_{a2}) - 2p_a^\rho(s_{3b} + 2s_{2b}) + 2\hat{s}(-q_2 - q_1)^\rho) \\ &\approx (-2\hat{s}g_s)\varepsilon_\rho^*\left(2p_b^\rho\frac{s_{a2}}{\hat{s}} - 2p_a^\rho\frac{s_{2b}}{\hat{s}} + (q_1 + q_2)^\rho\right), \end{aligned} \quad (2.36)$$

since $s_{1a} \ll s_{2a}$ and $s_{3b} \ll s_{b2}$. Reinstating the factors from the rest of the diagram and rewriting the $2\hat{s}$ we factorised outside as once again $\langle 1|\mu|a\rangle \langle 3|\mu|b\rangle$, then;

$$M_{3g} = M_{qQ \rightarrow qQ} C_t (-g_s)\varepsilon_\rho^*\left(2p_b^\rho\frac{s_{a2}}{\hat{s}} - 2p_a^\rho\frac{s_{2b}}{\hat{s}} + (q_1 + q_2)^\rho\right), \quad (2.37)$$

and therefore the $qQ \rightarrow qQ$ amplitude does indeed completely factor out in this limit. We now turn our attention to the colour factors;

$$\begin{aligned} C_1 - C_2 &= t_{b2}^g t_{1q}^e t_{qa}^g - t_{b2}^g t_{1q}^g t_{qa}^e \\ &= i f^{gec} t_{a1}^c t_{b2}^g \\ &= -i C_t, \end{aligned} \quad (2.38)$$

and similarly $C_3 - C_4 = i C_t$. The sum of all the diagrams are then proportional to the same colour factor and to the $qQ \rightarrow qQ$ amplitude. Putting everything together, we can then write;

$$M_{qQ \rightarrow qgQ} = g_s^3 C_t \varepsilon_\rho^* \frac{\langle 1|\mu|a\rangle \langle 3|\mu|b\rangle}{q_1^2 q_2^2} V^\rho(q_1, q_2), \quad (2.39)$$

where;

$$V^\rho(q_1, q_2) = -(q_1 + q_2)^\rho + p_a^\rho \left(\frac{q_1^2}{p_2 \cdot p_a} + 2 \frac{p_2 \cdot p_b}{p_a \cdot p_b} \right) - p_b^\rho \left(\frac{q_2^2}{p_2 \cdot p_b} + 2 \frac{p_2 \cdot p_a}{p_a \cdot p_b} \right) \quad (2.40)$$

is an *effective* or *Lipatov* vertex describing the emission of a gluon. Since this vertex was derived by approximating p_a with p_1 and p_b with p_3 , we can symmetrise this vertex in these momenta to ‘undo’ this approximation somewhat and it is this symmetrised version that is used in practice but adds nothing to the discussion here. The important point is that we can now construct an amplitude with any number of extra gluons by simply multiplying in the relevant number of Lipatov vertices. As previously discussed, the difference between amplitudes with initial state quarks and amplitudes with initial state gluons is an overall colour factor;

$$|\bar{M}_{f_1 f_2 \rightarrow f_1 g \dots g f_2}^t|^2 = \frac{1}{4(N_C^2 - 1)} \|S_{f_1 f_2 \rightarrow f_1 f_2}\|^2 \left(g_s^2 C_{f_1} \frac{1}{t_1}\right) \left(g_s^2 C_{f_2} \frac{1}{t_{n-1}}\right) \prod_{i=1}^{n-2} \left(\frac{-g_s^2 C_A}{t_i t_{i+1}} V^\mu(q_i, q_{i+1}) V_\mu(q_i, q_{i+1})\right), \quad (2.41)$$

where we have introduced the notation $\|S_{f_1 f_2 \rightarrow f_1 f_2}\|^2$ to represent the sum over helicities of the modulus squared of the contraction of currents that appears at tree-level. We have also used the result $\sum_{pol} \varepsilon_\mu \varepsilon_\nu^* \rightarrow -\eta_{\mu\nu}$ to contract the Lipatov vertex. In the full MRK limit, this is proportional to \hat{s}^2 as we saw earlier, but we are able to keep more information about the process by keeping the full dependence like this (for example, we will reproduce *exactly* the full LO $qQ \rightarrow qQ$ calculation in this manner, not just the MRK limit thereof). We can represent a HEJ amplitude pictorially as shown in figure 2.8. We see clearly how this expression has the simplicity of the full MRK expression whilst at the same time being more flexible and able to describe better the matrix element away from this limit.

2.3 Resummation Technique

So far, we have derived an approximation to the LO matrix element for a certain subset of $2 \rightarrow n$ processes. We will now show that the form of this approximation allows for the capture of the high energy leading logarithmic terms of the amplitude *to all orders in perturbation theory*.



Figure 2.8 A schematic view of a HEJ amplitude. The original image is present in [7].

2.3.1 Lipatov Ansatz

Earlier, we saw explicitly that the Leading Logarithmic contribution to the NLO correction for $qQ \rightarrow qQ$ scattering was given by multiplying the LO result by a factor as given by equation 2.18. One of the postulates of the *Lipatov Ansatz* is that this result exponentiates, such that the virtual corrections to this process to all orders are given by;

$$M_{qQ \rightarrow qQ}^{LO+virt} = M_{qQ \rightarrow qQ}^{LO} \times \exp [\hat{\alpha}(q_{\perp}) \Delta y], \quad (2.42)$$

where we have related Δy to the log as previously shown. The ansatz then goes further to say that this exponentiation holds in the MRK limit for any number of t -channel propagators present at the leading order, such that the virtual corrections are obtained by making the substitution;

$$\frac{1}{t_i} \rightarrow \frac{1}{t_i} \exp [\hat{\alpha}(q_{i,\perp}) \Delta y_{i,i+1}]. \quad (2.43)$$

In the appropriate limit, this ansatz has been proved to the sub-leading level [15, 30–32]. However, by inspection of the $\hat{\alpha}$ function given in equation 2.18, we see that it is clearly divergent; for small values of k_{\perp} in the integration region, the integrand tends to infinity. Such a divergence is called an *infrared divergence* and is a common problem in particle physics amplitudes involving massless particles. The problem arises because virtual corrections are not the only corrections we need to consider to an amplitude. We can also have the case where a real emission

has taken place but at an energy scale small enough that only a detector with infinite resolution could have detected it. Since such a detector cannot exist, there is no way of differentiating between a ‘pure’ $qQ \rightarrow qQ$ scattering and another one accompanied by the emission of a low energy (or ‘soft’) gluon. Such contributions are also divergent, but in such a way that when combined with the divergence in the virtual corrections, the divergence is cancelled away. We will show precisely how this happens in the next part. For now, we choose to use the technique of *dimensional regularisation* to rewrite our $\hat{\alpha}$ function in a more convenient way - that is, a way that makes the divergence clear. The formalism works by extending the dimensionality of the two-dimensional perpendicular component integral to $2 + 2\varepsilon$ dimensions. This will allow us to write the result as an expansion in ε , which will manifest our divergence as a term proportional to ε^{-1} . We must eventually take the limit $\varepsilon \rightarrow 0$, but we will see how this prescription allows us to remove the divergences from our theory in a neat and systematic way before we do so. A further note is that this dimensional shift also slightly alters the overall energy dimension of the integral and so we must introduce a scale μ to absorb this effect. The upshot is that we perform the integral in this convention and end up with;

$$\hat{\alpha}(q_{i\perp}, \varepsilon) = -g^2 C_A \frac{\Gamma(1-\varepsilon)}{(4\pi)^{2+\varepsilon}} \frac{2}{\varepsilon} \left(\frac{|q_{i\perp}|^2}{\mu^2} \right)^\varepsilon. \quad (2.44)$$

2.3.2 Combining Real and Virtual Corrections at All Orders

As already discussed, the real correction to the amplitude occurs when the momenta of an outgoing gluon becomes very small. Since the emissions are controlled entirely by the effective vertex, we then need to find the limit of the function as the momenta becomes small. It is a simple exercise to show that, if we denote the emitted momentum by p_2 as in figure 2.9, the soft limit is;

$$\lim_{p_2 \rightarrow 0} \frac{-V(q_1, q_2) \cdot V(q_1, q_2)}{\hat{t}_1 \hat{t}_2} = \frac{4}{|p_{2\perp}|^2}. \quad (2.45)$$

Therefore, the first real correction to $qQ \rightarrow qQ$ is;

$$|M_{qQ \rightarrow qQ}^{HE, 1RC}|^2 = \frac{||S_{qQ \rightarrow qQ}||^2}{4(N_c^2 - 1)} \frac{g^2 C_F}{\hat{t}_1} \frac{g^2 C_F}{\hat{t}_2} \left(\frac{4g^2 C_A}{|p_{2\perp}|^2} \right). \quad (2.46)$$

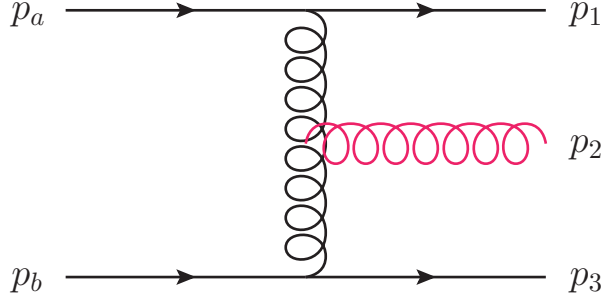


Figure 2.9 *If the momentum p_2 is small enough, we cannot detect the gluon emission and so treat it as a real correction to the $2 \rightarrow 2$ process.*

We need to regularise the soft divergence, so let us integrate this over the soft part of phase space (again, using dimensional regularisation) by introducing some soft transverse scale λ ;

$$\begin{aligned}
& \mu^{-2\varepsilon} \int_{soft} \frac{d^{3+2\varepsilon} p_2}{(2\pi)^{3+2\varepsilon} 2E_2} \left(\frac{4g^2 C_A}{|p_{2\perp}|^2} \right) \\
&= \mu^{-2\varepsilon} \int_0^\lambda \frac{d^{2+2\varepsilon} p_{2\perp}}{(2\pi)^{2+2\varepsilon}} \int_{y_1}^{y_3} \frac{dy_2}{4\pi} \left(\frac{4g^2 C_A}{|p_{2\perp}|^2} \right) \\
&= \mu^{-2\varepsilon} \frac{4g^2 C_A}{(2\pi)^{2+2\varepsilon} (4\pi)} (y_3 - y_1) \int_0^\lambda \frac{d^{2+2\varepsilon} p_{2\perp}}{|p_{2\perp}|^2} \\
&= \frac{g^2 C_A}{\pi (2\pi)^{2+2\varepsilon}} (y_3 - y_1) \frac{1}{\varepsilon} \frac{\pi^{1+\varepsilon}}{\Gamma(1+\varepsilon)} \left(\frac{\lambda^2}{\mu^2} \right)^\varepsilon.
\end{aligned} \tag{2.47}$$

By virtue of the Lipatov ansatz, the virtual corrections to the process are given by;

$$|M_{qQ \rightarrow qQ}^{HE,VC}|^2 = \frac{||S_{qQ \rightarrow qQ}||^2}{4(N_c^2 - 1)} \frac{g^2 C_F}{\hat{t}_1} \frac{g^2 C_F}{\hat{t}_2} \exp[2\hat{\alpha}(q_{1\perp}, \varepsilon)(y_1 - y_3)], \tag{2.48}$$

and so the first virtual correction is simply the exponential expanded to first order;

$$\begin{aligned}
|M_{qQ \rightarrow qQ}^{HE,1VC}|^2 &= \frac{||S_{qQ \rightarrow qQ}||^2}{4(N_c^2 - 1)} \frac{g^2 C_F}{\hat{t}_1} \frac{g^2 C_F}{\hat{t}_2} [2\hat{\alpha}(q_{1\perp}, \varepsilon)(y_1 - y_3)] \\
&= \frac{||S_{qQ \rightarrow qQ}||^2}{4(N_c^2 - 1)} \frac{g^2 C_F}{\hat{t}_1} \frac{g^2 C_F}{\hat{t}_2} \left[-4(y_3 - y_1) g^2 C_A \frac{\Gamma(1-\varepsilon)}{(4\pi)^{2+\varepsilon}} \frac{1}{\varepsilon} \left(\frac{|q_{1\perp}|^2}{\mu^2} \right)^\varepsilon \right].
\end{aligned} \tag{2.49}$$

We must now expand both of these results in ε , add them together and then take

the limit $\varepsilon \rightarrow 0$. Doing so yields;

$$\begin{aligned} \lim_{\varepsilon \rightarrow 0} |M_{qQ \rightarrow qQ}^{HE,1VC+1RC}|^2 &= \lim_{\varepsilon \rightarrow 0} \frac{||S_{qQ \rightarrow qQ}||^2}{4(N_c^2 - 1)} \frac{g^2 C_F}{\hat{t}_1} \frac{g^2 C_F}{\hat{t}_2} [\omega_0 + \mathcal{O}(\varepsilon)] \\ &= \frac{||S_{qQ \rightarrow qQ}||^2}{4(N_c^2 - 1)} \frac{g^2 C_F}{\hat{t}_1} \frac{g^2 C_F}{\hat{t}_2} \omega_0, \end{aligned} \quad (2.50)$$

with;

$$\omega_0 = \frac{g^2 C_A}{4\pi^2} \ln \left(\frac{\lambda^2}{|q_{1\perp}|^2} \right). \quad (2.51)$$

The argument clearly continues to higher orders and so we can immediately generalise the result to yield a full HEJ amplitude;

$$\begin{aligned} |M_{f_1 f_2 \rightarrow f_1 g \dots g f_2}^{HEJ}|^2 &= \frac{||S_{f_1 f_2 \rightarrow f_1 f_2}||^2}{4(N_c^2 - 1)} \frac{g^2 C_{f_1}}{\hat{t}_1} \frac{g^2 C_{f_2}}{\hat{t}_{n-1}} \\ &\quad \prod_{i=1}^{n-2} \frac{-g^2 C_A V(q_i, q_{i+1}) \cdot V(q_i, q_{i+1})}{\hat{t}_i \hat{t}_{i+1}} \\ &\quad \prod_{j=1}^{n-1} \exp [\omega_0(q_{j\perp})(y_{j+1} - y_j)]. \end{aligned} \quad (2.52)$$

The final comment to make about the HEJ amplitude is that we can extend it to also include the emission of a Higgs [7], a W^\pm [2] or a Z boson [4] along with the jets. The only difference is the form of the current contraction $S_{f_1 f_2 \rightarrow f_1 f_2}$. For the pure jets case, this is simply $j_\mu j^\mu$, the contraction of two pure quark currents. We can also define a current for the emission of, for example, a W boson as j_W^μ , which will depend on the momenta of the decay products of the W along with the momenta of the quark line. For a W process, then, we would have an object like $S_{f_1 f_2 \rightarrow f_1 f_2 e \nu} = j_W^\mu j_\mu$. The rest of the derivation then goes on like before.

2.4 Monte Carlo Implementation

We now have an expression for an all-order matrix element that is free of divergences in four spacetime dimensions. For physical relevance, we must now integrate the matrix element over the entire detector phase space of the LHC. The general expression for the integrand has already been shown in section 1.5. The way we do this complicated integral is via the technique of *Monte Carlo Integration* and we dedicate this section to explaining the process within the

context of our implementation.

2.4.1 The Motivation Behind Monte Carlo

To put it generally, Monte Carlo integration is a numerical integration technique that provides an estimate for a (usually very complicated or even analytically undoable) integral via use of random numbers. An insightful example of how it works is to consider how it can be used to estimate the value of π . Figure 2.10 shows a simple setup for how we might wish to do that. The area of the blue square is $(2R)^2$ and the area of the red circle is πR^2 . The ratio of the area of the circle to the area of the square is then $\pi/4$. If we were to pick a random point in the square (since we have only two dimensions here, this is the same as randomly sampling a pair of x and y coordinates) then there is a probability of $\pi/4$ that it also falls within the circle. Therefore, given N total choices of points within the square (or ‘trials’) of which M also fall inside the circle;

$$\pi \approx \frac{4M}{N}. \quad (2.53)$$

Of course, if we don’t conduct many trials N , our approximation will not be a good one because we have simply not sampled enough of the available space. As we increase our number of trials, however, the approximation gets closer to the real value of π , as evidenced³ in table 2.1. This is a consequence of the *law of large numbers*, a central mathematical law to the technique as a whole.

To make clear the relation to integral problems, we will discuss this problem again from a different point of view. We can think of the square which contains the circle as a two-dimensional ‘volume’ (more usually called ‘area’, of course, but we will introduce the more general term now) which bounds our system with value $V_2 = 4R^2$. Within this volume, we are trying to calculate another volume; namely, the area of the circle. Taking the origin of our co-ordinate system to be the centre of the circle, then the area of the circle is given by;

$$V_C = \int_0^R dr r \int_0^{2\pi} d\theta \equiv \int_{V_C} d\Omega. \quad (2.54)$$

³In fact, we tend to ‘bounce’ around the true value of π because the nature of our approximation means we are constantly switching between overestimating and underestimating the true value.

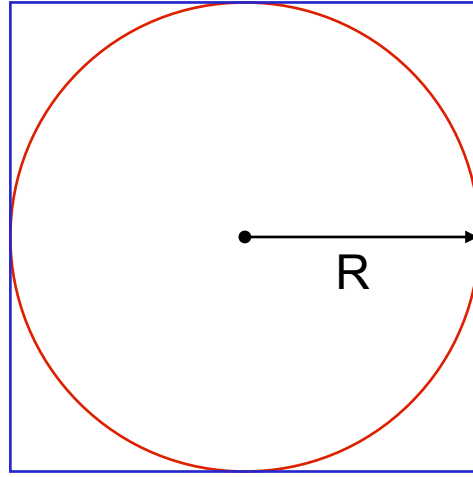


Figure 2.10 *A square with sides of length $2R$ enclosing a circle of radius R . We can estimate the value of π by picking random points in the square and seeing whether or not they also lie in the circle.*

Number of trials	Estimate of π
10^0	4
10^1	2
10^2	3.6
10^3	3.192
10^4	3.1644
10^5	3.1404
10^6	3.141828
10^7	3.14139320
10^8	3.14145576
10^9	3.14161324

Table 2.1 *Estimates of π via a simple Python Monte Carlo program for different numbers of trials.*

This is a particularly simple integral with value $V_C = \pi R^2$. In the initial formulation of the problem, we took this to be known but were ignorant on what the value of π numerically is. Instead, let us imagine that we didn't know how to perform the integral at all. We always know, however, that an integral (which we generalise to one depending on many variables) can be related to the average value of its integrand;

$$\langle f(\vec{x}) \rangle_{x \in V} = \frac{\int_V d\Omega f(\vec{x})}{V}. \quad (2.55)$$

The average can be estimated by simply sampling the integrand at N random points and then dividing by N . So long as the distribution of random points in

the volume is flat, the *Central Limit Theorem* guarantees that;

$$\int_V f(\vec{x}) d\Omega \approx V \langle f \rangle \pm V \sqrt{\frac{\langle f^2 \rangle - \langle f \rangle^2}{N}}, \quad (2.56)$$

with;

$$\langle f \rangle = \frac{1}{N} \sum_{i=1}^N f(\vec{x}_i), \quad (2.57a)$$

$$\langle f^2 \rangle = \frac{1}{N} \sum_{i=1}^N f^2(\vec{x}_i). \quad (2.57b)$$

It is important to note here that the error estimate is precisely that; an estimate that assumes the error is distributed in a Gaussian fashion. We clearly see that it scales as $N^{-\frac{1}{2}}$ which is rather slowly convergent but the important point is that it is *completely independent of the dimensionality* of the problem.

The last step is to increase the domain of integration to the larger area V_2 that encapsulates entirely V_C ;

$$\int_{V_C} d\Omega f = \int_{V_2} d\Omega f|_{V_C} \approx V_2 \langle f|_{V_C} \rangle \pm V_2 \sqrt{\frac{\langle f|_{V_C}^2 \rangle - \langle f|_{V_C} \rangle^2}{N}}. \quad (2.58)$$

Then, since in our original problem the integral we are interested in is simply the area integral, $f = 1$ if any chosen random point is within V_C and 0 otherwise. Thus, given N trials of which M lie inside the circle (we drop the error estimate now for brevity);

$$\begin{aligned} \int_{V_2} d\Omega 1|_{V_C} &= V_C \approx V_2 \frac{M}{N} \\ \therefore \frac{V_C}{V_2} &\approx \frac{M}{N}, \end{aligned} \quad (2.59)$$

which is the statement we started with.

We could imagine extending this experiment in two ways. Firstly, we could be interested in the behaviour of a more complicated function within a volume (i.e., a more complicated f). Secondly, we could also think about taking the problem into three dimensions by considering a sphere enclosed within a cube. Indeed, mathematically speaking, we could extend this into as many dimensions as we desire, to the point where we no longer have such an obvious geometric interpretation of the problem. It is precisely the arena of high-dimensionality integration problems with complicated integrands where Monte Carlo techniques come into their own.

2.4.2 Monte Carlo in High Energy Jets

We recall from section 1.5 that the integral we are trying to perform looks like;

$$\sigma_{pp \rightarrow n\text{-jet}}^{inc/exc} = \sum_{f_a, f_b} \int_0^1 dx_a \int_0^1 dx_b f_a(x_a, Q^2) f_b(x_b, Q^2) \times \hat{\sigma}_{partonic} \times \mathcal{J}(\text{n-jet}^{inc/exc}), \quad (2.60)$$

with;

$$\hat{\sigma}_{partonic} = S \times \frac{|M|^2}{F} \times (2\pi)^4 \delta^{(4)}(p_a + p_b - \sum_{f=1}^n p_f) \times \prod_{i=1}^n \int \frac{d^3 \vec{p}_i}{2E_i (2\pi)^3}, \quad (2.61)$$

and so the problem is clearly suited to evaluation by Monte Carlo methods. The general process is as follows;

1. Generate a number of partons for the final state.
2. Pick the flavours for the incoming state.
3. Generate the momenta for all partons.
4. Perform a basic cluster into jets to check whether this event will give something consistent with cuts. If it won't, throw away the point here.
5. Calculate the matrix element and multiply by other factors in the integrand.
6. Cluster into jets and check to see if they pass all imposed cuts on the process. If it does, add the calculated point to the estimation of the average.

7. Repeat.

Such a technique is perfectly acceptable and results can be achieved this way. However, if we are simply generating random numbers flatly in these steps then we are being needlessly inefficient. For example, we see from graphs of Parton Distribution Functions that there are clear areas where the value of it is much larger than at other points. If we simply generate flatly then we equally sample these two regions which will clearly hurt our convergence. Indeed, there is a technique to combat this called *importance sampling*.

Importance sampling is aimed at simply reducing as much as possible the value of $\sqrt{\langle f \rangle^2 - \langle f^2 \rangle} \equiv \sigma_{MC}$, also known as the *variance*, which we saw was directly related to the estimate of the error. To see how this achieved, let us consider a one-dimensional integral and utilise our freedom to multiply and divide by another (well-behaved) distribution $q(x)$;

$$\int_a^b dx f(x) = \int_a^b dx q(x) \frac{f(x)}{q(x)} = \int_a^b dx q(x) h(x). \quad (2.62)$$

We can then perform a change of variables;

$$\int_a^b dx q(x) h(x) = \int_{Q(a)}^{Q(b)} dy h(Q^{(-1)}(y)), \quad (2.63)$$

with $dQ(x)/dx = q(x)$. If we normalise $q(x)$ such that it integrates to unity over the integration domain, then the fundamental theorem for Monte Carlo integration shows;

$$\int_a^b dx f(x) = \int_a^b dx q(x) \frac{f(x)}{q(x)} \approx \left\langle \frac{f(x)}{q(x)} \right\rangle \pm \sqrt{\frac{\langle f^2(x)/q^2(x) \rangle - \langle f(x)/q(x) \rangle^2}{N}}. \quad (2.64)$$

Thus if we pick $q(x) = 1/(b-a)$, we arrive back at equation 2.56 (a one-dimensional volume is simply the length of the line), but we are not bound to make this choice - we should instead pick a $q(x)$ that minimises as much as possible the second term. There are a few subtleties and difficulties in doing this, but the upshot is that this is best achieved by sampling from a distribution $q(x)$

that is close to $f(x)$ in shape. This is done at many points in the HEJ program, including;

- Picking the incoming partons in such a way to more often sample those with a higher PDF value. The LHAPDF package [16] which contains a whole range of different PDF sets to choose from provides the value of f/x , so what we actually optimise for is the quantity $x \times f/x$.
- Generating transverse momenta skewed towards the lower end of the spectrum since the cross section falls off rapidly with p_{\perp} .
- Generating the rapidity of particles to more often create ‘valid’ configurations, where we keep the FKL rapidity ordering.

With such considerations, the variance of our estimate is greatly reduced and stable results can be obtained fairly quickly, depending on the precise nature of the analysis.

2.4.3 Concerning Partons and Jets

In the previous subsection it was remarked that at one step of our Monte Carlo program we check to see how the partons we have generated correspond to observed jets. How this is done is worthy of a longer discussion. The process by which hard partons produced by the scattering end up culminating in jets of hadrons is an inherently non-perturbative process; there is no such effect that arises naturally from the rules of our perturbation theory. The implication is clear; perturbation theory must break down at some point. The cause of this is that the value of the expansion parameter α_s is not a constant but ‘runs’ with the energy scale as shown in figure 2.11. At small energy scales, the parameter becomes large enough that a perturbative theory no longer makes sense. Thankfully, we can separate (or ‘factorise’) these low energy processes away from our high energy perturbative process so long as we have a defined way of estimating how many final state jets appear given a certain set of hard external partons. This has led to the development of *jet algorithms*.

There are two broad categories of algorithms; ‘Cone-Type’ and ‘Sequential Clustering’. The first type are heavily disfavoured by the theory community because of their tendency to be infrared unsafe and so we will focus on the second type. The general process for this type of algorithm is as follows;



Figure 2.11 *The value of α_s as evaluated at different energy scales Q^2 . At low energies, the value becomes large enough that a perturbative treatment of QCD is no longer valid. Original figure is present in [29].*

1. Define some distance measure d_{ij} that can be calculated between each pair of hard partons i, j and a distance d_{iB} between all particles and the beam line.
2. Compute all distances d_{ij} and d_{iB} and find the smallest.
3. If the smallest distance is a d_{ij} , then combine the momenta of the partons i, j and recalculate all distances. If the smallest is a d_{iB} , remove parton i from the process and call it a ‘jet’.
4. Repeat until all partons are clustered into jets.

The natural question, of course, is what we should choose for the distances d_{ij} and d_{iB} . The general form is;

$$d_{ij} = \min(k_{i\perp}^{2p}, k_{j\perp}^{2p}) \frac{\Delta_{ij}}{R} \quad \text{with} \quad \Delta_{ij} = \sqrt{(y_i - y_j)^2 - (\phi_i - \phi_j)^2} \quad (2.65)$$

$$d_{iB} = k_{i\perp}^{2p}.$$

The parameter R scales the d_{ij} with respect to d_{iB} such that any pair of final jets a, b are at least separated by $\Delta_{ab} = R$. For this reason, we often refer to R as a ‘jet radius’. The value of p can be chosen to govern the relative power of energy and geometrical scales in the distance parameter. There are three main algorithms which has three different choices for p ; the kT algorithm with $p = 2$, the Cambridge/Aachen with $p = 0$ and the anti-kT with $p = -2$. There are reasons why one might want to use one over the other and so one would wish for a simple way of changing between conventions in any computer program one wants to run. Fortunately, the *FastJet* library [17] does precisely this. For the user, the only requirement is to specify which algorithm is to be used at the start of the calculation. Any further calculations involving the jet objects are easily handled within the defined classes in the package.

2.4.4 Scale Variations

It has already been discussed that the value of a parton distribution function is dependent on the energy scale at which the proton is probed. We have now also seen that the value of the strong coupling constant α_s is also dependent on the energy scale it is being evaluated at. These two scales are called the *factorisation scale* μ_f and *renormalisation scale* μ_r respectively. Clearly, we need to make a choice for what these scales actually are before we can do any calculations. However, it is not clear at all what we should choose. We can imagine at least that the scales do not differ much and so we can simply to consider $\mu_f = \mu_r$. Still, we find there is no one good answer to this question and so we are left with the task of calculating *scale variations* in order to provide an estimate of uncertainty to our calculation arising from this. With HEJ, we by default allow for the input of four different scale choices;

1. Fixed scale.
2. Maximum jet p_\perp .
3. $H_T/2$, which is the scalar sum of all parton p_\perp divided by 2.
4. Invariant mass of the jets.

When calculating scale variations, we take the scale as defined and then vary independently μ_f and μ_r around it by factors of $2, \sqrt{2}, 1, \frac{1}{\sqrt{2}}, \frac{1}{2}$. Since there are

five choices for each scale, we overall have 25 different results. However, since we expect μ_f and μ_r to be close to each other, we remove the points where $\mu_f/\mu_r > \sqrt{2}$ or $\mu_r/\mu_f > \sqrt{2}$ which leaves us with 19 options. These will form bands around a central prediction which we then use as our estimation for the effect of scale variation for our results.

2.5 Experimental Analyses

We have spent the best part of this chapter arguing from a theoretical standpoint that the systematic treatment of High Energy logs is required for the accurate description of LHC data. We would then like to end this chapter by providing plots from actual LHC analyses to see if the experimental data actually agrees with that statement. HEJ has been used in a wide range of experimental analyses [9, 11–13, 18, 19, 21] and we present a few select plots for discussion here. To understand them all fully, we first need to explain a couple of other features of HEJ we have not yet presented.

Firstly, HEJ includes a multiplicative matching to full LO calculations for matrix elements up to and including four final state jets. After a process has been clustered into final state jets, the matrix element is recalculated with the jet momenta⁴ along with the full LO matrix element (currently provided by *MadGraph* [1]) and the process is multiplied by the ratio of the full LO to our matrix element. We also include full LO matrix elements for non-FKL processes, which we saw are sub-leading in the high energy limit. Including matching in this way allows HEJ to be as competitive as other approaches in areas far away from the high energy limit it is designed for.

Secondly, it is possible to interface HEJ with the *parton shower* ARIADNE [3]. A parton shower is designed to simulate the hadronisation of the event and as such is a completely distinct problem than that of calculating the hard, scattering matrix element that HEJ provides. The specifics of the technique are interesting [37] but beyond the scope of this thesis. The important point is that a combined HEJ+ARIADNE program can describe the high energy behaviour of the hard scattering element along with the soft behaviour of the parton shower.

⁴Since some partons may not make it into final state jets, momentum conservation may not necessarily hold here. This is solved by distributing the momenta of partons that are not included into the jets in such a way as to keep it as close as possible to the original jet momenta.



Figure 2.12 *Differential cross section in m_{12} bins in the ATLAS study [12]*

Figure 2.12 shows a range of predictions for a W plus at least two jet event, binned in the invariant mass between the most forward and backward jet. The tail of this distribution is precisely where we expect the high energy logs to become important. The failing of the fixed order approaches to describe this region well clearly shows that this is indeed the case. The error band on the HEJ prediction is large and comes from the scale variations; the scale variation bands are not included on the other generators in the plot and would be just as large, with the exception of the BlackHat line which is shown and smaller because it is an NLO calculation. It is clear even still that only HEJ shows flat behaviour in the ratio plot. Indeed, further investigation in [4] showed that this is purely a normalisation effect.

Figure 2.13 shows the cross section for a process involving at least four final state jets binned in H_T . The interesting feature of this plot is that HEJ continues to track the data out to high values of H_T , which correspondingly means high values of p_\perp for the jets. The High Energy limit that inspired HEJ holds only when the p_\perp of the final state particles are all much smaller than the centre of mass energy and therefore should not be expected to provide a good description in the regime probed here. We see that HEJ keeps enough of the full process and this, along with the matching procedure, allows for it to be a useful tool for describing data



Figure 2.13 *Differential cross section in H_T (the scalar sum of all jet momenta) bins in a four jet ATLAS study [13]*

even away from the limit it was designed for.

Figure 2.14 is a plot from an analysis involving a jet veto. A scale (in this case, 30 GeV) is chosen whereby any extra jet emission in a rapidity gap between a defined two-jet system (here, the most forward and backward jets) is vetoed. Such a measurement is useful for testing perturbative predictions on the absence of activity in the gap; for example, we see from our HEJ amplitude that a large Δy corresponds to a larger value of the resummation exponential. The predictions for both HEJ and HEJ+ARIADNE are shown for an observable related to the angular decorrelation of the dijet system. It is clear in this case that the best description of data comes only from having both the high energy and the parton shower effects included; in the early bins the partonic HEJ which only includes the former overshoots and the POWHEG line which only includes the latter undershoots.

All of these analyses were performed during the first run of the LHC and, at maximum, had a centre of mass energy of 8 TeV. Run II will provide us with data for events at a centre of mass energy of 14 TeV and so we expect that the effect of these high energy logs will become even more prevalent in future analyses.

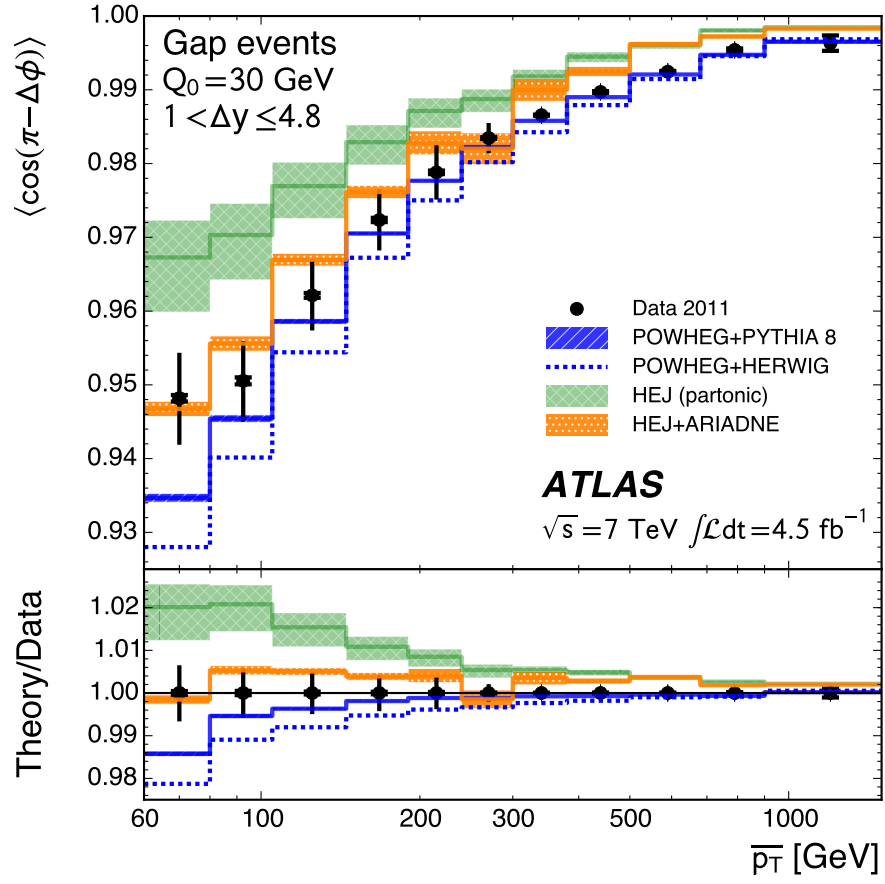


Figure 2.14 Plot of an azimuthal decorrelation observable in average p_\perp in the ATLAS analysis [11].

Chapter 3

Beyond Leading Log with High Energy Jets

Now that the driving principles behind HEJ have been explained, we move on to discuss the recent improvements to the formalism. We begin by discussing how the form of our amplitudes allows us to also capture terms which are Next-to-Leading Log (NLL) in the perturbative series. We will go into the motivations for why we should do this before presenting a full description of how some of these terms are derived and incorporated. We then finalise the chapter by presenting new results clearly showing the effect of the addition of these contributions, both in terms of the HEJ program and in comparison to real LHC data.

3.1 Motivations for NLL

There are a few reasons one might consider trying to go beyond Leading Log with the formalism. Firstly, since it has been proved that the Lipatov ansatz is valid at the NLL level, any sub-leading amplitude that still factors out into a product of t -channel poles can be resummed in precisely the same way as before; there is no added complication to the resummation procedure itself. The formalism thus lends itself naturally and readily to this extension. Secondly, by having access to these sub-leading terms we also expect to reduce the scale variation bands on our calculation, since these variations are directly related to how much ‘control’ we have over higher order terms. In order to claim full NLL accuracy, we must

have;

1. Calculations of FKL amplitudes but with the rapidity ordering of one emitted gluon disturbed. We call such contributions ‘unordered’ processes.
2. Corrections to the Lipatov vertex for the emission of gluons.
3. Calculations of inherently non-FKL amplitudes that appear at the NLL level.

The first point had already been implemented in theory but had not been incorporated into the program. The second point has not yet been attempted but remains a long term goal of the collaboration. This thesis will consider the first and final points, providing a brief overview of the former and a complete description and derivation of the author’s individual work for the latter. Including such considerations will mark an important step towards full NLL HEJ and, in the case of the addition of the non-FKL subprocesses, it extends the applicability of HEJ since we will now have a Leading Log description of these events; in conclusion, we will be able to resum more of the contribution to the cross section.

3.2 Unordered Emissions in Pure Jets

The derivation of the amplitude for an unordered (or simply ‘uno’) contribution revolves around extending our current formalism to include the effect of a gluon being emitted outside of the FKL strong rapidity ordered chain. We can express this by having a new ‘current’ that depends on the rapidity of this unordered parton and the parton next to it in rapidity that satisfies the ordering. For example, the amplitude for $qQ \rightarrow gqQ$ would look something like;

$$M_{qQ \rightarrow gqQ}^{uno} \sim \frac{j_{uno}^{\mu}(p_a, p_1, p_{uno}) j_{\mu}(p_b, p_2)}{\hat{t}_2}, \quad (3.1)$$

where $y_{uno} \sim y_1, y_1 \gg y_2$. In essence, we collapse the gluon emission to a point along the usual current such that there is only one suitable t -channel pole to be resummed as opposed to the two we would get if the gluon was emitted in the FKL ordering - it is thus clear to see why this is a sub-leading log contribution. Diagrammatically, we can show this like the schematic drawing in figure 3.1. We

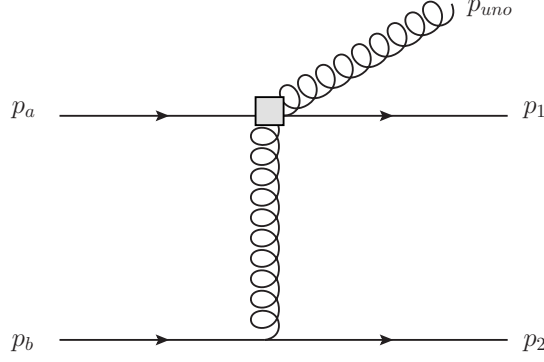


Figure 3.1 A schematical view of an unordered emission amplitude.

should also keep in mind that when it comes to discussing the colour properties of this amplitude that it will be more complicated than the FKL case and the result will have to be treated more carefully in this regard. To derive the form of the uno current, we will simply recalculate the $qQ \rightarrow gqQ$ amplitude but with the consideration that the rapidity of the gluon is no longer far away from the rapidity of the forward quark current. What this will essentially mean is that the kinematic arguments for dropping some terms like we did in section 2.2.3 will no longer be valid. We will therefore start by writing the full LO result for this amplitude (where we will write $p_{uno} = p_g$ for brevity);

$$\begin{aligned}
M_{qQ \rightarrow gqQ}^{LO} = & (ig_s)^3 T_{1i}^c T_{ia}^d T_{2b}^d \varepsilon_\nu(p_g) \frac{\langle 1|\nu|g \rangle \langle g|\mu|a \rangle + 2p_1^\nu \langle 1|\mu|a \rangle}{s_{1g} \hat{t}_2} \langle 2|\mu|b \rangle \\
& - (ig_s)^3 T_{1i}^d T_{ia}^c T_{2b}^d \varepsilon_\nu(p_g) \frac{2p_a^\nu \langle 1|\mu|a \rangle - \langle 1|\mu|g \rangle \langle g|\nu|a \rangle}{s_{ag} \hat{t}_2} \langle 2|\mu|b \rangle \\
& + (ig_s)^3 T_{2i}^c T_{ib}^d T_{1a}^d \varepsilon_\nu(p_g) \frac{\langle 2|\nu|g \rangle \langle g|\mu|b \rangle + 2p_2^\nu \langle 2|\mu|b \rangle}{s_{2g} \hat{t}_1} \langle 1|\mu|a \rangle \\
& - (ig_s)^3 T_{2i}^d T_{ib}^c T_{1a}^d \varepsilon_\nu(p_g) \frac{2p_b^\nu \langle 2|\mu|b \rangle - \langle 2|\mu|g \rangle \langle g|\nu|b \rangle}{s_{bg} \hat{t}_1} \langle 1|\mu|a \rangle \\
& - g_s^3 f^{dec} T_{1a}^d T_{2b}^e \varepsilon_\nu(p_g) \frac{\langle 1|\rho|a \rangle \langle 2|\mu|b \rangle}{\hat{t}_1 \hat{t}_2} (2p_g^\mu \eta^{\nu\rho} - 2p_g^\rho \eta^{\mu\nu} - (q_1 + q_2)^\nu \eta^{\mu\rho}).
\end{aligned} \tag{3.2}$$

With the full expression available, we can investigate which terms we can still drop in this new limit $y_g \sim y_1 \gg y_2$. We see that the first term in the third line and the second term in the fourth are the only ones we can drop because (depending on helicities) the μ contraction will give something that scales as $\sqrt{s_{ag}}$ or $\sqrt{s_{g1}}$ which are now small invariants in comparison to everything else.

By dropping these terms, all remaining terms are proportional to $\langle 2|\mu|b\rangle$ and so by comparison to equation 3.1, the sum of the terms multiplying this current is what will give us our unordered current. However, to be truly consistent with the factorised picture, we must factorise out the colour factor T_{2b}^d from this amplitude as well. This is already the case for the first, second and last lines and now that we have dropped terms for the other two lines we can use the still valid limit $p_2 \sim p_b$ to yield;

$$\begin{aligned}
& -ig_s^3 \langle 1|\mu|a\rangle \langle 2|\mu|b\rangle \varepsilon_\nu(p_g) \left(\frac{2p_2^\nu}{\hat{t}_1 s_{2g}} - \frac{2p_b^\nu}{\hat{t}_1 s_{bg}} \right) \\
& \approx -ig_s^3 \langle 1|\mu|a\rangle \langle 2|\mu|b\rangle \varepsilon_\nu(p_g) \frac{1}{\hat{t}_1} \frac{2p_b^\nu}{s_{bg}} T_{1a}^d (T_{2i}^c T_{ib}^d - T_{2i}^d T_{ib}^c) \\
& = g_s^3 \langle 1|\mu|a\rangle \langle 2|\mu|b\rangle \varepsilon_\nu(p_g) \frac{1}{\hat{t}_1} \frac{2p_b^\nu}{s_{bg}} f^{cde} T_{1a}^d T_{2b}^e \\
& = g_s^3 \langle 1|\mu|a\rangle \langle 2|\mu|b\rangle \varepsilon_\nu(p_g) f^{cde} T_{1a}^d T_{2b}^e \frac{1}{\hat{t}_1} \left(\frac{p_b^\nu}{s_{bg}} + \frac{p_2^\nu}{s_{2g}} \right), \tag{3.3}
\end{aligned}$$

where in the last line we have restored the symmetry between p_2 and p_b . Our factorised amplitude then looks like;

$$M_{qQ \rightarrow gqQ}^{uno, fact} = -g_s^3 \frac{\langle 2|\mu|b\rangle}{\hat{t}_2} T_{2b}^d (iT_{1i}^c T_{ia}^d U_1^{\mu\nu} + iT_{1i}^d T_{ia}^c U_2^{\mu\nu} + f^{ecd} T_{1a}^e L^{\mu\nu}), \tag{3.4}$$

where;

$$\begin{aligned}
U_1^{\mu\nu} &= \frac{1}{s_{1g}} (j_{1g}^\nu j_{ga}^\mu + 2p_1^\nu j_{1a}^\mu) \\
U_2^{\mu\nu} &= -\frac{1}{s_{ag}} (2j_{1a}^\mu p_a^\nu - j_{1g}^\mu j_{ga}^\nu) \\
L^{\mu\nu} &= \frac{1}{\hat{t}_1} \left(-2p_g^\mu j_{1a}^\nu + 2p_g \cdot j_{1a} \eta^{\mu\nu} + (q_1 + q_2)^\nu j_{1a}^\mu + \hat{t}_2 j_{1a}^\mu \left(\frac{p_2^\nu}{s_{2g}} + \frac{p_b^\nu}{s_{gb}} \right) \right). \tag{3.5}
\end{aligned}$$

The three colour factors are not independent here, so we can combine them and then we can extract the uno current by inspection;

$$j_{uno}^\mu(p_1, p_a, p_g) = i\varepsilon_\nu(p_g) (T_{1i}^c T_{ia}^d (U_1^{\mu\nu} - L^{\mu\nu}) + T_{1i}^d T_{1a}^c (U_2^{\mu\nu} + L^{\mu\nu})). \tag{3.6}$$

Gauge invariance of this expression has been checked by replacing the polarisation vector with the gluon momentum and seeing that the expression gives zero. This current can then be used as a basis for all unordered amplitudes, with further emissions added on via the Lipatov vertex and other incoming states accounted for by colour Casimir multiplications. One thing to note, however, is that the leg that the unordered current is dependent on cannot be a gluon, since a trivial rewriting of momenta in that case will lead back to the FKL ordering.

3.3 Calculations of NLL Partonic Subprocesses

It was discussed in chapter two that the leading amplitudes in the High Energy limit are given by those that involve the maximal number of gluon exchanges in the t -channel by analysis of Regge Theory. To access the sub-leading partonic configurations, we simply replace one gluon propagator by one quark propagator in these FKL amplitudes (whilst keeping the strict rapidity ordering). There are two distinct possibilities we can imagine - we can either replace the first or last propagator in the chain or one in the middle along the chain. We can assign the nomenclature ‘extremal’ and ‘central’ to the two cases respectively. The simplest case of an extremal process is $qg \rightarrow qQ\bar{Q}$ and for the central case it is $qq' \rightarrow qQ\bar{Q}q'$. Once we have expressions for these amplitudes in our language, we can build up all other related amplitudes by once more multiplying in Lipatov vertices and multiplying by ratios of colour factors.

3.3.1 Calculation of $qg \rightarrow qQ\bar{Q}$ in the High Energy Limit

The ultimate aim of this calculation will be to factorise the $qg \rightarrow qQ\bar{Q}$ amplitude into an expression like;

$$M_{qg \rightarrow qQ\bar{Q}} \sim \frac{\langle 1|\mu|a \rangle Q^{\mu\nu}(p_2, p_3, p_b) \varepsilon_\nu(p_b)}{\hat{t}_1}, \quad (3.7)$$

where $Q^{\mu\nu}$ is an effective vertex that encapsulates the effect of the emission of a quark/anti-quark pair at the end of the rapidity chain. We can schematically show this equation as a diagram like in figure 3.2. Given the momentum dependence of the vertex and how it looks schematically, we can also interpret $Q^{\mu\nu}$ as a $g \rightarrow q\bar{q}$ *impact factor*.

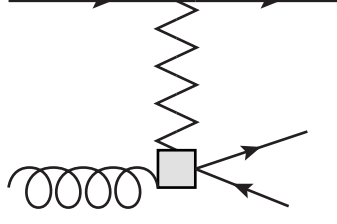


Figure 3.2 Schematic diagram involving $g \rightarrow q\bar{q}$ impact factor.

The technique for this is as follows. We will first study the complete amplitude for $qg \rightarrow qQ\bar{Q}$, for which there are five contributing diagrams as shown in figure 3.3. After we have the full LO expression, we will make some approximations based on the High Energy behaviour of the process to bring the entire amplitude into the desired form. During this approximation stage, we must remember to take care to maintain gauge invariance.

We will begin with the diagram shown in the top left and then proceed from left to right and top to bottom. Using the Feynman rules, we see this contribution is;

$$\begin{aligned}
 iM_1 &= \bar{u}_1(-ig_s\gamma^\nu T_{1q}^g) \frac{i(\not{p}_a + \not{p}_b)}{s_{ab}} (-ig_s\gamma^\mu T_{qa}^b) u_a \varepsilon_\mu(p_b) \frac{-i\eta^{\nu\sigma}}{s_{23}} \langle 2|\sigma|3\rangle (-ig_s T_{23}^g) \\
 &= \frac{ig_s^3 T_{1q}^g T_{qa}^b T_{23}^g}{s_{ab}s_{23}} \left[\bar{u}_1 \gamma^\nu (\not{p}_a + \not{p}_b) \gamma^\mu u_a \right] \langle 2|\nu|3\rangle \varepsilon_\mu(p_b).
 \end{aligned} \tag{3.8}$$

For the diagram involving a u -channel quark propagator, the expression is very similar;

$$iM_2 = \frac{-ig_s^3 T_{1q}^b T_{qa}^g T_{23}^g}{s_{1b}s_{23}} \left[\bar{u}_1 \gamma^\mu (\not{p}_1 - \not{p}_b) \gamma^\nu u_a \right] \langle 2|\nu|3\rangle \varepsilon_\mu(p_b). \tag{3.9}$$

The next diagram involves a three-gluon vertex and by invoking the Feynman

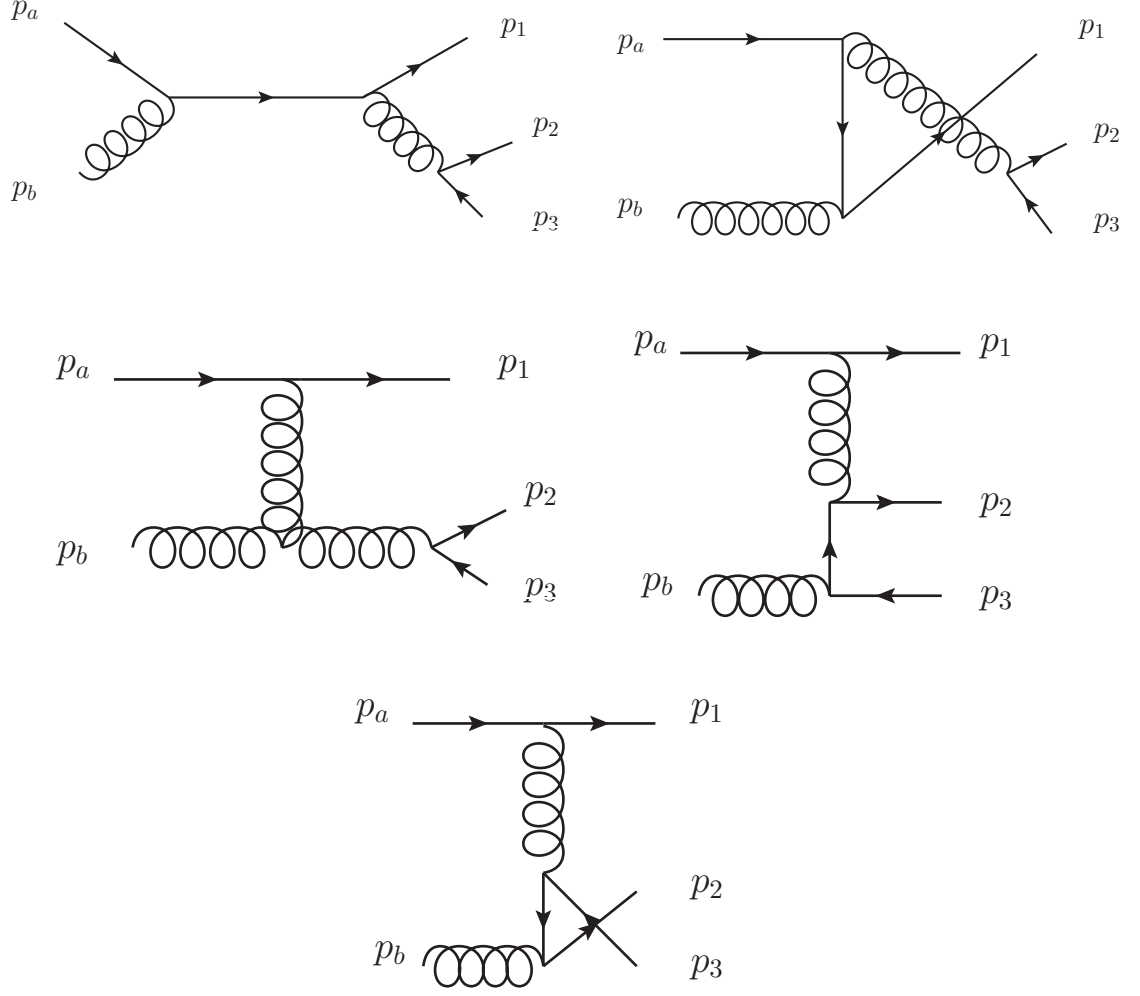


Figure 3.3 All LO graphs for $qq \rightarrow qQ\bar{Q}$.

rules we get;

$$iM_3 = [\bar{u}_1(-ig_s\gamma^\mu T_{1a}^g)u_a] \frac{-i\eta_{\mu\nu}}{\hat{t}_1} \left[\bar{u}_2(-ig_s\gamma^\rho T_{23}^{g'})u_3 \right] \frac{-i\eta_{\beta\rho}}{s_{23}} (-g_s f^{gg'b}) V_{3g}^{\nu\beta\alpha} \varepsilon_\alpha(p_b), \quad (3.10)$$

where;

$$V_{3g}^{\nu\beta\alpha} = (p_a - p_1 + p_2 + p_3)^\alpha \eta^{\nu\beta} - (p_2 + p_3 + p_b)^\nu \eta^{\beta\alpha} + (p_b - p_a + p_1)^\beta \eta^{\alpha\nu}. \quad (3.11)$$

Algebraic manipulation of this expression leads to;

$$iM_3 = \frac{-g_s^3 T_{1a}^g T_{23}^{g'} f^{gg'b}}{t_1 s_{23}} \langle 1|\nu|a\rangle \langle 2|\beta|3\rangle V_{3g}^{\nu\beta\alpha} \epsilon_\alpha(p_b). \quad (3.12)$$

Finally, we have the last two diagrams that involve both a t -channel gluon and quark propagator. For the first, we have:

$$iM_4 = [\bar{u}_1(-ig_s\gamma^\mu T_{1a}^g)u_a] \frac{-i\eta_{\mu\nu}}{\hat{t}_1} \left[\bar{u}_2(-ig_s\gamma^\nu T_{2q}^g) \frac{-i(\not{p}_3 - \not{p}_b)}{\hat{t}_2} (-ig_s\gamma^\rho T_{q3}^b)u_3 \right] \varepsilon_\rho(p_b). \quad (3.13)$$

Note the minus sign in the propagator; this is because the Feynman rule for the quark propagator requires that the momentum flows in the same direction as the charge. This can be written:

$$iM_4 = \frac{-ig_s^3 T_{1a}^g T_{q3}^b T_{2q}^g}{\hat{t}_1 \hat{t}_2} \langle 1|\nu|a\rangle \left[\bar{u}_2\gamma^\nu(\not{p}_3 - \not{p}_b)\gamma^\rho u_3 \right] \varepsilon_\rho(p_b). \quad (3.14)$$

A similar analysis yields for the last diagram (no minus sign from the fermion propagator this time);

$$iM_5 = \frac{ig_s^3 T_{1a}^g T_{2q}^b T_{q3}^g}{\hat{t}_1 \tilde{t}_2} \langle 1|\nu|a\rangle \left[\bar{u}_2\gamma^\rho(\not{p}_2 - \not{p}_b)\gamma^\nu u_3 \right] \varepsilon_\rho(p_b), \quad (3.15)$$

with $\tilde{t}_2 = (p_2 - p_b)^2$. We now have expressions that, when summed, will give the exact, LO result for the process $qg \rightarrow qQ\bar{Q}$. Now we must approximate in order to factorise the t -channel pole. No approximation is required for M_3, M_4 or M_5 since the t -channel pole is immediately explicit. M_1 and M_2 , however, need special attention. The problematic part is the square brackets of, for example, M_1 which we can rewrite using the completeness relation;

$$\bar{u}_1\gamma^\nu(\not{p}_a + \not{p}_b)\gamma^\mu u_a = \langle 1|\nu|a\rangle 2p_a^\mu + \langle 1|\nu|b\rangle \langle b|\mu|a\rangle, \quad (3.16)$$

where the spinor brackets have no helicity index written to indicate that the expansion is valid for both negative and positive helicities. The ν index is contracted with the quark current $\langle 2|\nu|b\rangle$. Depending on the helicity choices, the

second term after contraction behaves either like $\sqrt{s_{b3}s_{12}}$ or $\sqrt{s_{13}s_{b2}}$. Similarly, the first term behaves either like $\sqrt{s_{a3}s_{12}}$ or $\sqrt{s_{13}s_{a2}}$. The relative size of these terms is then $\sqrt{s_{b3}/s_{a3}}$ or $\sqrt{s_{b2}/s_{a2}}$. In the High Energy limit, it is clear that both s_{a3} and s_{a2} both are large. Also, since we are dealing with the case where the $q\bar{q}$ pair is emitted close in rapidity to one end of the chain, we can reasonably assume that s_{b3} and s_{b2} do not have to be large. We can therefore drop the second term with respect to the first and thus;

$$iM_1 \approx \frac{ig_s^3 T_{1q}^g T_{qa}^b T_{23}^g}{s_{ab}s_{23}} [2p_a^\mu \langle 1|\nu|a\rangle] \langle 2|\nu|3\rangle \varepsilon_\mu(p_b). \quad (3.17)$$

A similar argument holds for M_2 and so;

$$iM_2 \approx \frac{-ig_s^3 T_{1q}^b T_{qa}^g T_{23}^g}{s_{1b}s_{23}} [2p_1^\mu \langle 1|\nu|a\rangle] \langle 2|\nu|3\rangle \varepsilon_\mu(p_b). \quad (3.18)$$

We can now take the limit that $p_a \sim p_1$, which allows us to combine these two diagrams by using the colour commutator result:

$$(T_{1q}^g T_{qa}^b - T_{1q}^b T_{qa}^g) T_{23}^g = if^{gbc} T_{1a}^c T_{23}^g. \quad (3.19)$$

This is the same colour factor as that of the diagram involving a t -channel gluon exchange under the relabelling $g \rightarrow c$ and $g' \rightarrow g$. Because of this, we will from now on call the result of this iC_t . Thus;

$$i(M_1 + M_2) \rightarrow \frac{-g_s^3 C_t}{s_{ab}s_{23}} 2p_a^\mu \langle 1|\nu|a\rangle \langle 2|\nu|3\rangle \varepsilon_\mu(p_b), \quad (3.20)$$

and so we have now factored out the quark current in all the amplitudes. If we now combine all the amplitudes together, then we get the form of $Q^{\mu\nu}$ to be:

$$Q^{\mu\nu} = -\frac{C_1}{\hat{t}_2} \left(\bar{u}_2 \gamma^\mu (\not{p}_3 - \not{p}_b) \gamma^\nu u_3 \right) + \frac{C_2}{\hat{t}_2} \left(\bar{u}_2 \gamma^\nu (\not{p}_2 - \not{p}_b) \gamma^\mu u_3 \right) + i \frac{C_t}{s_{23}} \left(\frac{2p_a^\nu \hat{t}_1}{s_{ab}} \langle 2|\mu|3\rangle + V_{3g}^{\mu\rho\nu} \langle 2|\rho|3\rangle \right), \quad (3.21)$$

where we have relabelled some Lorentz indices to conform with equation 3.7 and

where;

$$C_1 = T_{1a}^g T_{q3}^b T_{2q}^g, \quad (3.22a)$$

$$C_2 = T_{1a}^g T_{2q}^b T_{q3}^g, \quad (3.22b)$$

$$C_t = f^{gbc} T_{1a}^c T_{23}^g. \quad (3.22c)$$

We should check at this point that our expression is indeed still gauge invariant after having made these approximations. The simplest way to check is to make use of the Ward Identity, which implies $Q^{\mu\nu} p_{b,\nu} = 0$. Explicitly;

$$\begin{aligned} Q^{\mu\nu} p_{b,\nu} &= -\frac{C_1}{\hat{t}_2} \left(\bar{u}_2 \gamma^\mu \not{p}_3 \not{p}_b u_3 \right) + \frac{C_2}{\tilde{t}_2} \left(\bar{u}_2 \not{p}_b \not{p}_2 \gamma^\mu u_3 \right) + i \frac{C_t}{s_{23}} \left(\hat{t}_1 \langle 2|\mu|3 \rangle + V_{3g}^{\mu\rho\nu} p_{b\nu} \langle 2|\rho|3 \rangle \right) \\ &= -\frac{C_1}{\hat{t}_2} s_{3b} \langle 2|\mu|3 \rangle + \frac{C_2}{\tilde{t}_2} s_{2b} \langle 2|\mu|3 \rangle + i \frac{C_t}{s_{23}} \left(\hat{t}_1 \langle 2|\mu|3 \rangle + (s_{2b} + s_{3b}) \langle 2|\mu|3 \rangle - \right. \\ &\quad \left. (p_2 + p_3 + p_b)^\mu p_b^\rho \langle 2|\rho|3 \rangle + 2p_b^\mu p_b^\rho \langle 2|\rho|3 \rangle \right) \\ &= \frac{\langle 2|\mu|3 \rangle}{s_{23}} (C_1 s_{23} - C_2 s_{23} + i C_t (\hat{t}_1 + (s_{2b} + s_{3b}))) \\ &\quad + i \langle 2|\rho|3 \rangle \frac{C_t}{s_{23}} (-(p_2 + p_3 + p_b)^\mu p_b^\rho + 2p_b^\mu p_b^\rho) \\ &= i C_t \frac{\langle 2|\mu|3 \rangle}{s_{23}} (-s_{23} + (-s_{2b} - s_{3b} + s_{23} + s_{2b} + s_{3b})) \\ &\quad + i \langle 2|\rho|3 \rangle \frac{C_t}{s_{23}} (-(p_2 + p_3 + p_b)^\mu p_b^\rho + 2p_b^\mu p_b^\rho) \\ &\approx i C_t \frac{\langle 2|\rho|3 \rangle}{s_{23}} (-2p_b^\mu p_b^\rho + 2p_b^\mu p_b^\rho) \\ &= 0, \end{aligned} \quad (3.23)$$

where we have had to make the high energy approximation $p_b \sim p_2 + p_3$. Therefore, so long as we always approximate the three gluon vertex in this manner (this is where the ‘offending’ term came from), the effective vertex is, indeed, a gauge invariant quantity. It may seem, however, that the effective vertex is not truly factorised since there is a clear instance of p_a in the vertex. Because the complete term goes like p_a^μ / s_{ab} , it is actually independent of p_a ¹. We still have freedom to

¹An easy way to convince oneself of this is to work in light-cone co-ordinates and see that the p_a^+ scale factors out on the top and bottom of the expression.

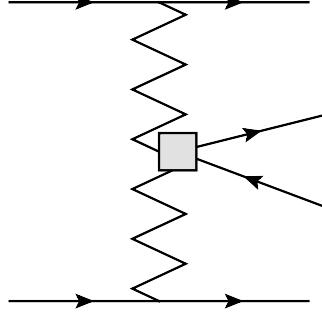


Figure 3.4 *Effective description of $qQ \rightarrow qq'\bar{q}'Q$*

make a gauge choice to do our calculations in, however, and a good choice will be the gauge where the gluon polarisation vector is orthogonal to p_a and we have;

$$\begin{aligned}
Q_{gauge}^{\mu\nu} = & -\frac{C_1}{\hat{t}_2} \left(\bar{u}_2 \gamma^\mu (\not{p}_3 - \not{p}_b) \gamma^\nu u_3 \right) + \frac{C_2}{\hat{t}_2} \left(\bar{u}_2 \gamma^\nu (\not{p}_2 - \not{p}_b) \gamma^\mu u_3 \right) \\
& + i \frac{C_t}{s_{23}} \left((2p_2 + 2p_3)^\nu \eta^{\mu\rho} - 2p_b^\mu \eta^{\nu\rho} + 2p_b^\rho \eta^{\nu\mu} \right) \langle 2|\rho|3 \rangle,
\end{aligned} \tag{3.24}$$

completing our calculation for the basis HEJ amplitude in the case of an extremal $q\bar{q}$ process.

3.3.2 Calculation of $qq' \rightarrow qQ\bar{Q}q'$ in the High Energy Limit

The technique for calculating the amplitude for the central process is precisely the same as the one for the extremal process. In this case, we are searching for an amplitude of the form;

$$M_{qq' \rightarrow qQ\bar{Q}q'} \sim \frac{\langle 1|\mu|a \rangle X^{\mu\nu} \langle 4|\nu|b \rangle}{\hat{t}_1 \hat{t}_3}. \tag{3.25}$$

There are a total of 7 diagrams to calculate here, shown in figure 3.5. Once more, we will calculate the diagrams starting with the one in the top left and proceeding

left to right. The expression for the first diagram is;

$$iM_1 = \frac{-ig_s^4 T_{1q}^e T_{qa}^g T_{23}^e T_{4b}^g}{s_{23} \hat{t}_3} \left[\bar{u}_1 \gamma^\mu \frac{(\not{p}_1 + \not{p}_2 + \not{p}_3)}{(p_1 + p_2 + p_3)^2} \gamma^\rho u_a \right] [\bar{u}_2 \gamma_\mu u_3] [\bar{u}_4 \gamma_\rho u_b]. \quad (3.26)$$

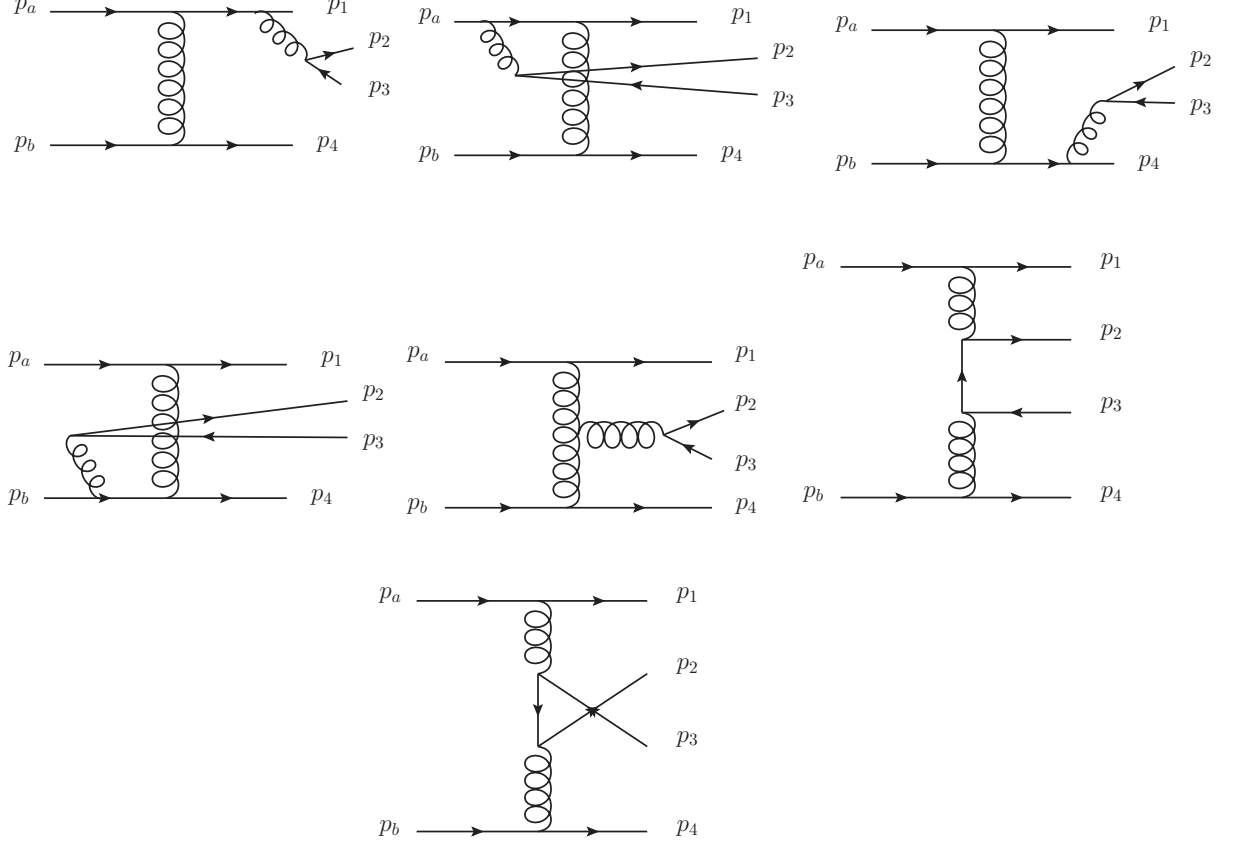


Figure 3.5 All LO graphs for $qq' \rightarrow qQ\bar{Q}q'$.

It is immediately clear that this diagram will not factorise into our desired form, so we expand the square bracket as a spinor chain again to attempt to make some approximations;

$$\frac{1}{s_{12} + s_{13} + s_{23}} (\langle 1|\mu|1\rangle \langle 1|\rho|a\rangle + \langle 1|\mu|2\rangle \langle 2|\rho|a\rangle + \langle 1|\mu|3\rangle \langle 3|\rho|a\rangle). \quad (3.27)$$

Depending on the helicities, either the second or third term in this bracket is

identically zero when contracted with the quark current $\langle 2|\mu|3\rangle$. Once more, we can use a scaling argument to eliminate other terms in this string. The first term contracted with $\langle 2|\mu|3\rangle$ will scale as $\sqrt{s_{12}s_{13}}$ regardless of helicity choices. For the other non-zero term, the scaling will be like $\sqrt{s_{23}s_{12}}$. We have no requirement that s_{23} be large but all other invariants there are large and thus we can approximate the sub-amplitude by keeping the first term only;

$$iM_1 \approx \frac{-ig_s^4 T_{1q}^e T_{qa}^g T_{23}^e T_{4b}^g}{s_{23} \hat{t}_3 (s_{12} + s_{13})} \langle 1|\rho|a\rangle \langle 4|\rho|b\rangle \times 2p_1^\mu \langle 2|\mu|3\rangle. \quad (3.28)$$

The next graph is very similar to the previous and so the calculation proceeds in the same fashion as before. We will then skip to the final expression (having again made the approximation) which is;

$$iM_2 \approx \frac{ig_s^4 T_{1q}^g T_{qa}^e T_{23}^e T_{4b}^g}{s_{23} \hat{t}_3 (s_{a2} + s_{a3})} \langle 1|\rho|a\rangle \langle 4|\rho|b\rangle \times 2p_a^\mu \langle 2|\mu|3\rangle. \quad (3.29)$$

The next two graphs where the $q\bar{q}$ is emitted from the p_4 and p_b legs is clearly very similar to the previous two results. Because of this, we simply state the result of the calculation here for these amplitudes which for the p_4 leg is;

$$iM_3 \approx \frac{-ig_s^4 T_{1a}^g T_{4q}^e T_{qb}^g T_{23}^e}{\hat{t}_1 s_{23} (s_{24} + s_{34})} \langle 1|\rho|a\rangle \langle 4|\rho|b\rangle \times 2p_4^\mu \langle 2|\mu|3\rangle, \quad (3.30)$$

and for the p_b leg is;

$$iM_4 \approx \frac{ig_s^4 T_{1a}^g T_{4q}^g T_{qb}^e T_{23}^e}{\hat{t}_1 s_{23} (s_{2b} + s_{3b})} \langle 1|\rho|a\rangle \langle 4|\rho|b\rangle \times 2p_b^\mu \langle 2|\mu|3\rangle. \quad (3.31)$$

The remaining graphs are already t -channel factorised and so we know that we can include them exactly. The next diagram where the $q\bar{q}$ emission is off of the t -channel gluon propagator has the exact expression;

$$iM_5 = \frac{g_s^4 T_{1a}^g f^{geg'} T_{4b}^{g'} T_{23}^e}{\hat{t}_1 s_{23} \hat{t}_3} \left((q_1 + p_2 + p_3)^\lambda \eta^{\nu\sigma} + (q_3 - p_2 - p_3)^\nu \eta^{\sigma\lambda} - (q_1 + q_3)^\sigma \eta^{\nu\lambda} \right) \\ [\bar{u}_1 \gamma_\nu u_a] [\bar{u}_4 \gamma_\lambda u_b] [\bar{u}_2 \gamma_\sigma u_3]. \quad (3.32)$$

The final two diagrams both have quark propagators. They have the exact expressions;

$$iM_6 = \frac{ig_s^4 T_{1a}^g T_{2q}^g T_{q3}^{g'} T_{4b}^{g'}}{\hat{t}_1 \hat{t}_2 \hat{t}_3} [\bar{u}_1 \gamma^\mu u_a] [\bar{u}_4 \gamma^\sigma u_b] \left[\bar{u}_2 \gamma_\mu (\not{p}_a - \not{p}_1 - \not{p}_2) \gamma_\sigma u_3 \right], \quad (3.33)$$

and;

$$iM_7 = \frac{-ig_s^4 T_{1a}^g T_{2q}^{g'} T_{q3}^g T_{4b}^{g'}}{\hat{t}_1 \hat{t}_2 \hat{t}_3} [\bar{u}_1 \gamma^\mu u_a] [\bar{u}_4 \gamma^\sigma u_b] \left[\bar{u}_2 \gamma_\sigma (\not{p}_a - \not{p}_1 - \not{p}_3) \gamma_\mu u_3 \right], \quad (3.34)$$

respectively, where $\tilde{t}_2 = (p_a - p_1 - p_3)^2$.

Since the High Energy limit here still implies $p_a \sim p_1$ and $p_b \sim p_4$, we can approximately combine both M_1 with M_2 and M_3 with M_4 . Doing the former yields;

$$i(M_1 + M_2) \approx \frac{C_1 g_s^4}{s_{23} \hat{t}_3 (s_{a2} + s_{a3})} \langle 1|\rho|a \rangle \langle 4|\rho|b \rangle \times 2p_a^\sigma \langle 2|\sigma|3 \rangle, \quad (3.35)$$

where we have defined:

$$C_1 = T_{1q}^e T_{qa}^g T_{23}^e T_{4b}^g - T_{1q}^g T_{qa}^e T_{23}^e T_{4b}^g = f^{egc} T_{1a}^c T_{23}^e T_{4b}^g, \quad (3.36)$$

and a similar process on M_3 and M_4 grants;

$$i(M_3 + M_4) \rightarrow \frac{-C_1 g_s^4}{s_{23} \hat{t}_1 (s_{b2} + s_{b3})} \langle 1|\rho|a \rangle \langle 4|\rho|b \rangle \times 2p_b^\sigma \langle 2|\sigma|3 \rangle. \quad (3.37)$$

We are then in a position to combine all graphs together and derive our effective

vertex $X^{\mu\nu}$;

$$X^{\mu\nu} = \frac{C_1}{s_{23}} \left(\eta^{\mu\nu} \left(2p_a^\sigma \left(\frac{q_1^2}{s_{a2} + s_{a3}} \right) - 2p_b^\sigma \left(\frac{q_3^2}{s_{b2} + s_{b3}} \right) \right) + V_{3g}^{\mu\nu\sigma} \right) \langle 2|\sigma|3 \rangle \\ + \frac{iC_2}{\hat{t}_2} X_{qprop}^{\mu\nu} - \frac{iC_3}{\tilde{t}_2} X_{crossed}^{\mu\nu}, \quad (3.38)$$

where we have defined the following expressions:

$$V_{3g}^{\mu\nu\sigma} = (q_1 + p_2 + p_3)^\nu \eta^{\mu\sigma} + (q_3 - p_2 - p_3)^\mu \eta^{\sigma\nu} - (q_1 + q_3)^\sigma \eta^{\mu\nu} \quad (3.39a)$$

$$C_2 = T_{1a}^g T_{2q}^g T_{q3}^{g'} T_{4b}^{g'} \quad (3.39b)$$

$$C_3 = T_{1a}^g T_{2q}^{g'} T_{q3}^g T_{4b}^{g'} \quad (3.39c)$$

$$X_{qprop}^{\mu\nu} = \bar{u}_2 \gamma^\mu (\not{q}_1 - \not{p}_2) \gamma^\nu u_3 \quad (3.39d)$$

$$X_{crossed}^{\mu\nu} = \bar{u}_2 \gamma^\nu (\not{q}_1 - \not{p}_3) \gamma^\mu u_3. \quad (3.39e)$$

In fact, since we assumed $p_a \sim p_1$ and $p_b \sim p_4$ in deriving this form, we can go one step further and reinstate this symmetry so that our final vertex looks like:

$$X^{\mu\nu} = \frac{C_1}{s_{23}} \left(\eta^{\mu\nu} X_{sym}^\sigma + V_{3g}^{\mu\nu\sigma} \right) \langle 2|\sigma|3 \rangle \\ + \frac{iC_2}{\hat{t}_2} X_{qprop}^{\mu\nu} - \frac{iC_3}{\tilde{t}_2} X_{crossed}^{\mu\nu}, \quad (3.40)$$

with:

$$X_{sym}^\sigma = p_a^\sigma \left(\frac{q_1^2}{s_{a2} + s_{a3}} \right) + p_1^\sigma \left(\frac{q_1^2}{s_{12} + s_{13}} \right) \\ - p_b^\sigma \left(\frac{q_3^2}{s_{b2} + s_{b3}} \right) - p_4^\sigma \left(\frac{q_3^2}{s_{42} + s_{43}} \right). \quad (3.41)$$

We have intentionally used the notation of q^2 rather than \hat{t} to make it clear that this invariant is the invariant formed from the mass of the propagator entering into the effective vertex. Once extra emissions are added, the \hat{t} notation can be

misleading. With this, we now have the complete expression for the effective central $q\bar{q}$ vertex.

3.3.3 Checks and Verifications of Amplitudes

In order to check the derivation of these amplitudes, we will explicitly investigate how they behave in the MRK limit. We discussed before that we expect them to be suppressed by the invariant $s_{q\bar{q}}$ with respect to the leading FKL configurations at the $|M|^2$ level. Since the FKL amplitudes behaved as \hat{s}^2 at the $|M|^2$ level, we should see a systematic dying off of these new amplitudes if we plot $|M|^2/\hat{s}^2$ and furthermore multiplication of $s_{q\bar{q}}$ should combat this suppression. In these amplitudes, we have a more complicated colour structure than we did before, with each effective vertex depending on three. At the $|M|^2$ level, we must ensure to deal with this correctly when performing the colour sum. This is done by splitting up the vertices into sub-vertices, each one of which being associated with one colour factor. For example;

$$Q^{\mu\nu} = C_1 Q_1^{\mu\nu} + C_2 Q_2^{\mu\nu} + C_t Q_t^{\mu\nu}, \quad (3.42)$$

which will allows us to calculate the squared amplitude as (the colour sum is implicitly performed);

$$\begin{aligned} |M_{qg \rightarrow qQ\bar{Q}}|^2 \sim \frac{1}{24} & \left(|C_1 M_{Q_1}|^2 + |C_2 M_{Q_2}|^2 + |C_t M_{Q_t}|^2 \right. \\ & \left. + 2Re(C_1 C_2^\dagger M_{Q_1} M_{Q_2}^\dagger) + 2Re(C_1 C_t^\dagger M_{Q_1} M_{Q_t}^\dagger) + 2Re(C_2 C_t^\dagger M_{Q_2} M_{Q_t}^\dagger) \right), \end{aligned} \quad (3.43)$$

where the pre-factor comes from the colour averaging factor. We can calculate the $qq' \rightarrow qQ\bar{Q}q'$ amplitude in a similar manner. The helicity sum is performed explicitly and the average brings about a further factor of 1/4 in both cases. In order to check how our matrix element performs against the full leading order result, we plot the value of $|M|^2/\hat{s}^2$ for both approaches (the latter taken from MadGraph) across a slice of phase space. For the $qg \rightarrow qQ\bar{Q}$ amplitude, the

momenta are chosen such that;

$$\begin{aligned} p_1 &= (40 \cosh(\Delta), 0, 40, 40 \sinh(\Delta)), \\ p_2 &= (40\sqrt{2}, 40, -40, 0), \\ p_3 &= (40 \cosh(-\Delta), -40, 0, 40 \sinh(-\Delta)), \end{aligned} \tag{3.44}$$

and the results are plotted in figure 3.6. We see that the two calculations follow each other very closely and we also see the suppression at large Δ as we expected. In figure 3.7, we multiply this result by $s_{q\bar{q}}$ and show that it is indeed this invariant that is suppressing the amplitude in this regime.

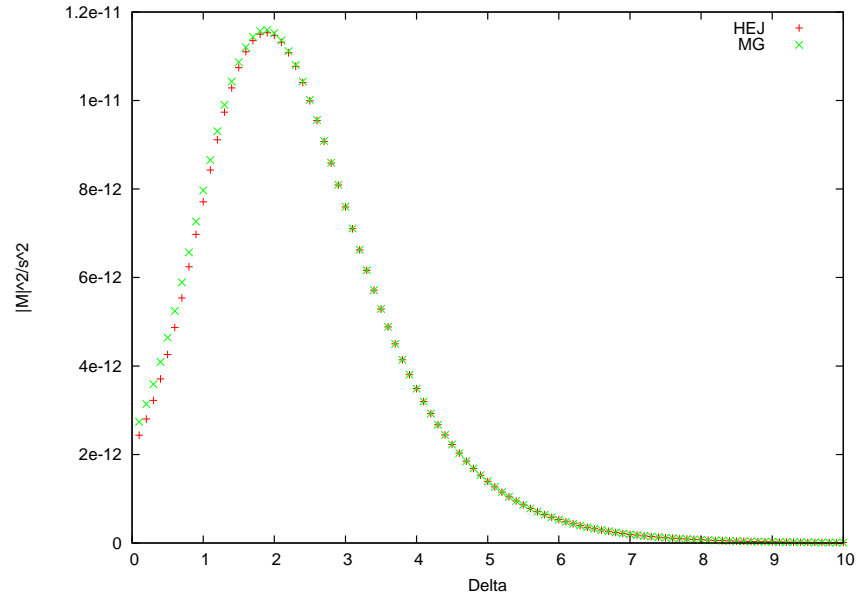


Figure 3.6 *Effective vertex approach to the $qg \rightarrow qQ\bar{Q}$ amplitude (red) compared to the full LO (green).*

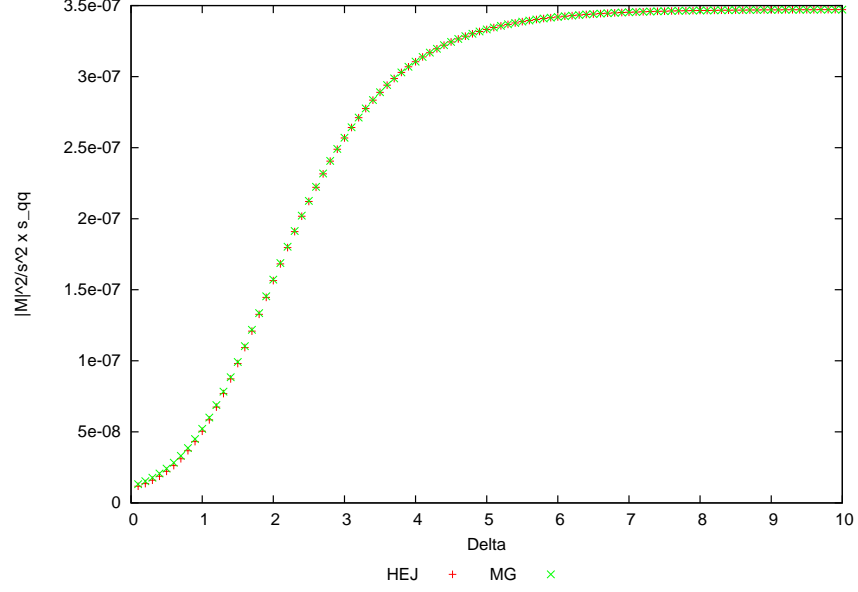


Figure 3.7 *Effective vertex approach to the $qg \rightarrow qQ\bar{Q}$ amplitude (red) compared to the full LO (green) multiplied by the invariant mass of the quark/anti-quark pair.*

We can perform a similar test on the $qq' \rightarrow qQ\bar{Q}q'$ amplitude, where we choose the momenta to be;

$$\begin{aligned}
 p_1 &= (40 \cosh(\Delta), 0, 40, 40 \sinh(\Delta)), \\
 p_2 &= (40 \cosh(\Delta/3), 40, 0, 40 \sinh(\Delta/3)), \\
 p_3 &= (40 \cosh(-\Delta/3), 0, -40, 40 \sinh(-\Delta/3)), \\
 p_4 &= (40 \cosh(-\Delta), -40, 0, 40 \sinh(-\Delta)).
 \end{aligned} \tag{3.45}$$

The comparison between our amplitude and the full leading order is shown in figure 3.8. We see once more the good agreement between the two across the phase space as well as suppression at large Δ , which figure 3.9 shows is due to $s_{q\bar{q}}$.

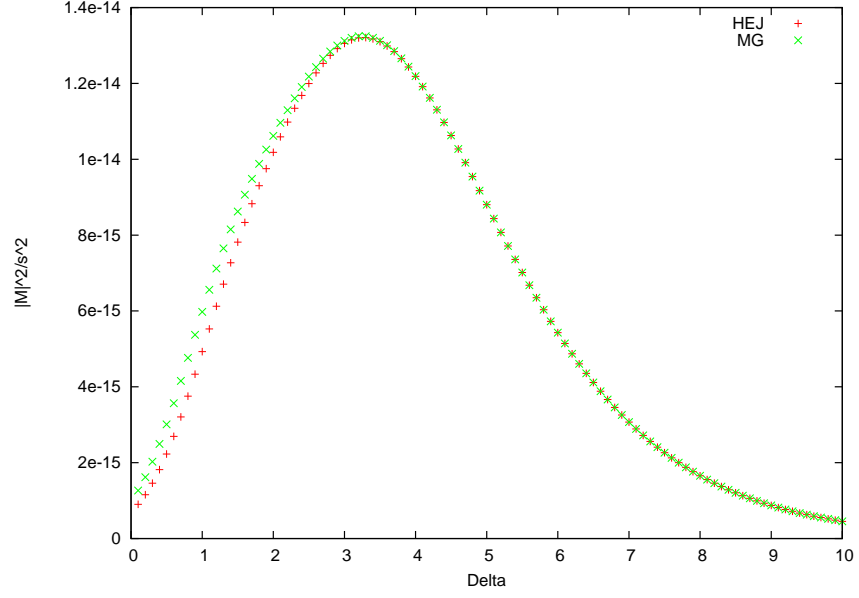


Figure 3.8 *Effective vertex approach to the $qq' \rightarrow qQ\bar{Q}q'$ amplitude (red) compared to the full LO (green).*

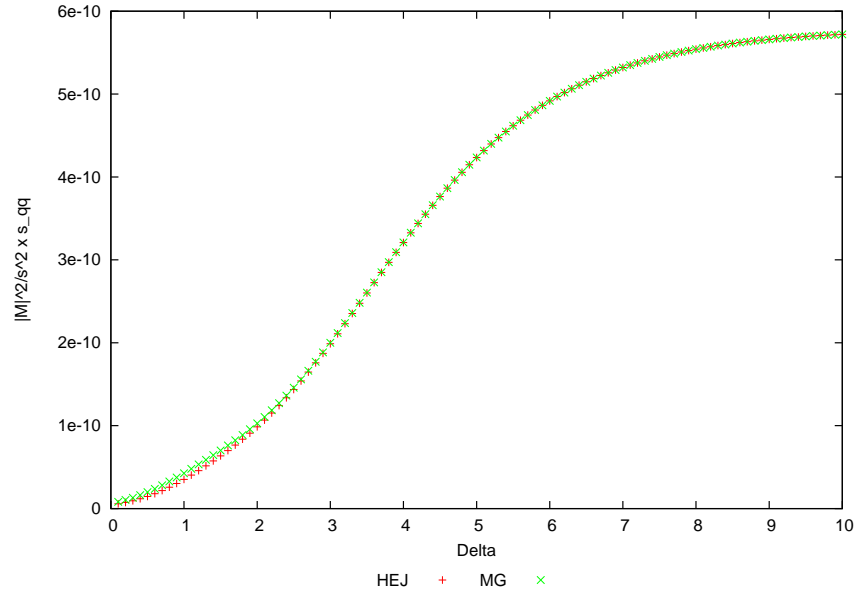


Figure 3.9 *Effective vertex approach to the $qq' \rightarrow qQ\bar{Q}q'$ amplitude (red) compared to the full LO (green) multiplied by the invariant mass of the quark/anti-quark pair.*

Given these tests, we are satisfied that these ‘base’ amplitudes work as expected. To extend them, we need to be able to generalise them to an arbitrary incoming state and we need to describe the effect of extra gluon emissions. The first of these, we postulated, can be achieved by a simple multiplication of a colour factor at the $|M|^2$ level and, since this was based on the high energy behaviour of amplitudes, the same idea still applies here. However, for the $qg \rightarrow qQ\bar{Q}$ case, we must always require that there is a gluon in the initial state since our vertex is an impact factor for the splitting of a gluon into a quark/anti-quark pair. Therefore, the only extension we need to consider (anti-quarks in the initial state require no alteration) is the replacement of the quark in the initial state with a gluon. Our postulate is that;

$$|M_{gg \rightarrow gQ\bar{Q}}|^2 \sim \frac{\tilde{C}_A}{C_F} |M_{qg \rightarrow qQ\bar{Q}}|^2, \quad (3.46)$$

and we plot this result (multiplied by $s_{q\bar{q}}$) along with the full leading order in figure 3.10. The difference between the two lines is minimal and only in the low Δ regime where it should be expected to be different. We conclude that this method of replacing incoming partons does indeed still hold. For completeness, we also check the $qq' \rightarrow qQ\bar{Q}q'$ amplitude, where we can have both qg and gg initial states;

$$\begin{aligned} |M_{qg \rightarrow qQ\bar{Q}g}|^2 &\sim \frac{\tilde{C}_A}{C_F} |M_{qq' \rightarrow qQ\bar{Q}q'}|^2, \\ |M_{gg \rightarrow gQ\bar{Q}g}|^2 &\sim \left(\frac{\tilde{C}_A}{C_F} \right)^2 |M_{qq' \rightarrow qQ\bar{Q}q'}|^2. \end{aligned} \quad (3.47)$$

The comparison to the full leading order of these amplitudes (multiplied by $s_{q\bar{q}}$) is shown in figures 3.11 and 3.12 respectively.

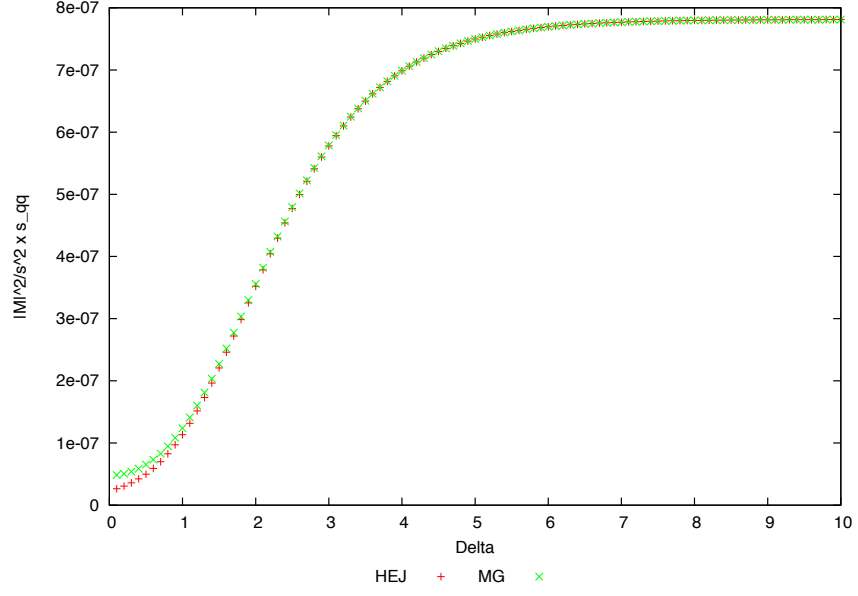


Figure 3.10 *Effective vertex approach to the $gg \rightarrow gQ\bar{Q}$ amplitude (red) compared to the full LO (green) multiplied by the invariant mass of the quark/anti-quark pair.*

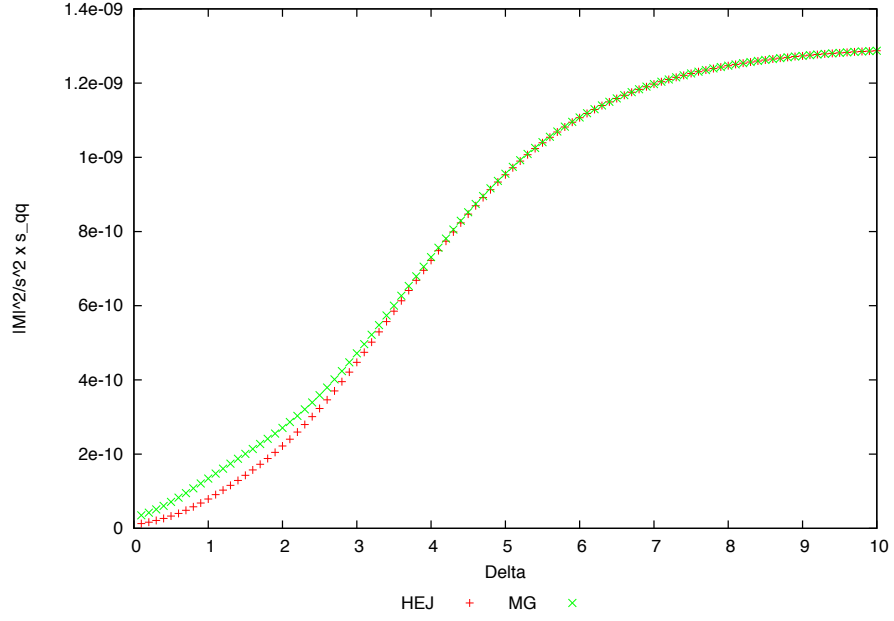


Figure 3.11 *Effective vertex approach to the $qg \rightarrow qQ\bar{Q}g$ amplitude (red) compared to the full LO (green) multiplied by the invariant mass of the quark/anti-quark pair.*

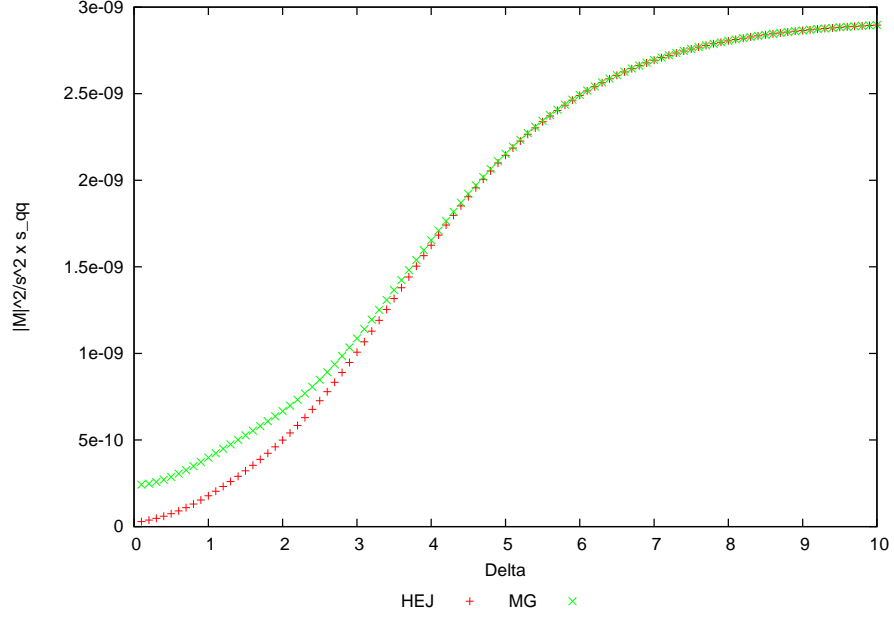


Figure 3.12 *Effective vertex approach to the $gg \rightarrow gQ\bar{Q}g$ amplitude (red) compared to the full LO (green) multiplied by the invariant mass of the quark/anti-quark pair.*

Again, we conclude that the colour factor multiplication is sufficient to approximate the full leading order result. We therefore move on to discussing how extra gluon emissions are added to these amplitudes. Because of the factorisation properties of the High Energy Limit, so long as we assume the extra gluon emissions are far away in rapidity from the partons already in the amplitude, we can simply multiply in a Lipatov vertex, along with a colour factor and then dividing by additional t -channel poles that will appear. For the $qg \rightarrow qQ\bar{Q}$ case, this yields simply;

$$|M_{qg \rightarrow q \dots Q\bar{Q}}|^2 \sim |M_{qg \rightarrow qQ\bar{Q}}|^2 \times \prod_{i=1}^{n-3} C_A \left(\frac{-V(q_i, q_{i+1}) \cdot V(q_i, q_{i+1})}{q_i^2} \right), \quad (3.48)$$

where the set of dots represents the emission of $n - 3$ gluons, with n being the total number of final state partons. For the $qq' \rightarrow qQ\bar{Q}q'$ amplitude, we can either have the gluon emitted in rapidity between the most forward parton and

the quark/anti-quark pair or between the pair and the most backward parton;

$$|M_{qq' \rightarrow q \dots Q \bar{Q} \dots q'}|^2 = |M_{qq' \rightarrow q Q \bar{Q} q'}|^2 \times \prod_{i=1}^{n_a} C_A \left(\frac{-V(q_i, q_{i+1}) \cdot V(q_i, q_{i+1})}{q_{i+1}^2} \right) \times \prod_{j=n_a+2}^{n-2} C_A \left(\frac{-V(q_j, q_{j+1}) \cdot V(q_j, q_{j+1})}{q_j^2} \right), \quad (3.49)$$

where n_a is the number of gluons more forward in rapidity than the quark/anti-quark pair. We take the simple case of emitting one extra gluon and again compare to the full leading order result to check that the argument we employ holds. In figure 3.13 we plot our effective description for the $qg \rightarrow qgQ\bar{Q}$ amplitude with an extra gluon emission and compare with the leading order result. The momenta we use are the same as the momenta in equation 3.45.

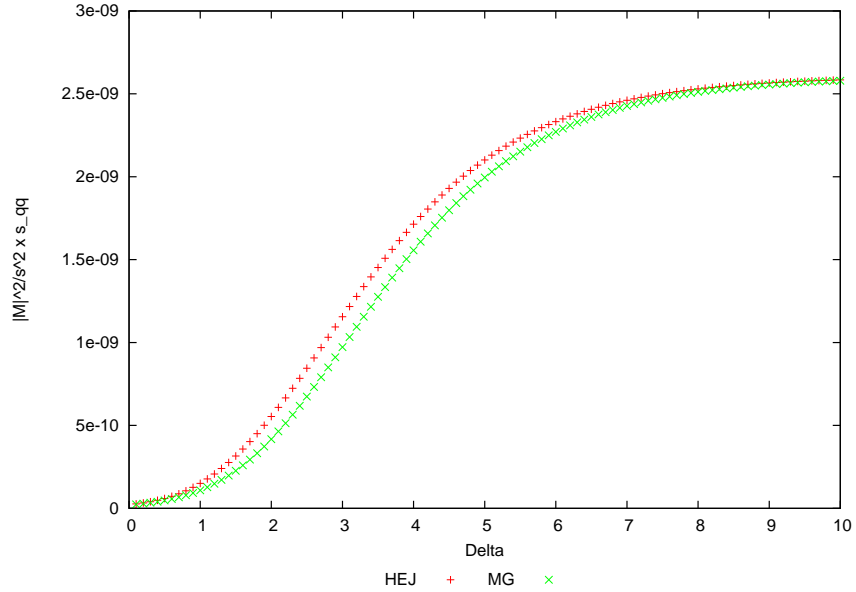


Figure 3.13 *Effective vertex approach to the $qg \rightarrow qgQ\bar{Q}$ amplitude (red) compared to the full LO (green) multiplied by the invariant mass of the quark/anti-quark pair.*

For the case of the central $q\bar{q}$ emission plus an extra gluon emission, we employ the

following set of five jet momenta;

$$\begin{aligned}
p_1 &= (40 \cosh(\Delta), 0, 40, 40 \sinh(\Delta)), \\
p_2 &= (40 \cosh(\Delta/2), -40, 0, 40 \sinh(\Delta/2)), \\
p_3 &= (80\sqrt{2}, 80, -80, 0), \\
p_4 &= (40 \cosh(-\Delta/2), -40, 0, 40 \sinh(-\Delta/2)), \\
p_5 &= (40 \cosh(-\Delta), 0, 40, 40 \sinh(-\Delta)).
\end{aligned} \tag{3.50}$$

In figure 3.14 we plot the result for when the gluon is more forward in rapidity than the $q\bar{q}$ pair and in 3.14 we have the result for when it is emitted more backward in rapidity. All three of these latest figures show the reasonable agreement with the full result.

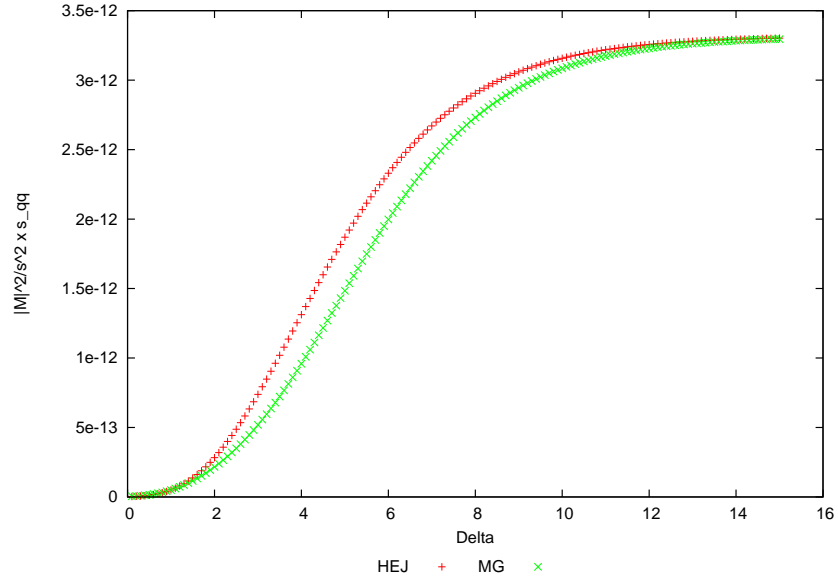


Figure 3.14 *Effective vertex approach to the $qq' \rightarrow qqQ\bar{Q}q'$ amplitude (red) compared to the full LO (green) multiplied by the invariant mass of the quark/anti-quark pair.*

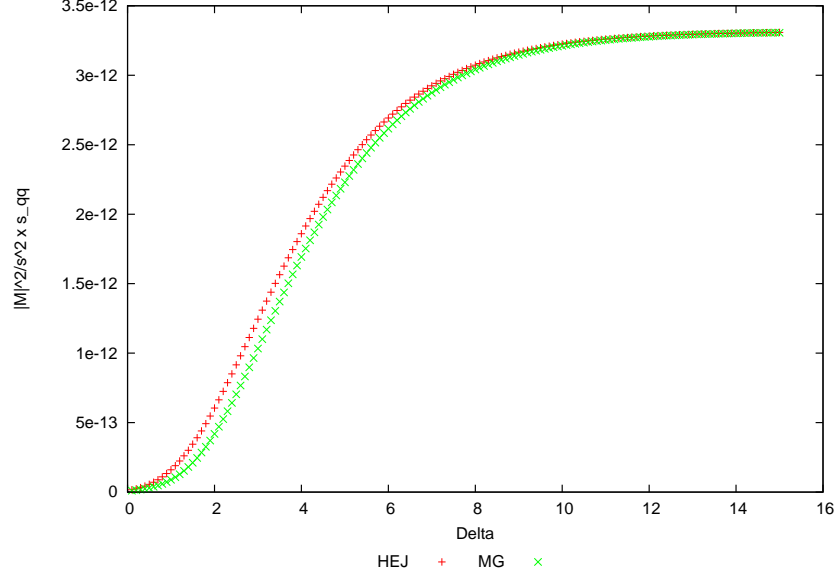


Figure 3.15 *Effective vertex approach to the $qq' \rightarrow qQ\bar{Q}qq'$ amplitude (red) compared to the full LO (green) multiplied by the invariant mass of the quark/anti-quark pair.*

3.4 Computational Aspects

The plots of the last section all served to convince that the derived amplitudes behaved as expected. The next step is to include them in the full HEJ program correctly. This is a very significant change to the codebase that requires the modification of many files and so a ‘branch’ of the code base was created so that all work can be done independent of other projects going on in the collaboration. Once everything is done and checked, the branch can be ‘merged’ back into the main development code base in a way that does not disrupt any other work done there since the branch was created. The points that need to be considered when adding these amplitudes in are as follows;

1. Correctly removing calls to fixed order non-FKL processes if they are now to be included in the resummation. For example, the code already contains a call to the $qg \rightarrow qQ\bar{Q}$ amplitude at leading order for matching purposes. We therefore need to remove calls to these particular subprocesses in that section of the code and we need to remove them only if the user specifies

that they wish to include these processes in the resummation (although it will become default for HEJ to include them).

2. Ensuring that all possible processes are generated. Since the HEJ program is a Monte Carlo program, we must ensure that all of these extra NLL processes are ‘picked’. Since we are requiring a leading order matching, one consideration is that an NLL process should not be picked if the event will not be clustered into at least three jets. Also, given a set number of final state partons and a central $q\bar{q}$ emission, we must make sure that all positions of that emission along that chain are considered. Another point is that the rapidity ordering of the $q\bar{q}$ pair can be either way around and we must include both orderings. Failure to do any of this correctly will mean that the program will be artificially removing physics that we know is there.
3. Checking that the leading order matching at the jet level for the NLL processes is done consistently. For example, imagine we generate a central $q\bar{q}$ emission at the parton level and choose partons p_i and p_j for the pair, where p_i is more forward than and next to p_j in rapidity. In order to properly implement the matching, we require that these cluster into two different jets, $p_i \rightarrow j_i$ and $p_j \rightarrow j_j$, whereby j_i is more forward than and next to j_j in rapidity. Because of how the clustering works, it is not at all guaranteed that the jets will preserve this rapidity ordering and furthermore that these jets are even still next to each other in rapidity in the chain. All these considerations must be carefully checked.

It is absolutely crucial that all of these points are properly addressed and checked and so such a task is necessarily time consuming. After validating these steps by comparisons to old code with certain restraints, we can be confident that everything works as it should.

3.5 Results

One advantage of now being able to resum these partonic subprocesses and unordered events is that it means we have a reduced reliance on fixed order matching codes. Before, all process that were ‘non-FKL’ had to be included via a leading order matching. We have shown here that some of these non-FKL process can themselves be resummed and therefore we no longer need to include these

processes in the fixed order part. Figure 3.16 graphically shows the difference this makes. An analysis was run whereby we require at least three jets in the final state and the cross section broken down into the contribution coming from the resummation and the fixed order. It is desirable if the red line (the resummed contribution) is as close to the black line (the total contribution) as possible and it is clear from this plot that the addition of these partonic subprocesses is helping that in a significant way, reducing the relative contribution of the fixed order processes by a large fraction.

We can also revisit the predictions for previous analyses HEJ was involved in and investigate how these new additions help whilst comparing with real data. For example, in an ATLAS study of dijet production with a central jet veto [9]. One interesting plot is figure 6 of that paper, which is that of the average number of jets in the ‘gap’, defined as the rapidity region between the dijet system which in this case is given by the two highest p_T jets in an event. There are a total of four different lines which correspond to different rapidity slices shown in figure 3.17. From the top; $4 \leq \Delta y < 5$, $3 \leq \Delta y < 4$, $2 \leq \Delta y < 3$ and $1 \leq \Delta y < 2$. In order to differentiate them on the graph, these lines are moved up by 3, 2, 1 and 0 respectively. The x -axis is \bar{p}_t , which is the average of the dijet system’s transverse momenta. For the high energy limit HEJ considers, we should not expect this to be a good variable to plot in; the limit depends on all transverse scales being roughly the same order. At high average p_T , we can very easily construct a large p_T hierarchy. This is indeed reflected at the right hand side of the figure. It was noted that the analysis might have been better performed by considering only the resummed part of the HEJ calculation, since it is this part that is going to give rise to gap jets. We therefore include both the full and resummed only lines in this figure. In the diagram on the top left, we see a considerable difference between these two lines. By adding these new processes, we make these lines essentially indistinguishable and at the same time capture more bins on the left hand side of the plots, which is the only place we can reasonably expect improvement.

Furthermore, in a later dijet veto ATLAS analysis [11], it was observed that the predictions from the pure partonic HEJ needed to be interfaced with a parton shower in order to get the best description of the data. Although of course there are regions where a parton shower description is always going to be important, we can investigate to see if NLL effects can push the pure partonic line closer to the data by itself. For example, we can take a look at figure 3a of that paper. This figure plots the ‘Gap Fraction’, defined as the ratio of the cross section for dijet

events with no additional jets above a certain scale in the rapidity gap between the two jets to the cross section in total. Such an observable will clearly be sensitive to resummation effects, since we saw earlier that the rapidity gap plays a central role in the derivation of our amplitudes. In figure 3.18 we plot a comparison of data to four different HEJ runs, which correspond to the four different combinations of including/not including the unordered/sub-leading partonic processes corrections. For the same reasons as before, we plot both the resummed and full HEJ lines for comparison. The bottom right figure shows that the inclusion of both of these effects leads to a better description of the data everywhere, but in particular we ‘gain’ a few extra bins at the left side of the figure.

Finally, we revisit a four-jet ATLAS analysis [13]. This analysis is somewhat special in HEJ in that it includes matching for up to 5 jets in the final state (our usual approach is only up to 4). To compile the fixed order matrix elements for the 5 jet matching takes on the order of days and so is not practical to do generally. However, since this analysis specifically looks at four jet inclusive events, it was felt that it was necessary to have the matching to this level. In figure 3.19, we look at figure 4 of that paper which is a measurement of the inclusive cross section binned in leading jet p_T . As mentioned before, p_T is generally an observable that can be tricky to get right with the limit we consider, but we see here that if we make an inclusive measurement, we can describe the data remarkably well. Once more, the addition of the new processes make this measurement even better.

Make
last
figure
pret-
tier -
longer,
less
wide,
bet-
ter
la-
belling

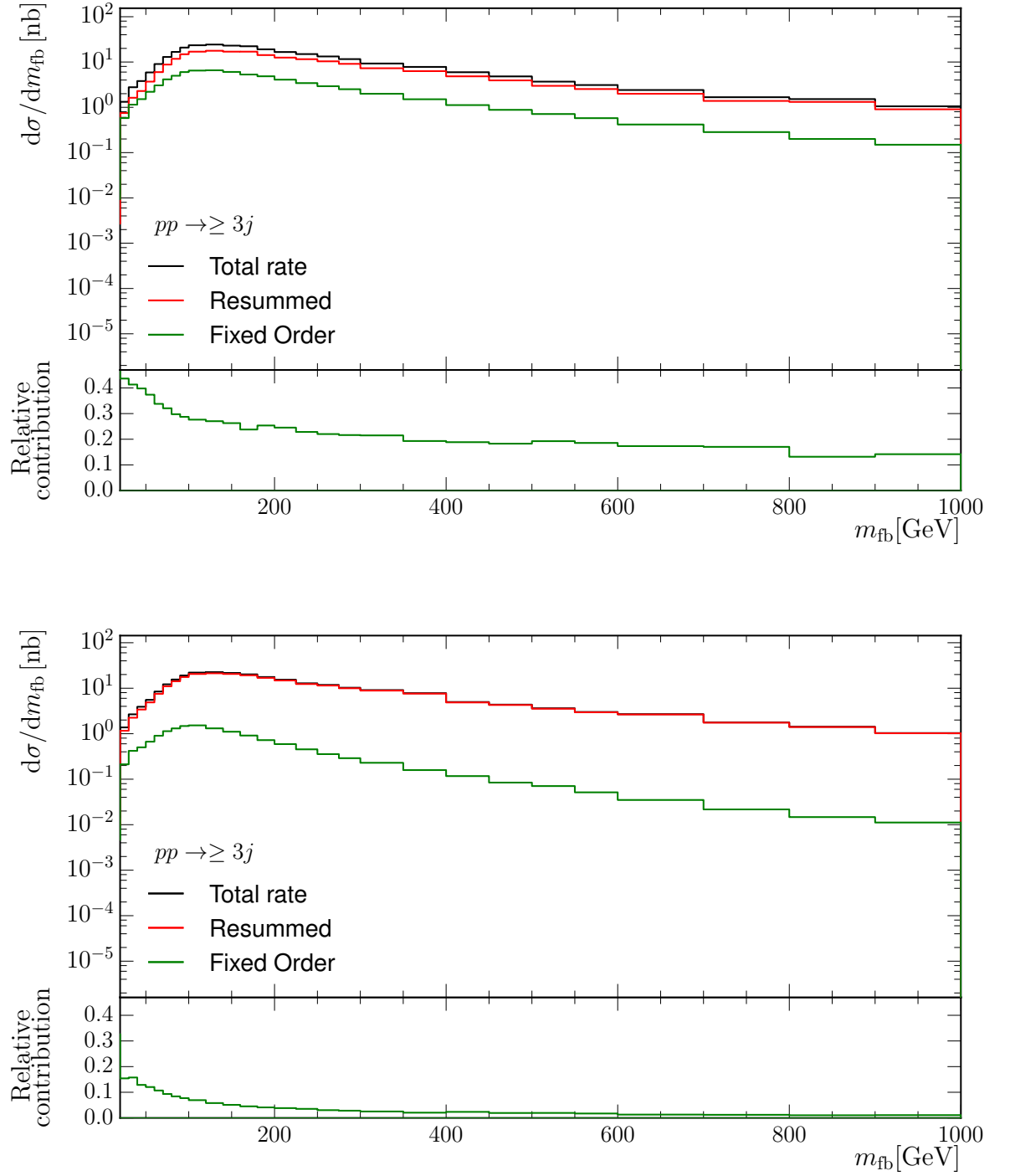


Figure 3.16 A breakdown of contributing parts to the jet cross section before (top) and after (bottom) implementing the effective vertex description of the new partonic subprocesses and the unordered events, in bins of the invariant mass between the most forward and backward jets.

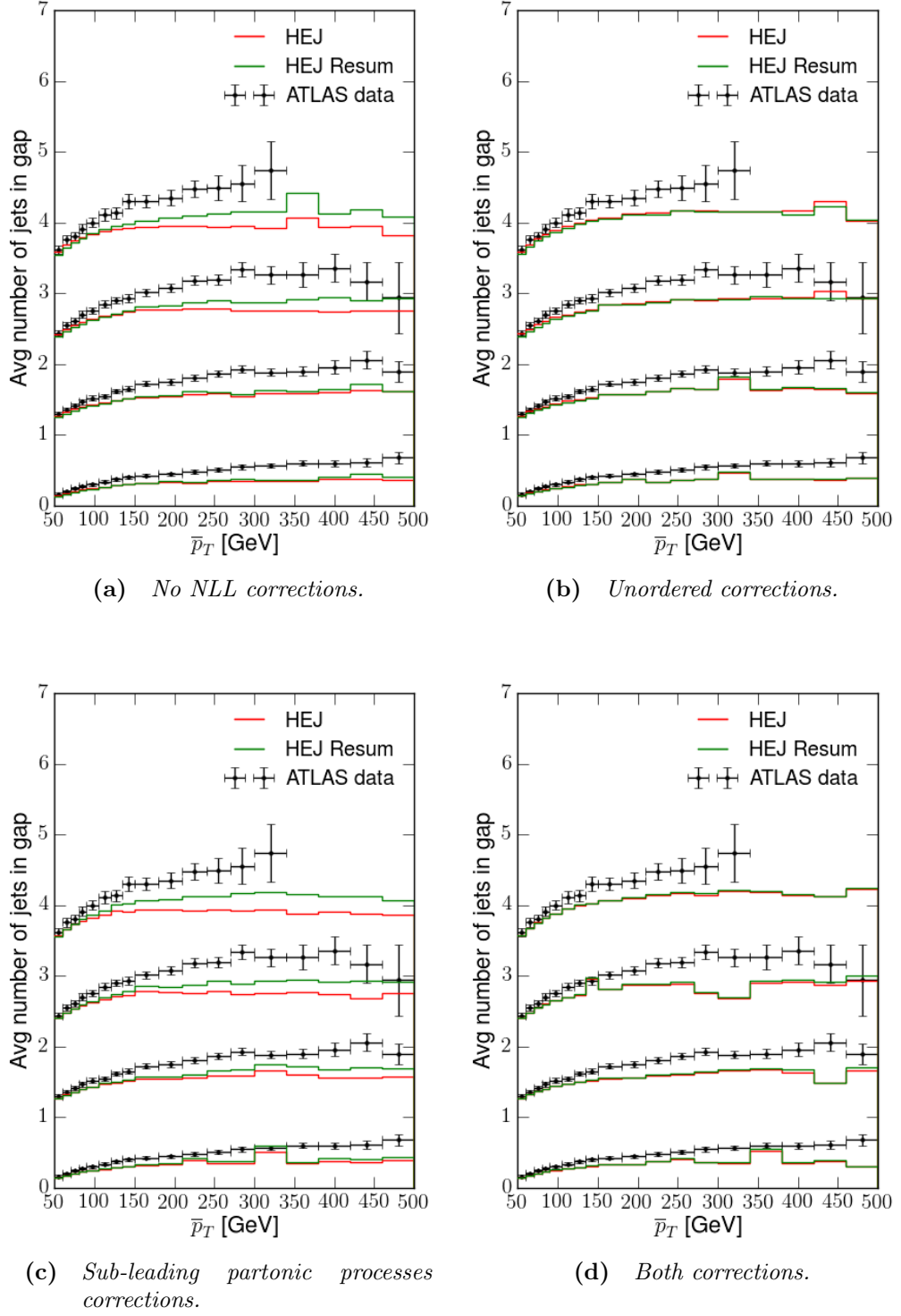
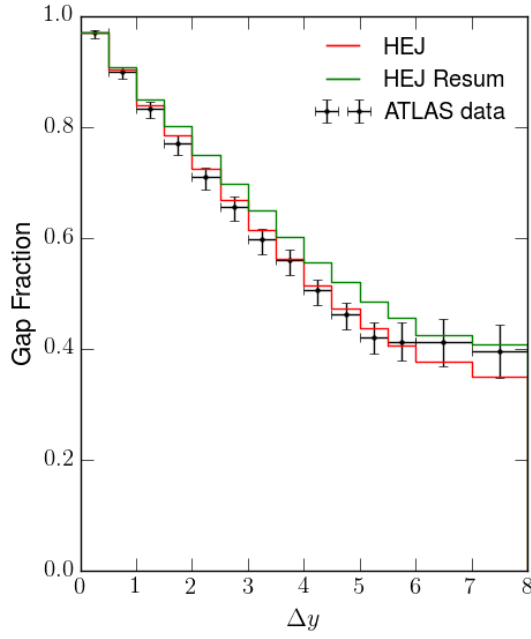
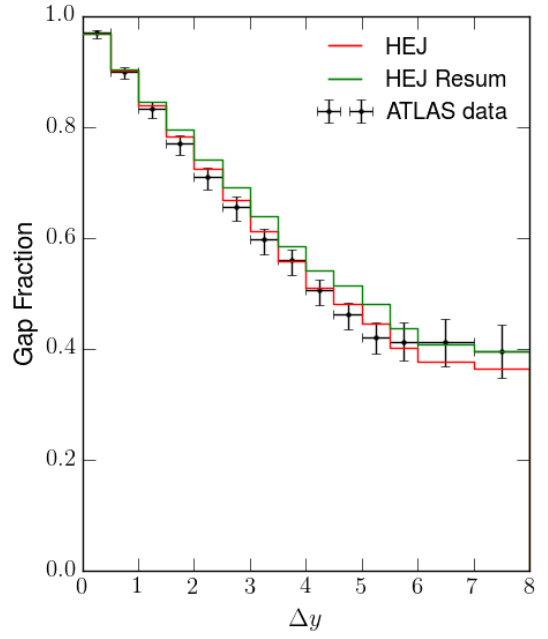


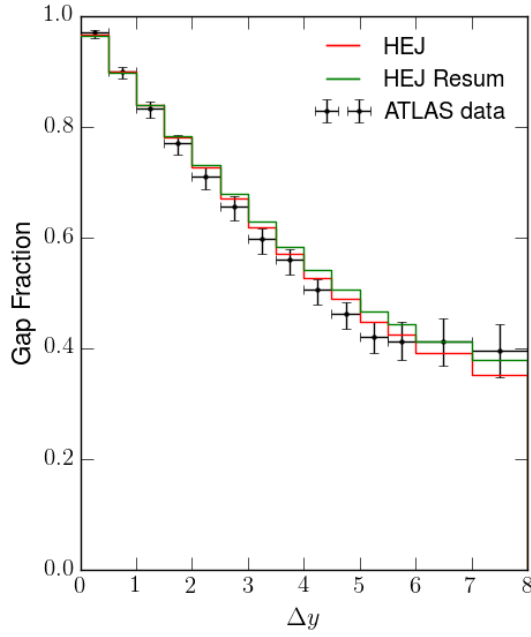
Figure 3.17 Figure 6 of [9] redone with corrections included. The red lines are the results from running the full HEJ program, the green if one only considers the resummed parts of the program and black points are the data. From the top left; no corrections, unordered corrections, sub-leading partonic processes corrections, both corrections. In the last figure, we see how these corrections mean that there is barely any distinction between ‘resummed’ and ‘full’ HEJ anymore.



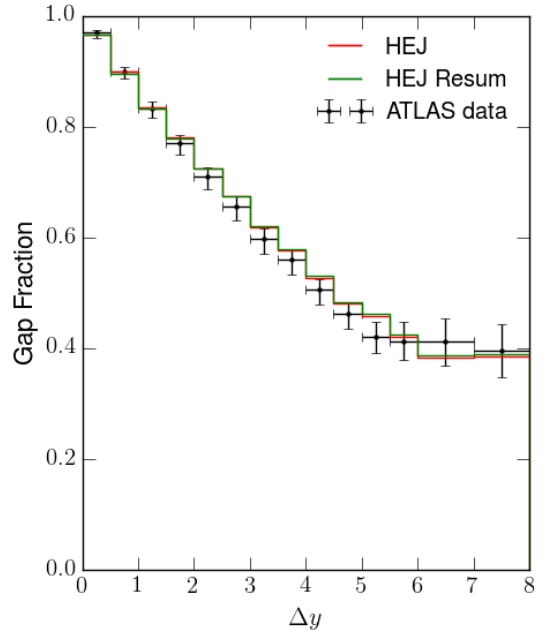
(a) *No NLL corrections.*



(b) *Unordered corrections.*

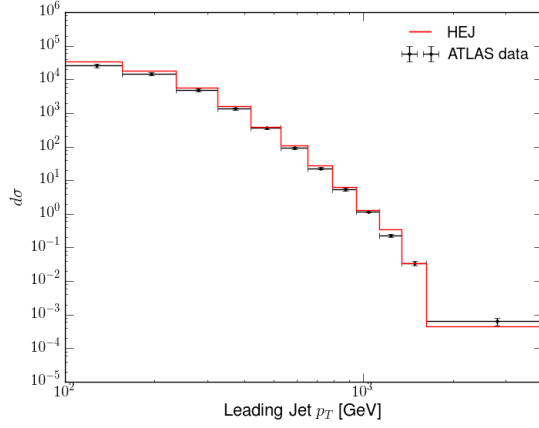


(c) *Sub-leading partonic processes corrections.*

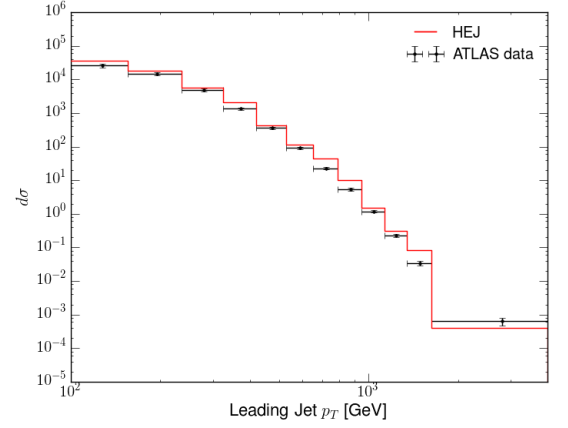


(d) *Both corrections.*

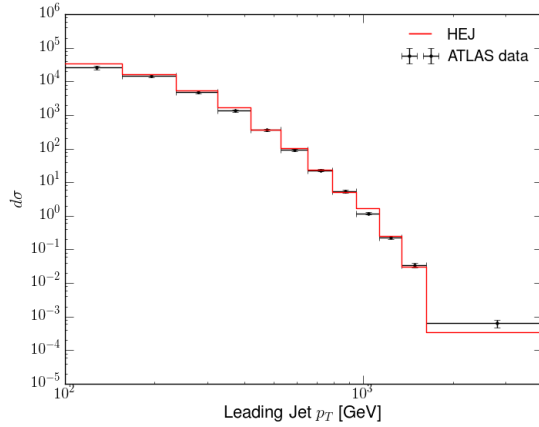
Figure 3.18 *Figure 3a of [11] redone with corrections included. The red lines are the results from running the full HEJ program, the green if one only considers the resummed parts of the program and black points are the data. From the top left; no corrections, unordered corrections, sub-leading partonic processes corrections, both corrections. In the last figure, we see how these corrections mean that there is barely any distinction between ‘resummed’ and ‘full’ HEJ anymore.*



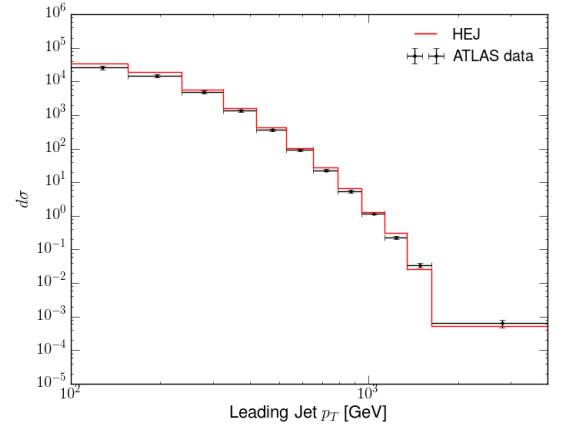
(a) *No NLL corrections.*



(b) *Unordered corrections.*



(c) *Sub-leading partonic processes corrections.*



(d) *Both corrections.*

Figure 3.19 *Figure 4 of [13] redone with corrections included. From the top left; no corrections, unordered corrections, sub-leading partonic processes corrections, both corrections.*

Chapter 4

Higgs Plus Jets with Finite Quark Mass Effects

It was briefly discussed that the addition of particles not charged under QCD such as the W^\pm , Z and Higgs bosons are included in HEJ by deriving an expression for the emission of the boson that does not interfere with the general factorisation process. In this chapter, we look more closely at how this is done for the case of the Higgs boson (or simply ‘ H ’) in a collection of limits. We will begin with the limit where the Higgs boson is emitted far apart from all other partons in rapidity and where the top quark mass is taken to infinity (the ‘infinite top mass limit’). Then we will relax the rapidity assumption on the Higgs and allow it to be produced close to an extremal parton in rapidity. Once this is established, we will consider the same rapidity situations but where we no longer use the infinite top mass limit and this will constitute the author’s own work. By the end of the chapter, we will have an expression that allows for the Leading Log resummation of Higgs plus at least two jets processes with full quark mass dependence, a calculation that is unique to HEJ.

4.1 The Infinite Top Mass Limit

If we wish to place a Higgs along our rapidity chain which consists of t -channel gluon exchanges, then it stands to reason that we need to couple the Higgs to the gluon in some fashion. However, the Higgs coupling to the gluon is zero because

the latter is a massless particle. Generally, what we need to do is couple the Higgs to a quark loop (the top loop is the most dominant, since the coupling depends on the mass of the particle that the Higgs is coupling to) which connects to the gluons in the chain. Loops generally complicate the calculation of an amplitude and thus even the calculation to leading order for this case is more involved than a pure QCD process. This will be demonstrated further in the later sections of this chapter. In order to get around this complication, theorists and phenomenologists sometimes take the limit where the top mass tends to infinity. This effectively ‘shrinks’ the quark loop to a point and so we end up with an *effective* gluon-gluon-Higgs coupling in our Lagrangian¹;

$$\mathcal{L}_{QCD+ggH} = \mathcal{L}_{QCD} + \frac{A}{4} G^{\mu\nu} G_{\mu\nu} H, \quad (4.1)$$

with $A = \frac{\alpha_s}{3\pi v}$ [24], resulting in the following Feynman rule for the effective ggH vertex [6];

$$V_H^{\mu\nu}(q_1, q_2) = A (\eta^{\mu\nu} q_1 \cdot q_2 - q_1^\nu q_2^\mu), \quad (4.2)$$

where q_1 is incoming to the vertex and q_2 outgoing. Since the Higgs does not carry colour information, we can simply insert this vertex into our FKL amplitude expression so long as the Higgs is far away from all other particles in rapidity. We encode this by first defining the spinor/Lorentz string;

$$S_{qQ \rightarrow qHQ}(q_1, q_2) = \langle 1|\mu|a\rangle (\eta^{\mu\nu} q_1 \cdot q_2 - q_1^\nu q_2^\mu) \langle 2|\nu|b\rangle. \quad (4.3)$$

With this, we can express the $qQ \rightarrow qHQ$ helicity and colour summed and

¹There is also a gluon-gluon-Higgs-Higgs interaction, but this thesis only concerns itself with single Higgs production and so we leave it out for brevity here.

averaged square of the amplitude as;

$$\begin{aligned}
|M_{qQ \rightarrow qHQ}^{HE,ggH}|^2 &= \frac{1}{4(N_C^2 - 1)} \|S_{qQ \rightarrow qHQ}(q_1, q_2)\|^2 \\
&\cdot \left(g^2 C_F \frac{1}{\hat{t}_1} \right) \\
&\cdot \left(\frac{1}{\hat{t}_1} \left(\frac{\alpha_s}{3\pi v} \right)^2 \frac{1}{\hat{t}_2} \right) \\
&\cdot \left(g^2 C_F \frac{1}{\hat{t}_2} \right).
\end{aligned} \tag{4.4}$$

The generalisation to multiple gluon emissions and different initial states follows as before by colour factor multiplications and additions of Lipatov vertices, though care is needed to keep track of which t -channel momenta are flowing into the Higgs vertex and which are flowing into Lipatov vertices. If instead the Higgs is emitted close to an extremal parton, then this decomposition is no longer valid and we have to include the contributions in some other fashion. Such contributions are included via the use of impact factors [24], which are strict high energy expressions that encapsulate this effect.

The infinite top mass limit is remarkably successful for predictions of inclusive variables like total cross sections. The reason for this is that the expansion of this effective coupling is a power series in $\frac{m_H^2}{4m_t^2} \sim 0.13$ and we essentially assume the top mass is the most relevant scale in the problem. It was checked that even the addition of a large dijet invariant mass in the amplitude had little effect [24]. However, if the transverse scales start to become larger than the top mass (in particular, the transverse scales of the gluons entering the effective vertex), there is significant deviation between the result obtained in the full and effective theories [24].

For HEJ, the infinite top mass limit was included because the expressions are simpler, but note that the factorisation of amplitudes will still occur whether or not this limit is taken. Therefore, any derived vertices for Higgs production with the full quark mass included can still be implemented in a straightforward way. Furthermore, as soon as the vertex including the full quark mass is derived, we can trivially add in the effect of more than one quark loop (for example, where a bottom quark runs in it). Such interference effects have been shown to produce

interesting effects at small p_T scales [34?]. For these reasons, we decided to implement the effect of finite quark masses in the HEJ formalism.

4.2 Calculations of $H + \text{jets}$ with Finite Quark Mass Effects

As discussed before, there are two rapidity cases to be discussed; the first where the Higgs is emitted centrally and the second where it is emitted close to an external parton. The base amplitude for the first is the $qQ \rightarrow qHQ$ amplitude and for the second it is the $gq \rightarrow Hgq$ amplitude. We will begin our discussion with the first case, since it will turn out to be remarkably simple.

4.2.1 $qQ \rightarrow qHQ$

The HEJ expression for the $qQ \rightarrow qHQ$ amplitude with full finite quark mass effects is shown diagrammatically in figure 4.1. In the previous section, we showed how the amplitude was derived in the infinite top mass limit. Because the factorisation properties of the amplitude are unchanged by moving away from this limit, the extension of this amplitude to the full finite quark mass dependent one is found by simply ‘undoing’ the infinite top mass limit on the vertex $V_H^{\mu\nu}$. Such an expression can essentially be looked up, for example in Appendix B of [24], so long as care is taken to ensure that incoming and outgoing momenta are labelled correctly. Keeping with the convention before that q_1 is incoming and q_2 outgoing, the vertex with a finite top mass is;

$$V_{H,m_t}^{\mu\nu}(q_1, q_2) = -\frac{4g_s^2 m_t^2}{v} [\eta^{\mu\nu} A_2(-q_1, q_2) + q_1^\nu q_2^\mu A_1(-q_1, q_2)], \quad (4.5)$$

where v is the Higgs vacuum expectation value (≈ 246 GeV) and A_1, A_2 depend on a combination of scalar integrals which appear via the integral reduction technique

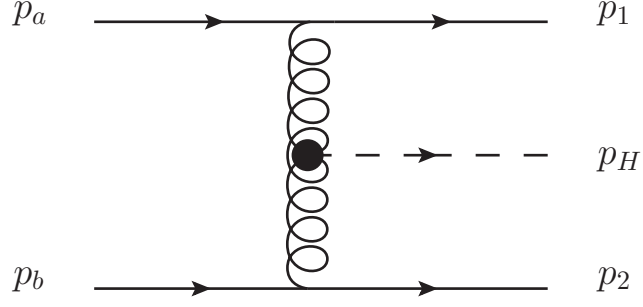


Figure 4.1 Diagrammatic representation of $qQ \rightarrow qHQ$ with an effective vertex for the production of the Higgs.

[?]. We first define ²;

$$\begin{aligned}
B_0(k) &= \int \frac{d^4q}{(2\pi)^4} \frac{1}{(q^2 - m_t^2)((q+k)^2 - m_t^2)}, \\
C_0(p, k) &= \int \frac{d^4q}{(2\pi)^4} \frac{1}{(q^2 - m_t^2)((q+p)^2 - m_t^2)((q+p+k)^2 - m_t^2)}, \\
Q &= -q_1 - q_2, \\
\Delta_3 &= (q_1^2)^2 + (q_2^2)^2 + (Q^2)^2 - 2q_1^2 q_2^2 - 2q_1^2 Q^2 - 2q_2^2 Q^2,
\end{aligned} \tag{4.6}$$

²The integral B_0 is actually divergent in 4 dimensions, but will always appear in combinations such that this divergence cancels in later functions.

which allows us to give the forms of A_1 and A_2 as;

$$\begin{aligned}
A_1(-q_1, q_2) &= C_0(-q_1, q_2) \left[\frac{4m_t^2}{\Delta_3} (Q^2 - q_1^2 - q_2^2) - 1 - \frac{4q_1^2 q_2^2}{\Delta_3} - \frac{12q_1^2 q_2^2 Q^2}{\Delta_3^2} (q_1^2 + q_2^2 - Q^2) \right] \\
&\quad - [B_0(q_2) - B_0(Q)] \left[\frac{2q_1^2}{\Delta_3} + \frac{12q_1^2 q_2^2}{\Delta_3^2} (q_2^2 - q_1^2 + Q^2) \right] \\
&\quad - [B_0(-q_1) - B_0(Q)] \left[\frac{2q_1^2}{\Delta_3} + \frac{12q_1^2 q_2^2}{\Delta_3^2} (q_1^2 - q_2^2 + Q^2) \right] \\
&\quad - \frac{2}{\Delta_3} \frac{i}{(4\pi)^2} (q_1^2 + q_2^2 - Q^2) \\
A_2(-q_1, q_2) &= C_0(-q_1, q_2) \left[2m_t^2 + \frac{1}{2} (q_1^2 + q_2^2 - Q^2) + \frac{2q_1^2 q_2^2 Q^2}{\Delta_3} \right] \\
&\quad + [B_0(q_2) - B_0(Q)] \frac{1}{\Delta_3} q_2^2 (q_2^2 - q_1^2 - Q^2) \\
&\quad + [B_0(-q_1) - B_0(Q)] \frac{1}{\Delta_3} q_1^2 (q_1^2 - q_2^2 - Q^2) \\
&\quad + \frac{i}{(4\pi)^2}.
\end{aligned} \tag{4.7}$$

The scalar integrals can either be evaluated numerically (via, for example, a program like LoopTools [35]) or again simply looked up³ and so the values of A_1 and A_2 can be worked out at any point. It can be numerically checked that;

$$\begin{aligned}
\lim_{m_t \rightarrow \infty} 4 \frac{g_s^2 m_t^2}{v} A_1(-q_1, q_2) &= iA, \\
\lim_{m_t \rightarrow \infty} 4 \frac{g_s^2 m_t^2}{v} A_2(-q_1, q_2) &= -iq_1 \cdot q_2 A,
\end{aligned} \tag{4.8}$$

and thus;

$$\lim_{m_t \rightarrow \infty} V_{H, m_t}^{\mu\nu} \rightarrow -iV_H^{\mu\nu}, \tag{4.9}$$

where the phase factor of $-i$ arises from a difference in convention and is unimportant since we are always taking the modulus squared of the amplitude.

³It is important to realise that most given results are valid only in certain kinematical regions, so care must be taken to pick the correct analytical formula.

We can therefore simply insert this vertex rather than the infinite top mass vertex into our amplitude to get the result;

$$\begin{aligned}
|M_{qQ \rightarrow qHQ}^{HE,ggH}|^2 &= \frac{1}{4(N_C^2 - 1)} \|S_{qQ \rightarrow qHQ}^{m_t}(q_1, q_2)\|^2 \\
&\cdot \left(g^2 C_F \frac{1}{\hat{t}_1}\right) \\
&\cdot \left(\frac{1}{\hat{t}_1} \left(\frac{-4g_s^2 m_t^2}{v}\right)^2 \frac{1}{\hat{t}_2}\right) \\
&\cdot \left(g^2 C_F \frac{1}{\hat{t}_2}\right).
\end{aligned} \tag{4.10}$$

with;

$$S_{qQ \rightarrow qHQ}^{m_t}(q_1, q_2) = \langle 1|\mu|a \rangle (\eta^{\mu\nu} A_2(-q_1, q_2) + q_1^\nu q_2^\mu A_1(-q_1, q_2)) \langle 2|\nu|b \rangle. \tag{4.11}$$

4.2.2 $gq \rightarrow Hgq$

The situation where the Higgs is emitted close to an extremal gluon involves a much more thorough calculation. We will start by finding the general leading order expression and then use knowledge of the high energy limit considered ($y_H \sim y_1 \gg y_2$) to again factorise the expression into the form HEJ requires, which would look diagrammatically like figure 4.2 and mathematically like;

$$M \sim \frac{Z^\mu(p_a, p_1, p_H) \langle 2|\mu|b \rangle}{\hat{t}_2}, \tag{4.12}$$

assuming that the polarisation vectors of the external gluons have been contracted with the effective vertex. There are 20 leading order diagrams to consider in total, which is reduced to 10 after invoking Furry's Theorem which states that diagrams involving an anti-quark loop can be related to diagrams with a quark loop. A selection of these diagrams is shown in figure 4.3. We will use [23] as a guide for our work. In particular, we choose to use the following function for our parametrisation of the top-quark triangle loop, keeping full top mass dependence;

$$T^{\mu_1\mu_2} = F_T(q_1^2, q_2^2, (q_1 + q_2)^2) T_T^{\mu_1\mu_2} + F_L(q_1^2, q_2^2, (q_1 + q_2)^2) T_L^{\mu_1\mu_2}, \tag{4.13}$$

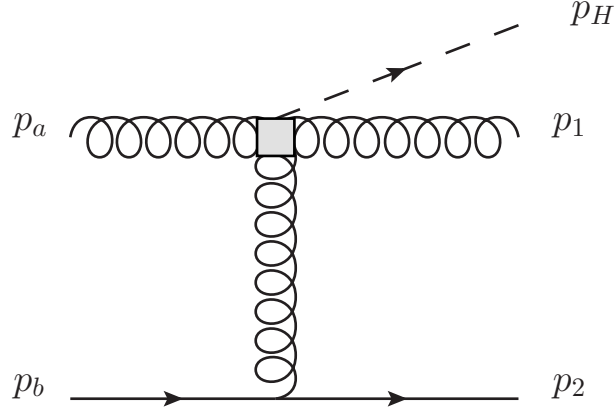


Figure 4.2 Diagrammatical representation of factorised $gq \rightarrow gHq$ expression.

where we have $T_T^{\mu_1\mu_2} = q_1 \cdot q_2 \eta^{\mu_1\mu_2} - q_1^{\mu_2} q_2^{\mu_1}$ and $T_L^{\mu_1\mu_2} = q_1^2 q_2^2 \eta^{\mu_1\mu_2} - q_1^2 q_2^{\mu_1} q_2^{\mu_2} - q_2^2 q_1^{\mu_1} q_1^{\mu_2} + q_1 \cdot q_2 q_1^{\mu_1} q_2^{\mu_2}$ and both q_1 and q_2 are going out from the triangle loop. In our calculation, we will thus need to remember to switch the sign of some momenta at points. The full forms for the F_L and F_T functions are;

$$\begin{aligned}
 F_L(q_1^2, q_2^2, Q^2) = & -\frac{1}{2\det\mathcal{Q}_2} \left\{ \left[2 - \frac{3q_1^2 q_2 \cdot Q}{2\det\mathcal{Q}_2} \right] (\tilde{B}_0(q_1) - \tilde{B}_0(Q)) \right. \\
 & + \left[2 - \frac{3q_2^2 q_1 \cdot Q}{2\det\mathcal{Q}_2} \right] (\tilde{B}_0(q_2) - \tilde{B}_0(Q)) \\
 & \left. - \left[4m_t^2 + q_1^2 + q_2^2 + Q^2 - \frac{3q_1^2 q_2^2 Q^2}{\det\mathcal{Q}_2} \right] \tilde{C}_0(q_1, q_2) \right\},
 \end{aligned} \tag{4.14}$$

where $\det\mathcal{Q}_2 = q_1^2 q_2^2 - (q_1 \cdot q_2)^2$. The scalar integrals with the tilde notation are related to the scalar integrals shown in equation 4.6 by multiplying the latter by $-16i\pi^2$ and the F_L and F_T functions are related to the A_1 and A_2 of equation 4.7 by;

$$\begin{aligned}
 A_1(q_1, q_2) &= \frac{i}{(4\pi)^2} F_T(q_1, q_2), \\
 A_2(q_1, q_2) &= \frac{i}{(4\pi)^2} (F_T(q_1, q_2) q_1 \cdot q_2 + F_L(q_1, q_2) q_1^2 q_2^2).
 \end{aligned} \tag{4.15}$$

An interesting point to notice is that, if one of the momenta q_1 or q_2 is on-shell, we only get a contribution from the F_T term in $T^{\mu\nu}$. This comes about because

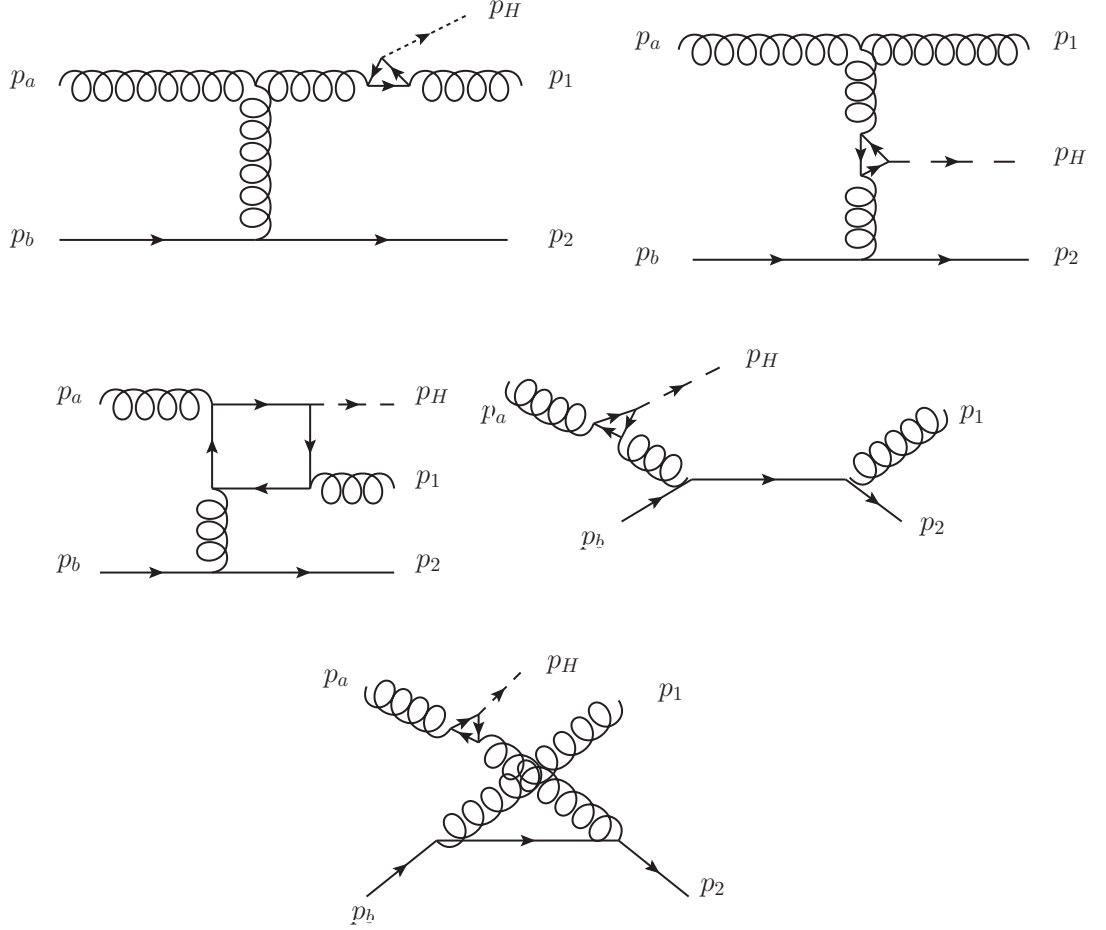


Figure 4.3 A selection of LO graphs for $gq \rightarrow Hgq$.

the presence of an on-shell momenta must mean that the vertex is going to be contracted with the relevant polarisation vector, setting the term proportional to F_L to zero. When this happens, we will write T_R in place of T to remind ourselves of this. Finally, since we know that every graph is contributing at the same order in α_s , has a Yukawa coupling from the top loop and has factors from loop integrals, we conveniently define;

$$F = \frac{4m_t^2}{v} \alpha_s^2, \quad (4.16)$$

and multiply F into every graph as in [23]. This slightly changes the Feynman rules for QCD that we should use in that all coupling information is now removed.

We now begin the process of finding the full LO expression. We start with the graph shown in the top left of figure 4.3, where the Higgs is emitted off of the

gluon leg with momentum p_1 . The Feynman rules yield;

$$A_1 = -F\varepsilon_{\mu_1}(p_a)f^{a1t}V_{3g}^{\mu_1\mu_2\mu_3}(p_a, -p_1 - p_H, -p_a + p_1 + p_H) \left(\frac{-i\eta_{\mu_2\mu_4}}{(p_1 + p_H)^2} \right) \quad (4.17)$$

$$T_R^{\mu_4\mu_5}(-p_1 - p_H, p_1)\varepsilon_{\mu_5}^*(p_1) \left(\frac{-i\eta_{\mu_3\mu_6}}{\hat{t}_2} \right) (-i)T_{2b}^t \langle 2|\mu_6|b \rangle ,$$

which can be cleaned up to give;

$$A_1 = \frac{-iFf^{a1t}T_{2b}^t}{(p_1 + p_H)^2\hat{t}_2}\varepsilon_{\mu_1}(p_a)V_{3g}^{\mu_1\mu_2\mu_3}(p_a, -p_1 - p_H, -p_a + p_1 + p_H) \quad (4.18)$$

$$\cdot T_{R,\mu_2}^{\mu_5}(-p_1 - p_H, p_1)\varepsilon_{\mu_5}^*(p_1) \langle 2|\mu_3|b \rangle .$$

The diagram where the Higgs is emitted off of the gluon with momentum p_a instead follows in essentially the same fashion and we just quote the final result of the calculation here, which is;

$$A_2 = \frac{-iFf^{a1t}T_{2b}^t}{(p_a - p_H)^2\hat{t}_2}\varepsilon_{\mu_1}(p_a)T_{R,\mu_3}^{\mu_1}(-p_a, p_a - p_H)V_{3g}^{\mu_3\mu_4\mu_5}(p_a - p_H, -p_1, -p_a + p_H + p_1) \quad (4.19)$$

$$\cdot \varepsilon_{\mu_4}^*(p_1) \langle 2|\mu_5|b \rangle .$$

We now look at the case where the Higgs is emitted from a t-channel gluon, as shown in the top right of figure 4.3. The Feynman rules give us;

$$A_3 = -F\varepsilon_{\mu_1}(p_a)f^{a1t}V_{3g}^{\mu_1\mu_2\mu_3}(p_a, -p_1, p_1 - p_a) \left(\frac{-i\eta_{\mu_3\mu_4}}{(p_a - p_1)^2} \right) \varepsilon_{\mu_2}^*(p_1) \quad (4.20)$$

$$\cdot T^{\mu_4\mu_5}(p_1 - p_a, p_a - p_1 - p_H) \left(\frac{-i\eta_{\mu_5\mu_6}}{\hat{t}_2} \right) (-i)T_{2b}^t \langle 2|\mu_6|b \rangle ,$$

which tidies up to;

$$A_3 = \frac{-iFf^{a1t}T_{2b}^t}{(p_a - p_1)^2 t_2} \varepsilon_{\mu_1}(p_a) V_{3g}^{\mu_1 \mu_2 \mu_3}(p_a, -p_1, p_1 - p_a) \varepsilon_{\mu_2}^*(p_1) \cdot T_{\mu_3}^{\mu_5}(p_1 - p_a, p_a - p_1 - p_H) \langle 2|\mu_5|b \rangle. \quad (4.21)$$

All of these three diagrams have had fairly complicated forms but are automatically factorised in the form we are searching for and so require no further work. The graph involving a box integral will also be like this, but we skip over that calculation for now due to the more complicated nature of it. We will instead discuss the other four diagrams which involve an s or u channel quark propagator. One such diagram is shown in the middle-right of figure 4.3. The Feynman rules for this diagram give;

$$A_4 = -iF T_{2q}^1 \varepsilon_{\mu_1}^*(p_1) \bar{u}_2 \gamma^{\mu_1} \left(\frac{i(\not{p}_1 + \not{p}_2)}{s_{12}} \right) \gamma^{\mu_2} u_b (-i) T_{qb}^a \left(\frac{-i\eta_{\mu_2 \mu_3}}{(p_a - p_H)^2} \right) \cdot T_R^{\mu_4 \mu_3}(-p_a, p_a + p_H) \varepsilon_{\mu_4}(p_a), \quad (4.22)$$

which one can tidy up to yield;

$$A_4 = \frac{-F T_{2q}^1 T_{qb}^a}{s_{12}(p_a - p_H)^2} \varepsilon_{\mu_1}^*(p_1) \bar{u}_2 \gamma^{\mu_1} (\not{p}_1 + \not{p}_2) \gamma^{\mu_2} u_b T_{R\mu_2}^{\mu_4}(-p_a, p_a - p_H) \varepsilon_{\mu_4}(p_a). \quad (4.23)$$

We have a similar diagram to this where there is still an s -channel quark but now the Higgs is emitted off of the p_1 leg. The calculation is almost identical so we just quote the result which is;

$$A_5 = \frac{-F T_{2q}^1 T_{qb}^a}{s_{ab}(p_1 + p_H)^2} \varepsilon_{\mu_2}(p_a) \bar{u}_2 \gamma^{\mu_1} (\not{p}_a + \not{p}_b) \gamma^{\mu_2} u_b T_{R\mu_1}^{\mu_4}(-p_1 - p_H, p_1) \varepsilon_{\mu_4}^*(p_1). \quad (4.24)$$

Finally, we have the u -type diagrams. One such is shown at the bottom of figure

4.3. The Feynman rules yield;

$$A_6 = -FT_{2q}^a T_{qb}^1 \bar{u}_2 \gamma^{\mu_1} \left(\frac{i(\not{p}_b - \not{p}_1)}{-s_{b1}} \right) \gamma^{\mu_2} u_b \varepsilon_{\mu_1}^*(p_1) \left(\frac{-i\eta_{\mu_2\mu_3}}{(p_a - p_H)^2} \right) \cdot T_R^{\mu_4\mu_3}(-p_a, p_a + p_H) \varepsilon_{\mu_4}(p_a). \quad (4.25)$$

This can be simplified to;

$$A_6 = \frac{FT_{2q}^a T_{qb}^1}{s_{1b}(p_a - p_H)^2} \bar{u}_2 \gamma^{\mu_1} (\not{p}_b - \not{p}_1) u_b \varepsilon_{\mu_1}^*(p_1) T_{R\mu_2}^{\mu_4}(-p_a, p_a + p_H) \varepsilon_{\mu_4}(p_a). \quad (4.26)$$

The last diagram is the same as this one except with the Higgs emitted off of the gluon with momentum p_1 and the result is;

$$A_7 = \frac{FT_{2q}^a T_{qb}^1}{s_{2a}(p_1 + p_H)^2} \bar{u}_2 \gamma^{\mu_1} (\not{p}_2 - \not{p}_a) u_b \varepsilon_{\mu_1}(p_a) T_{R\mu_2}^{\mu_4}(-p_1 - p_H, p_1) \varepsilon_{\mu_4}^*(p_1) \quad (4.27)$$

We now return to the box integrals. There are three independent contributions, related to the three different ways the two gluons and one Higgs can be attached to the box. For ease, we use the parametrisation as described in [24] (not as in [23], though they are of course related), which writes this part of the amplitude as;

$$M^{\mu\nu\rho} = \frac{2g_s^3 m t^2}{v} i f^{bac} T^c J^{\mu\nu\rho}(q_1, q_2, q), \quad (4.28)$$

in their notation. To get from their paper to this thesis we make the following mapping for momenta;

$$q_1 = p_1, \quad (4.29a)$$

$$q_2 = -p_a, \quad (4.29b)$$

$$q = p_a - p_1 - p_H = p_2 - p_b, \quad (4.29c)$$

and for the colour indices we map $a \rightarrow 1, b \rightarrow a, c \rightarrow t$. The last thing to do is to write this factor as also proportional to F ;

$$M^{\mu\nu\rho} = \left(F \times \frac{-16\pi^2}{2g_s} \right) f^{a1t} J^{\mu\nu\rho}. \quad (4.30)$$

A very important thing to notice here is that the paper this result is taken from has loop integrals defined with an overall factor of $\frac{1}{(2\pi)^4}$, whereas the loops used in LoopTools [35] (which is the program we will use in the Monte Carlo integration) and [23] are defined with an overall factor of $\frac{1}{i\pi^2}$. We take care of this by simply reweighing the LoopTools results when called here. For brevity, we will write the expression for J in terms of the q s rather than the momenta of the external particles. Lifting the expression from this paper also forces us to use a particular gauge, which is the one where the polarisation vector of the gluon with momenta p_a is perpendicular to p_1 and vice versa. Imposing this and the function J is;

$$J^{\mu\nu\rho} = \eta^{\mu\nu}(H_1 q_1^\rho + H_2 q_2^\rho) + \eta^{\mu\rho} H_4 q^\nu + \eta^{\nu\rho} H_5 q^\mu + H_{10} q_2^\rho q^\mu q^\nu + H_{12} q_1^\rho q^\mu q^\nu. \quad (4.31)$$

The full expressions for each of the H functions are very long and so we will leave their forms for Appendix A. A useful study is to investigate the link between the finite and infinite top mass cases for the box diagrams. This will, for example, give us a stringent numerical check on our implementation. In the infinite top mass case, the box diagram goes over to a three gluon vertex diagram multiplied by a factor, since the limit shrinks quark loops. Using this knowledge and applying it to the infinite top mass limit of equation 4.31 along with the factor F , we see

that the following must hold;

$$\begin{aligned}
\frac{2\pi F}{\alpha_s} H_1 &\rightarrow iA, \\
\frac{2\pi F}{\alpha_s} H_2 &\rightarrow -iA, \\
\frac{2\pi F}{\alpha_s} H_4 &\rightarrow iA, \\
\frac{2\pi F}{\alpha_s} H_5 &\rightarrow -iA, \\
\frac{2\pi F}{\alpha_s} H_{10} &\rightarrow 0, \\
\frac{2\pi F}{\alpha_s} H_{12} &\rightarrow 0,
\end{aligned} \tag{4.32}$$

with once more $A = \frac{\alpha_s}{3\pi v}$. This was tested numerically in a computer program by setting $M_t = 174000$ and seen to hold.

We can now combine all graphs together. We have three different colour structures appearing from the individual sub-amplitudes, but we use the fact that $[T^a, T^b] = if^{abc}T^c$ to see that we can reduce this down to two. For the time being, we will keep the amplitudes separated into their ‘natural’ colour factor and then later on use our commutator identities. Before we write the full amplitude, we make use of one more useful piece of notation. Throughout the calculation, we came across many instances where one of the polarisation vectors was contracted with a T_R function from the top loop. It will be useful to define an ‘effective polarisation vector’ which is precisely this contraction along with the propagator invariant. In other words;

$$\begin{aligned}
\frac{\varepsilon_{\mu_1}(p_a) T_R^{\mu_1}_{\mu_2}(-p_a, p_a - p_H)}{(p_a - p_H)^2} &= \frac{F_T(p_a^2, (p_a - p_H)^2, p_H^2) (p_a \cdot p_H \varepsilon_{\mu_2}(p_a) - p_{a\mu_2} p_H \cdot \varepsilon(p_a))}{(p_a - p_H)^2} \\
&\equiv \varepsilon_{H, \mu_2}(p_a),
\end{aligned} \tag{4.33a}$$

$$\begin{aligned}
\frac{\varepsilon_{\mu_1}^*(p_1) T_{R\mu_2}^{\mu_1}(-p_1 - p_H, p_1)}{(p_1 + p_H)^2} &= \frac{F_T((p_1 + p_H)^2, p_1^2, p_H^2) (p_H \cdot \varepsilon^*(p_1) p_{1\mu_2} - p_1 \cdot p_H \varepsilon_{\mu_2}^*(p_1))}{(p_1 + p_H)^2} \\
&\equiv \varepsilon_{H,\mu_2}^*(p_1).
\end{aligned} \tag{4.33b}$$

Note that the idea of the effective polarisation tensor has been taken from [23], but the forms look quite different due to the differences between incoming/outgoing momenta. The full amplitude is then;

$$\begin{aligned}
M_{gq \rightarrow Hgq}^{m_t} = F &\left(T_{2q}^a T_{qb}^1 \left[\frac{\bar{u}_2 \gamma^{\mu_1} (\not{p}_2 - \not{p}_a) \gamma^{\mu_2} u_b \varepsilon_{\mu_1}(p_a) \varepsilon_{H,\mu_2}^*(p_1)}{s_{2a}} \right. \right. \\
&+ \left. \frac{\bar{u}_2 \gamma^{\mu_1} (\not{p}_b - \not{p}_1) \gamma^{\mu_2} u_b \varepsilon_{H,\mu_1}(p_a) \varepsilon_{\mu_2}^*(p_1)}{s_{1b}} \right] - \\
&T_{2q}^1 T_{qb}^a \left[\frac{\bar{u}_2 \gamma^{\mu_1} (\not{p}_a + \not{p}_b) \gamma^{\mu_2} u_b \varepsilon_{\mu_2}(p_a) \varepsilon_{H,\mu_1}^*(p_1)}{s_{ab}} \right. \\
&+ \left. \frac{\bar{u}_2 \gamma^{\mu_1} (\not{p}_1 + \not{p}_2) \gamma^{\mu_2} u_b \varepsilon_{\mu_1}^*(p_1) \varepsilon_{H,\mu_2}(p_a)}{s_{12}} \right] \\
&- [T^a, T^1]_{2b} \frac{\langle 2|\mu_3|b \rangle}{t_2} \left[8i\pi^2 \varepsilon_{\mu_2}(p_a) \varepsilon_{\mu_1}^*(p_1) J^{\mu_1\mu_2\mu_3}(p_1, -p_a, p_a - p_1 - p_H) \right. \\
&+ \varepsilon_{H,\mu_1}(p_a) V_{3g}^{\mu_1\mu_2\mu_3}(p_a - p_H, -p_1, -p_a + p_H + p_1) \varepsilon_{\mu_2}^*(p_1) \\
&+ \varepsilon_{\mu_1}(p_a) V_{3g}^{\mu_1\mu_2\mu_3}(p_a, -p_1 - p_H, -p_a + p_1 + p_H) \varepsilon_{H,\mu_2}^*(p_1) \\
&+ \left. \frac{\varepsilon_{\mu_1}(p_a) V_{3g}^{\mu_1\mu_2\mu_4}(p_a, -p_1, p_1 - p_a) \varepsilon_{\mu_2}^*(p_1) T_{\mu_4}^{\mu_3}(p_1 - p_a, p_a - p_1 - p_H)}{(p_a - p_1)^2} \right] \Bigg).
\end{aligned} \tag{4.34}$$

This expression has been checked term-by-term with [23] and [24] and agreement has been found. With the full amplitude known, we can hope to use limiting arguments to factorise the expression into the form we require. To do this, we need to focus on the first four terms in the amplitude, since the other terms are already in the correct form. These four terms have elements of the desired form within them. To see this, consider the numerator of the first term;

$$A_1^{num} = \bar{u}_2 \gamma^{\mu_1} (\not{p}_2 - \not{p}_a) \gamma^{\mu_2} u_b \varepsilon_{\mu_1}(p_a) \varepsilon_{H,\mu_2}^*(p_1). \tag{4.35}$$

With the completeness relation, we can rewrite the \not{p} parts in terms of massless spinors, $\not{p} = |p^+\rangle\langle p^+| + |p^-\rangle\langle p^-|$. By considering the action of the projection operator $(1 \pm \gamma^5)$ it is simple to see that you only pick out one of these helicity projections, which is the helicity projection corresponding to the helicity of particles b and 2. Thus we can write the term as;

$$A_1^{num} = (\langle 2|\mu_1|2\rangle \langle 2|\mu_2|b\rangle + \langle 2|\mu_1|a\rangle \langle a|\mu_2|b\rangle) \varepsilon_{\mu_1}(p_a) \varepsilon_{H,\mu_2}^*(p_1). \quad (4.36)$$

We recall at this point a useful parametrisation for our gluon polarisation vectors, as detailed in [26];

$$\varepsilon_\mu^\pm(k, q) = \pm \frac{\langle q^\mp | \mu | k^\mp \rangle}{\sqrt{2} \langle q^\mp | k^\pm \rangle}, \quad (4.37)$$

where k is the momenta of the gluon and q is an arbitrary, massless, reference momenta which reflects our gauge freedom. This notation is useful because it allows us to apply some of the identities we established in section 1.6 to perform dot products. As previously discussed, the parametrisation of the box function requires that we pick the following gauge for the gluon polarisation vectors;

$$\begin{aligned} \varepsilon_\mu^\pm(p_a) &= \pm \frac{\langle 1^\mp | \mu | a^\mp \rangle}{\sqrt{2} \langle 1^\mp | a^\pm \rangle}, \\ \varepsilon_\mu^\pm(p_1) &= \pm \frac{\langle a^\mp | \mu | 1^\mp \rangle}{\sqrt{2} \langle 1^\mp | a^\pm \rangle}. \end{aligned} \quad (4.38)$$

Using this, we can perform the μ_1 contraction in 4.36 and see that if the spinor chain and the polarisation vector $\varepsilon(p_a)$ have the same helicity, the second term is identically zero. However, if they have opposite helicity, then the dot product goes like $\langle a1 \rangle [a2]$. The first term will instead go like $\langle 21 \rangle [a2]$. We can think of the square and angled brackets as square roots of invariants, so the ratio of these terms is like $\sqrt{s_{a1}/s_{12}}$. Since we are considering the limit where s_{12} is large and s_{a1} not necessarily so, we can then neglect the second term. This will apply also to the \not{p}_a part of the third term of the full amplitude and a similar argument can be made for the \not{p}_1 part of the second term and the \not{p}_1 part of the fourth. Thus

we have now approximated the first four terms as;

$$\tilde{A} \equiv iF \left(T_{2q}^a T_{qb}^1 \left[\frac{\bar{u}_2 \gamma^{\mu_1} \not{p}_2 \gamma^{\mu_2} u_b \varepsilon_{\mu_1}(p_a) \varepsilon_{H,\mu_2}^*(p_1)}{s_{2a}} + \frac{\bar{u}_2 \gamma^{\mu_1} \not{p}_b \gamma^{\mu_2} u_b \varepsilon_{H,\mu_1}(p_a) \varepsilon_{\mu_2}^*(p_1)}{s_{1b}} \right] - T_{2q}^1 T_{qb}^a \left[\frac{\bar{u}_2 \gamma^{\mu_1} \not{p}_b \gamma^{\mu_2} u_b \varepsilon_{\mu_2}(p_a) \varepsilon_{H,\mu_1}^*(p_1)}{s_{ab}} + \frac{\bar{u}_2 \gamma^{\mu_1} \not{p}_2 \gamma^{\mu_2} u_b \varepsilon_{\mu_1}^*(p_1) \varepsilon_{H,\mu_2}(p_a)}{s_{12}} \right] \right). \quad (4.39)$$

Because we will be performing contractions and evaluating spinor brackets with the polarisation vectors, we will rewrite them in a different (though of course equivalent) form that we know for sure conforms with our spinor definitions. The formula we quoted from [26] is designed for the case where all momenta are taken as outgoing, so when it comes to writing out these contractions explicitly (not just schematically like we did for the scaling argument) we cannot be confident that the convention is the same. Thus, our polarisation vectors for explicit calculations are;

$$\varepsilon(p_a)^+ = \frac{\langle a^- | \mu | 1^- \rangle}{\sqrt{2}[a1]} = \frac{\langle 1^+ | \mu | a^+ \rangle}{\sqrt{2}[a1]}, \quad (4.40a)$$

$$(\varepsilon(p_1)^+)^* = -\frac{\langle a^- | \mu | 1^- \rangle}{\sqrt{2}\langle 1a \rangle} = -\frac{\langle 1^+ | \mu | a^+ \rangle}{\sqrt{2}\langle 1a \rangle}, \quad (4.40b)$$

$$\varepsilon(p_a)^- = \frac{\langle 1^- | \mu | a^- \rangle}{\sqrt{2}\langle 1a \rangle} = \frac{\langle a^+ | \mu | 1^+ \rangle}{\sqrt{2}\langle 1a \rangle}, \quad (4.40c)$$

$$(\varepsilon(p_1)^-)^* = -\frac{\langle 1^- | \mu | a^- \rangle}{\sqrt{2}[a1]} = -\frac{\langle a^+ | \mu | 1^+ \rangle}{\sqrt{2}[a1]}. \quad (4.40d)$$

We now expand our expression for \tilde{A} using the completeness relation;

$$\tilde{A} \equiv F \left(T_{2q}^a T_{qb}^1 \left[\frac{2p_2^{\mu_1} \langle 2 | \mu_2 | b \rangle \varepsilon_{\mu_1}(p_a) \varepsilon_{H,\mu_2}^*(p_1)}{s_{2a}} + \frac{\langle 2 | \mu_1 | b \rangle 2p_b^{\mu_2} \varepsilon_{H,\mu_1}(p_a) \varepsilon_{\mu_2}^*(p_1)}{s_{1b}} \right] - T_{2q}^1 T_{qb}^a \left[\frac{\langle 2 | \mu_1 | b \rangle 2p_b^{\mu_2} \varepsilon_{\mu_2}(p_a) \varepsilon_{H,\mu_1}^*(p_1)}{s_{ab}} + \frac{2p_2^{\mu_1} \langle 2 | \mu_2 | b \rangle \varepsilon_{\mu_1}^*(p_1) \varepsilon_{H,\mu_2}(p_a)}{s_{12}} \right] \right). \quad (4.41)$$

Note that we have not made any choice on the helicity of the quark line $\langle 2|\mu|b\rangle$ nor will we need to; we aim to factor out this string from our expression and the terms $2p_b$ and $2p_2$ will appear regardless of the helicity choice. We will now explicitly calculate the contractions with the polarisation vectors using the same spinor convention as outlined in section 1.6. Since our aim is to remove all p_b and p_2 dependence from our effective vertex, it will be useful to consider which spinor bracket combinations are independent of these. Two useful results are (we will assume p_a is moving in the $+$ direction for now, but generalise later);

$$\frac{[1b]}{[ba]} = -\sqrt{\frac{p_1^+}{p_a^+}}, \quad (4.42a)$$

$$\frac{\langle ba \rangle}{\langle 1b \rangle} = -\sqrt{\frac{p_a^+}{p_1^+}}. \quad (4.42b)$$

These are exact. However, if we consider the limit $p_2^- \sim p_b^-$ that is still valid here, then we have additional, approximate results we can use. For example;

$$\langle 12 \rangle = \sqrt{p_2^+ p_1^-} e^{i\phi_1} - \sqrt{p_2^- p_1^+} e^{i\phi_2} \approx -\sqrt{p_2^- p_1^+} e^{i\phi_2}, \quad (4.43)$$

where we use the fact that both p_2^+ and p_1^- are suppressed in comparison to p_2^- and p_1^+ . Using this, we also use the results (we will use an equality sign, but remember that the equality is only truly realised in the high energy limit);

$$\frac{[12]}{[a2]} = \sqrt{\frac{p_1^+}{p_a^+}}, \quad (4.44a)$$

$$\frac{\langle a2 \rangle}{\langle 12 \rangle} = \sqrt{\frac{p_a^+}{p_1^+}}. \quad (4.44b)$$

Let us now return to our expression for \tilde{A} . We calculate the dot product between the pure momentum term (either p_b or p_2) and the polarisation vector. There are two cases we need to consider; firstly, when the helicity of the gluons with momentum p_a and p_1 are the same (helicity-conserving) and secondly, when they differ (helicity non-conserving). Though there are of course four total choices for the helicities, we need only consider two, being able to get the other two by parity relations. We start with the helicity-conserving case and choose gluons $a, 1$ to

both have positive helicity. The first term is;

$$\begin{aligned} \frac{2p_2^{\mu_1} \langle 2|\mu_2|b\rangle \varepsilon_{\mu_1}^+(p_a) \varepsilon_{H,\mu_2}^{+,*}(p_1)}{s_{2a}} &= \frac{2 \langle 2a \rangle [12] \langle 2|\mu_2|b\rangle \varepsilon_{H,\mu_2}^{+,*}(p_1)}{\sqrt{2}[a1] \langle 2a \rangle [a2]} \\ &= \frac{\sqrt{2} \langle 2|\mu_2|b\rangle \varepsilon_{H,\mu_2}^{+,*}(p_1)}{[a1]} \sqrt{\frac{p_1^+}{p_a^+}}, \end{aligned} \quad (4.45)$$

and therefore (once we factor out the spinor current) is completely independent of both p_b and p_2 . Similar results occur with the other three terms and, in fact, terms 1 and 3 and 2 and 4 will become equal. At that point, we can rewrite \tilde{A} as proportional to the colour commutator $[T^a, T^1]$. The result is;

$$\tilde{A}_{++} = \sqrt{2}F[T^a, T^1] \langle 2|\mu|b\rangle \left(\sqrt{\frac{p_1^+}{p_a^+}} \frac{\varepsilon_{H,\mu}^{+,*}(p_1)}{[a1]} - \sqrt{\frac{p_a^+}{p_1^+}} \frac{\varepsilon_{H,\mu}^+(p_a)}{\langle 1a \rangle} \right). \quad (4.46)$$

For the helicity non-conserving case, we choose the helicity of the gluon with momentum p_a to be positive and the other gluon to have negative helicity, yielding similar results:

$$\tilde{A}_{+-} = \sqrt{2}F[T^a, T^1] \frac{\langle 2|\mu|b\rangle}{[a1]} \left(\sqrt{\frac{p_1^+}{p_a^+}} \varepsilon_{H,\mu}^{-,*}(p_1) - \sqrt{\frac{p_a^+}{p_1^+}} \varepsilon_{H,\mu}^+(p_a) \right). \quad (4.47)$$

If instead we chose p_a to be moving in the - direction, we find by direction calculation that we need to multiply \tilde{A}_{++} and the first term of \tilde{A}_{+-} by $-\frac{p_{1,\perp}^*}{|p_{1,\perp}|^2}$ and the second term of \tilde{A}_{+-} by $-\frac{p_{1,\perp}}{|p_{1,\perp}|^2}$.

We have now achieved our goal of creating a factorised matrix element. Before we write down the explicit expressions for that, we consider if the form can be made to look simpler. For example, in the helicity conserving case, our gauge actually sets one diagram identically zero. The graph shown in the top right of figure 4.3 has a part which is a three-gluon vertex contracted with symmetric polarisation vectors that depend only on the momenta along the top line. It is easy to show by direct calculation that this yields a result of zero. Because we are going to implement this in a numerical integration program, it is important to find these contributions where the analytical result is zero because, depending

on the accuracy of the calculation, a computer might give you a small (but vitally non-zero) answer that could potentially hurt your integration.

We now have everything we need to state the result of $gq \rightarrow Hgq$ in the limit where the Higgs is emitted close to the gluon in rapidity space. For our High Energy expressions, we will present a form which will conform with equation 4.12 by performing some of the index contractions. After some manipulation, we find for the helicity conserving amplitude (we will take p_a to be moving in the + direction, but recall that we know how to immediately get to the situation where it is going in the - direction);

$$\begin{aligned}
A_{++} = & F[T^a, T^1] \frac{\langle 2|\mu|b\rangle}{\hat{t}_2} \left[\sqrt{\frac{2p_1^+}{p_a^+}} \frac{\varepsilon_{H,\mu}^{+,*}(p_1)\hat{t}_2}{[a1]} - \sqrt{\frac{2p_a^+}{p_1^+}} \frac{\varepsilon_{H,\mu}^+(p_a)\hat{t}_2}{\langle 1a\rangle} \right. \\
& + \frac{\langle 1^+|H|a^+\rangle}{\sqrt{2}\langle 1a\rangle} \varepsilon_{H,\mu}^+(p_a) + \frac{\langle 1^+|H|a^+\rangle}{[a1]} \varepsilon_{H,\mu}^{+,*}(p_1) \\
& - \frac{\sqrt{2}F_{Ta}p_a \cdot p_1 \langle 1^+|H|a^+\rangle}{[a1]} \varepsilon_{\mu}^{+,*}(p_1) - \frac{\sqrt{2}F_{T1}p_a \cdot p_1 \langle 1^+|H|a^+\rangle}{\langle 1a\rangle} \varepsilon_{\mu}^+(p_a) \quad (4.48) \\
& - \frac{\langle 1^+|H|a^+\rangle}{\sqrt{2}[a1]} \varepsilon_{\mu}^{+,*}(p_1) RH_4 + \frac{\langle 1^+|H|a^+\rangle}{\sqrt{2}\langle 1a\rangle} \varepsilon_{\mu}^+(p_a) RH_5 \\
& \left. + \frac{\langle 1^+|H|a^+\rangle^2}{2\langle 1a\rangle[a1]} \{p_{a,\mu} RH_{10} - p_{1,\mu} RH_{12}\} \right]
\end{aligned}$$

where we have introduced the notation $F_{Ta} = \frac{F_T(0,(p_a-p_H)^2,m_H^2)}{(p_a-p_H)^2}$, $F_{T1} = \frac{F_T((p_1+p_H)^2,0,m_H^2)}{(p_1+p_H)^2}$ and $R = 8i\pi^2$. The part in the square brackets can be interpreted directly (or along with some of the overall constants) as the effective vertex we were searching for, in the helicity conserving case. What remains then, is the helicity

non-conserving case which is given by;

$$\begin{aligned}
A_{+-} = & F[T^a, T^1] \frac{\langle 2|\mu|b\rangle}{\hat{t}_2} \left[\sqrt{\frac{2p_1^+}{p_a^+}} \frac{\varepsilon_{H,\mu}^{+,*}(p_1)\hat{t}_2}{[a1]} - \sqrt{\frac{2p_a^+}{p_1^+}} \frac{\varepsilon_{H,\mu}^+(p_a)\hat{t}_2}{[a1]} \right. \\
& + \frac{\langle 1^+|H|a^+\rangle}{\sqrt{2}[a1]} \varepsilon_{H,\mu}^+(p_a) + \frac{\langle 1^+|H|a^+\rangle}{[a1]} \varepsilon_{H,\mu}^{+,*}(p_1) \\
& - \frac{\sqrt{2}F_{Ta}p_a \cdot p_1 \langle 1^+|H|a^+\rangle}{[a1]} \varepsilon_\mu^{+,*}(p_1) - \frac{\sqrt{2}F_{T1}p_a \cdot p_1 \langle 1^+|H|a^+\rangle}{[a1]} \varepsilon_\mu^+(p_a) \\
& - \frac{\langle 1^+|H|a^+\rangle}{\sqrt{2}[a1]} \varepsilon_\mu^{+,*}(p_1) RH_4 + \frac{\langle 1^+|H|a^+\rangle}{\sqrt{2}[a1]} \varepsilon_\mu^+(p_a) RH_5 \\
& + \frac{\langle 1^+|H|a^+\rangle^2}{2[a1]^2} \{p_{a,\mu} RH_{10} - p_{1,\mu} RH_{12}\} \\
& + e^{i\phi} RH_1 p_1^\mu - e^{i\phi} RH_2 p_a^\mu + 2e^{i\phi} F_{T1} p_1 \cdot p_H p_a^\mu - 2e^{i\phi} F_{Ta} p_a \cdot p_H p_1^\mu \\
& - e^{i\phi} (p_a + p_1)^\mu F_\alpha \frac{(p_1 - p_a) \cdot (p_a - p_1 - p_H)}{(p_a - p_1)^2} \\
& + e^{i\phi} (p_a - p_1 - p_H) \cdot (p_a + p_1) \frac{(p_1 - p_a)}{(p_a - p_1)^2} F_\alpha \\
& \left. - e^{i\phi} F_\beta (p_a - p_1 - p_H)^2 (p_a + p_1)^\mu \right] \tag{4.49}
\end{aligned}$$

where we have $F_\alpha = F_T(p_1 - p_a, p_a - p_1 - p_H, p_H)$, $F_\beta = F_L(p_1 - p_a, p_a - p_1 - p_H, p_H)$ and $\varepsilon_\mu^{+,*}(p_1) \cdot \varepsilon_\mu^+(p_a) = e^{i\phi}$ as the phase factor that comes out of dotting the polarisation vectors.

With both the helicity conserving and non-conserving vertices found, we are able to provide a high energy approximation to the whole amplitude by manually performing the colour/helicity sum/average. The colour sum is simple, since the approximation is proportional only to $f^{a1t}T^t$ and, using the normalisation $Tr(T^a T^b) = \frac{1}{2}$, we find that the sum yields an answer of 12. Since we have a quark and gluon incoming, the average factor is $\frac{1}{3 \times 8} = \frac{1}{24}$. For the helicities, there are total of 8 combinations, of which we need only work out 4 because the other 4 are related by parity and we average by a factor of 4. This gives our full approximation to be (where the subscripts refer to the helicities of particles with

momenta p_a, p_1, p_2 & p_b respectively and P is the parity operation);

$$|M_{gq \rightarrow Hgq}^{m_t, HE}|^2 = \frac{1}{8} (|A_{++,-}|^2 + |A_{++,+}|^2 + |A_{+,-}|^2 + |A_{+,-,+}|^2 + |P(A_{++,-})|^2 + |P(A_{++,+})|^2 + |P(A_{+,-})|^2 + |P(A_{+,-,+})|^2). \quad (4.50)$$

4.2.3 Checks and Verifications of Amplitudes

Given recent advances in MadGraph, we are able to check our result against a full LO implementation, complete with finite top mass effects. We first decide to check a phase space configuration where the Higgs boson is kept central in rapidity and the two extremal jets are allowed to move further and further apart. The precise momentum configuration used is;

$$p_1 = (40\sqrt{2} \cosh(\Delta), -40, 40, 40\sqrt{2} \sinh(\Delta)), \quad (4.51a)$$

$$p_H = (\sqrt{40^2 + m_H^2}, 0, -40, 0), \quad (4.51b)$$

$$p_2 = (40 \cosh(-\Delta), 40, 0, 40 \sinh(-\Delta)). \quad (4.51c)$$

This configuration is useful to check against for two reasons. Firstly, it is a more restrictive limit than the one we considered to derive our amplitude (here, s_{1H} also must be large) and so our calculation should correctly describe this situation too. Secondly, High Energy theory tells us that this process should behave like the $qQ \rightarrow qHQ$ case where the Higgs is produced far from the parton rapidities with a reweighting due to the quark being replaced by a gluon. Figure 4.4 shows both of these points clearly.

Our second phase space parametrisation fixes the Higgs boson to always be close to the gluon in rapidity whilst the two jets move further apart in rapidity.

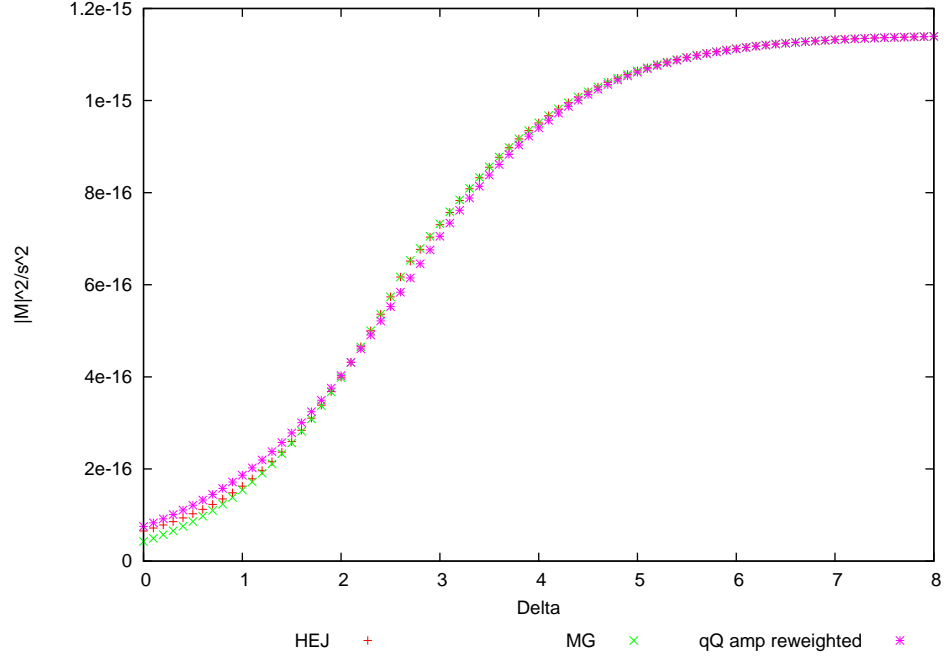


Figure 4.4 *Comparison between the HEJ effective vertex, the full LO result and the result of the $qQ \rightarrow qHQ$ LO calculation reweighted by a colour factor for a central H in $gq \rightarrow Hgq$ with full top mass dependence.*

Explicitly;

$$p_1 = (40\sqrt{2} \cosh(\Delta), -40, 40, 40\sqrt{2} \sinh(\Delta)), \quad (4.52a)$$

$$p_H = (\sqrt{40^2 + m_H^2} \cosh(\Delta + 0.5), 0, -40, \sqrt{40^2 + m_H^2} \sinh(\Delta + 0.5)), \quad (4.52b)$$

$$p_2 = (40 \cosh(-\Delta), 40, 0, 40 \sinh(-\Delta)). \quad (4.52c)$$

In figure 4.5, we plot this new effective vertex approach against the full LO result with this momenta set. We also include the result of the reweighted $qQ \rightarrow qHQ$ amplitude to show that this is not an appropriate result in this limit.

In both cases, we see clear agreement between our result and the full LO result from MadGraph in the high energy limit (high Δ). We now move on to check the effects of having a finite quark mass compared to an infinite one. By simply putting a high value for the top mass in our amplitude (numerically, we see

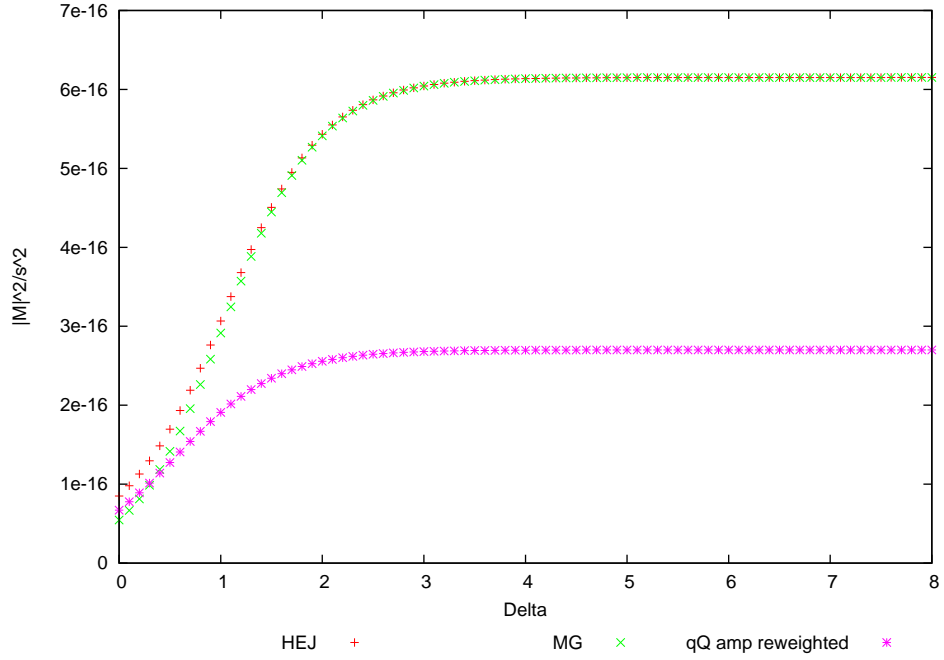


Figure 4.5 *Comparison between the HEJ effective vertex, the full LO result and the result of the $qQ \rightarrow qHQ$ LO calculation reweighted by a colour factor for an outside H in $gq \rightarrow Hgq$ with full top mass dependence.*

that $m_t = 17400$ is a good choice) we can generate results that correspond to the effective theory where the top mass is treated as an infinite parameter. Additionally, we can very easily add the interference via bottom loops to our result (when working out the amplitudes for helicity configurations, simply add the same amplitude with the bottom mass before squaring it) so we can also see how large an effect this has. We will begin by looking at these three cases with a central Higgs (the first set of momenta), which is plotted in figure 4.6. We see that there are clear differences between the cases. The finite top mass case is always greater than the infinite top mass case and the addition of the bottom quark makes it larger still. The same comparison for a Higgs close to the gluon (the second set of momenta) is plotted in figure 4.7. In that case, we have slightly different behaviour - the infinite top mass case is still lower, but now the addition of the bottom loop (slightly) decreases the ME from the case where only the top quark is considered.

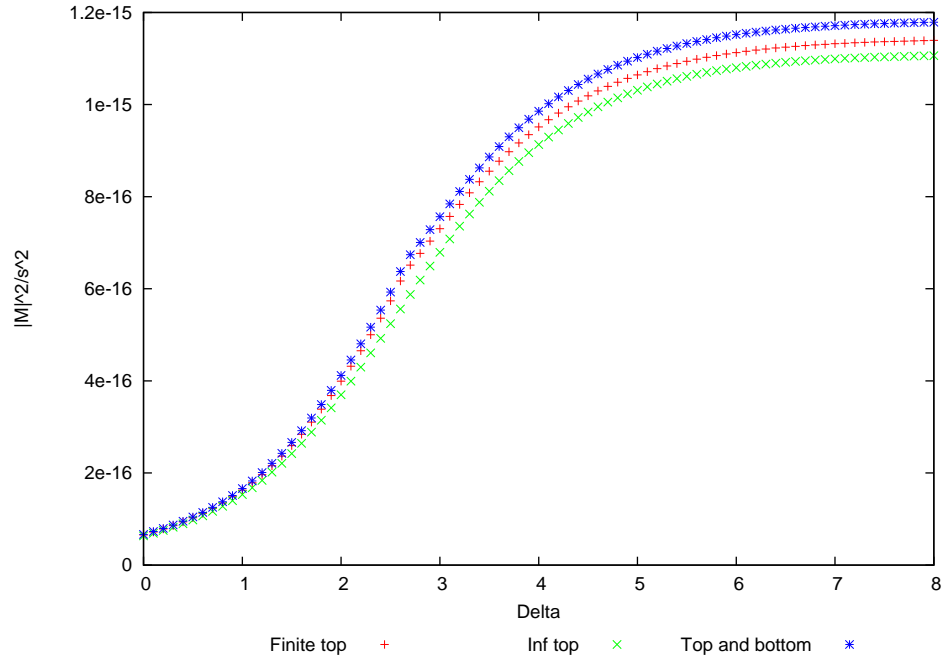


Figure 4.6 *Comparison of infinite top, finite top and finite top plus finite bottom HEJ matrix elements with a central Higgs.*

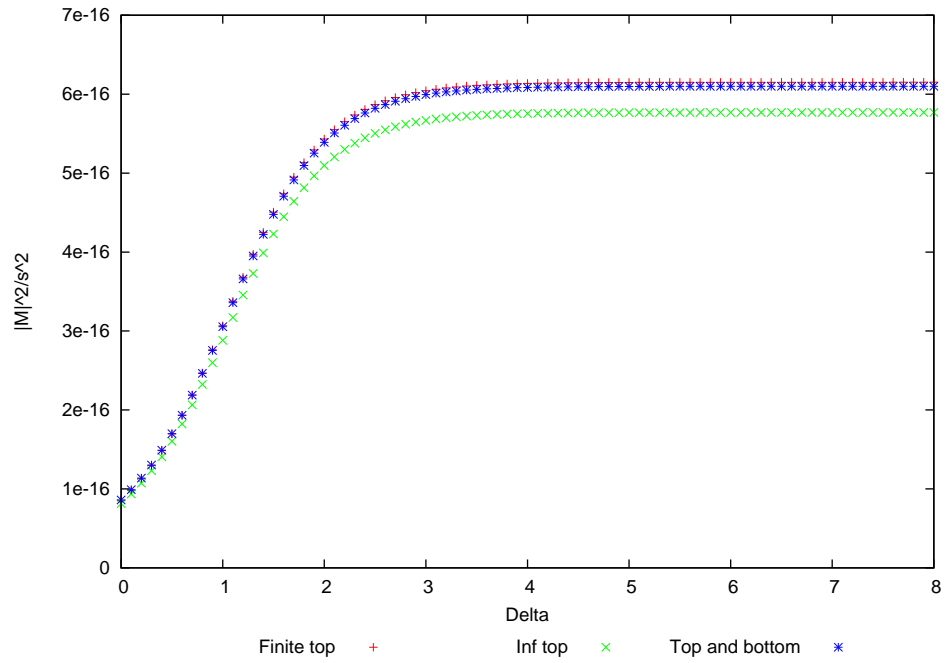


Figure 4.7 *Comparison of infinite top, finite top and finite top plus finite bottom HEJ matrix elements with an outside Higgs.*

The addition of extra emissions is once more done by multiplying Lipatov vertices into the amplitude we have derived. Although some care has to be taken to ensure the correct t-channel momenta are taken, it is relatively straightforward to do this, resulting in a general $gq \rightarrow Hg\dots q$ amplitude (where the ... represent an arbitrary number of gluons) which is simply;

$$|M_{gq \rightarrow Hg\dots q}^{HE, m_t}|^2 = |M_{gq \rightarrow Hgq}^{HE, m_t}|^2 \times \prod_{i=1}^{n-2} \frac{-g_s^2 C_A V^\mu V_\mu}{\hat{t}_i^2}, \quad (4.53)$$

where n is the number of final state jets. As a check, we will generate more explorer plots for the case of one extra emission. We will choose the process $gu \rightarrow Hggu$ with a few different choices for the rapidity of the extra gluon and the Higgs to ensure we are calculating correctly. Our first configuration is used for when the Higgs is being emitted close to the extremal gluon;

$$p_1 = (40 \cosh(\Delta), -40, 0, 40 \sinh(\Delta)), \quad (4.54a)$$

$$p_H = (\sqrt{40^2 + m_H^2} \cosh(\Delta + 0.5), 0, -40, \sqrt{40^2 + m_H^2} \sinh(\Delta + 0.5)), \quad (4.54b)$$

$$p_2 = (40 \cosh(-\Delta/3), 0, 40, 0), \quad (4.54c)$$

$$p_3 = (40 \cosh(-\Delta), 40, 0, 40 \sinh(-\Delta)). \quad (4.54d)$$

We show $|M|^2/\hat{s}^2$ as a function of Δ in figure 4.8 for this configuration. Because the finite m_t result available in MadGraph is numerically unstable at high Δ , we will instead set our m_t to 17400 and compare to the full LO effective theory matrix element, available in earlier versions of MadGraph.

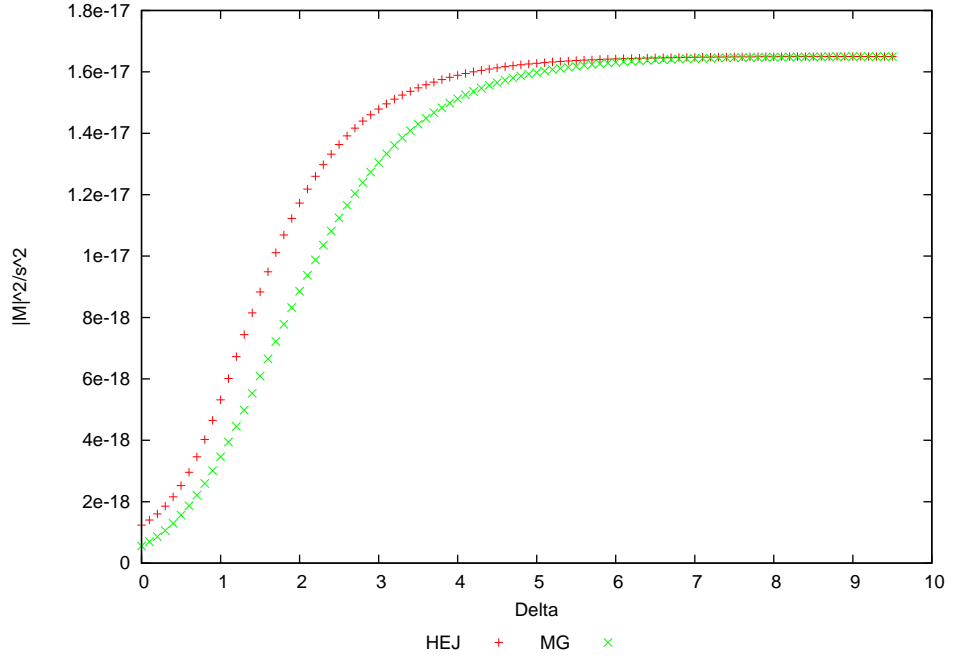


Figure 4.8 *Comparison between the HEJ effective vertex and the full LO result of the $gu \rightarrow Hgg$ amplitude for a forward H with an infinite top mass.*

The agreement here is good across the phase space. Another slice of phase space we can take is one where all particles gradually move apart in rapidity;

$$p_1 = (40 \cosh(\Delta), -40, 0, 40 \sinh(\Delta)), \quad (4.55a)$$

$$p_H = (\sqrt{40^2 + m_H^2} \cosh(\Delta/3), 0, -40, \sqrt{40^2 + m_H^2} \sinh(\Delta/3)), \quad (4.55b)$$

$$p_2 = (40 \cosh(-\Delta/3), 0, 40, 40 \sinh(-\Delta/3)), \quad (4.55c)$$

$$p_3 = (40 \cosh(-\Delta), 40, 0, 40 \sinh(-\Delta)). \quad (4.55d)$$

The explorer plot for this configuration is shown in figure 4.9. Again, the agreement is good between the two lines. The other configuration to check is the one where the Higgs is more behind the extra emission. This contribution is not there for the qg incoming state (at least, not with this matrix element) but is there for gg . In that case, we can send $p_z \rightarrow -p_z$ in p_2 and p_H in our

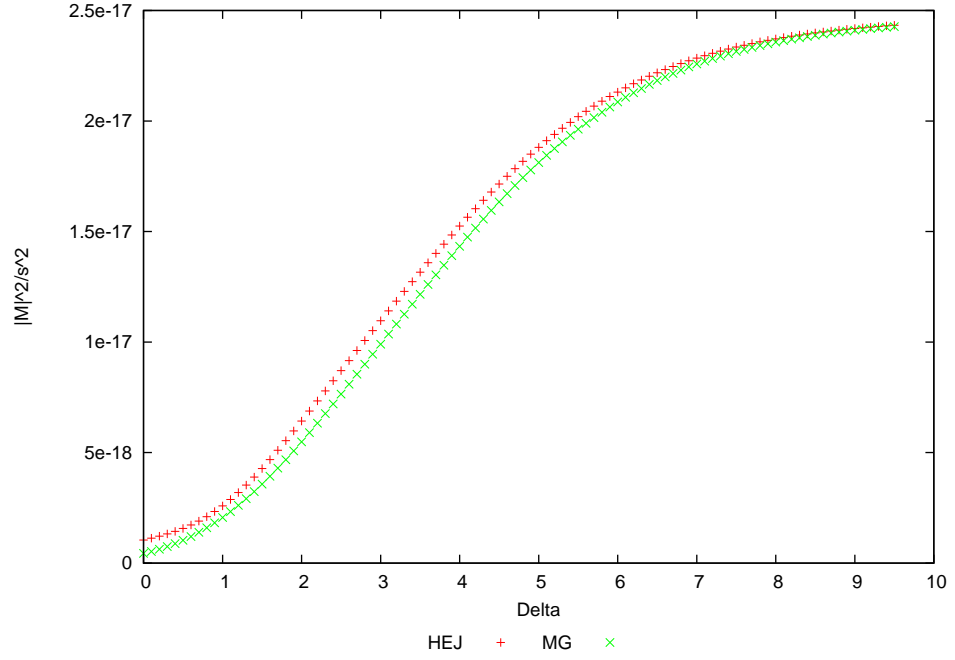


Figure 4.9 *Comparison between the HEJ effective vertex and the full LO result of the $gu \rightarrow gHgu$ amplitude for a central H with an infinite top mass.*

momenta sets to probe this matrix element. In figures 4.10, 4.11, 4.12 and 4.13, we show $gg \rightarrow Hggg$ with the Higgs being more forward, central but more forward than the extra emission, central but more backward than the extra emission and more backward respectively. All plots show agreement in the large Δ region, as expected, and track the LO result fairly well over the entire range. Confident in our forms for the matrix elements, we can move on to implementing them within the HEJ program and investigating their behaviour over the whole range of integrated phase space.

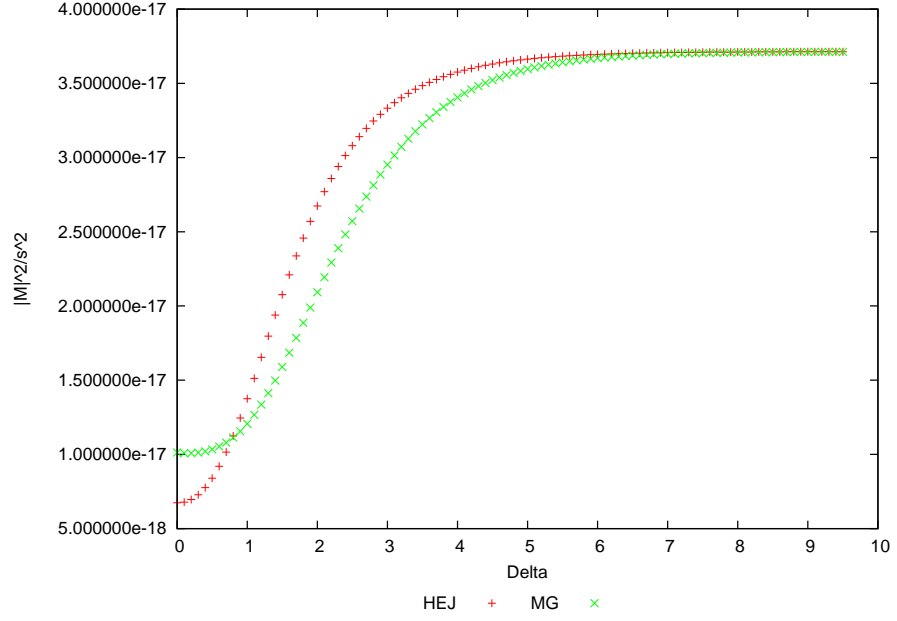


Figure 4.10 Comparison between the HEJ effective vertex and the full LO result of the $gg \rightarrow Hggg$ amplitude for a forward H with an infinite top mass.

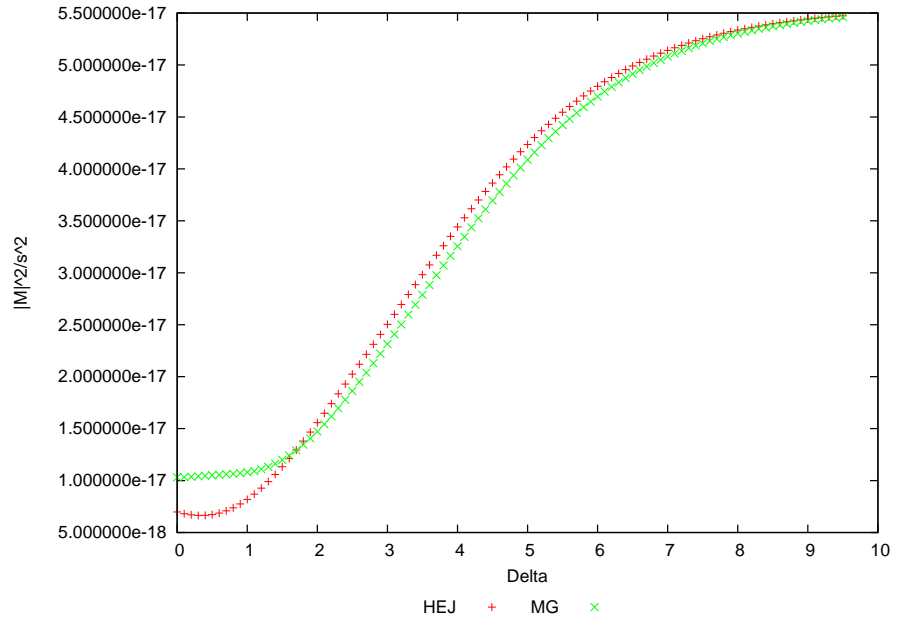


Figure 4.11 Comparison between the HEJ effective vertex and the full LO result of the $gg \rightarrow gHgg$ amplitude for a central H next to the extremal forward parton with an infinite top mass.

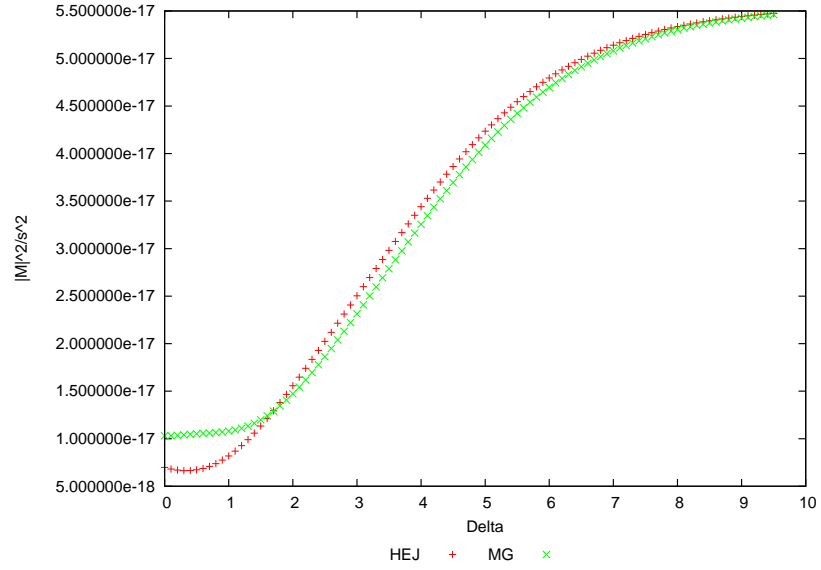


Figure 4.12 *Comparison between the HEJ effective vertex and the full LO result of the $gg \rightarrow ggHg$ amplitude for a central H next to the extremal backward parton with an infinite top mass.*

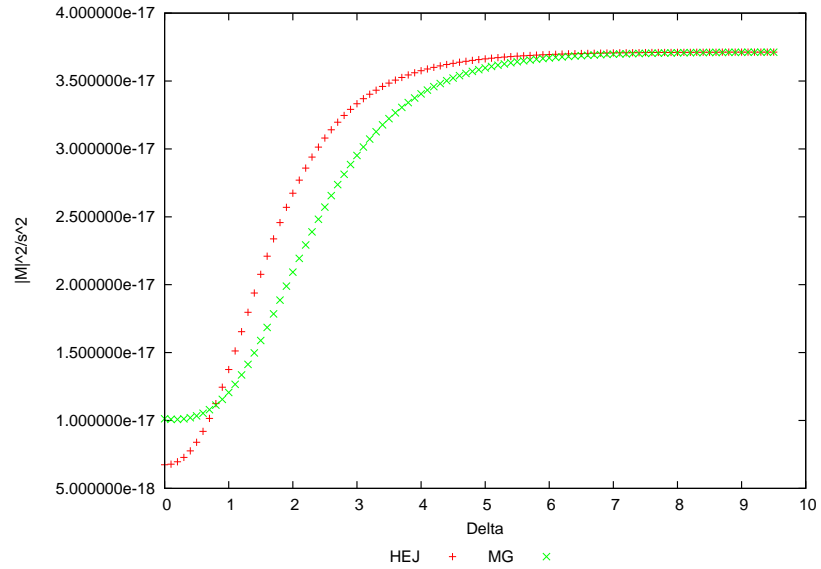


Figure 4.13 *Comparison between the HEJ effective vertex and the full LO result of the $gg \rightarrow gggH$ amplitude for a backward H with an infinite top mass.*

4.3 Computational Aspects

The addition of this new amplitude into the HEJ program is a much simpler task than it was for the NLL processes. Since we already had the amplitude in terms of the impact factors for the infinite top mass cases, the implementation was a case of adding the option to run with this finite top mass element instead. However, in order to calculate the scalar integrals in this amplitude, a HEJ interface to LoopTools is required. This is achieved in the program by setting a special instruction in the makefile; this way, if a user is not interested in using HEJ to generate for these types of events, they do not have to have LoopTools on their system. On the other hand, with the setting of a few library paths and setting the value for the special flag, LoopTools is quickly and simply added to the program such that running these new amplitudes can be done ‘out of the box’.

Another consideration is how to implement the matching for the finite top mass case. It was decided that, given the length of time it would take to evaluate the matrix element with the full top mass included (especially in the three jet case) that it would not be wise to do the matching in this manner. Instead, since the infinite top mass elements are much quicker to evaluate, the matching is done by applying the finite top mass limit to the HEJ amplitude and dividing that by the full LO result in the effective theory. This yields an acceptable compromise, however it would clearly be ideal to match to the full result if the amount of time needed to do so was significantly reduced. This one motivation behind the development of the ‘inverse HEJ’ technique. Since there are many resummation processes that can map to one jet process, the idea is to instead generate the jet level matrix element and work backwards from that to generate many resummation points to evaluate; hence ‘inverse’. This will drastically reduce the amount of calls we would make to the full finite top mass LO element and thus allow us to include this matching.

4.4 Results

Our first analysis will be $gu \rightarrow guH$ run, where the gluon is fixed to be the forward moving particle and the u quark is fixed to be moving backwards. The Higgs can then be more forward than the gluon, more backward than the quark

or in between the two particles in rapidity. For the forward case, we will use the matrix element we just derived to describe the process. For the central case, we will use the reweighted qQ amplitude. Although our new matrix element will get this case correct, the reason we do not use it here is in anticipation of our resummation technique. Because we resum t -channel gluons, it is important to have a system where we can always unambiguously define what those gluons will be (or, in other words, we must have a consistent ‘resummation region’, which for us will be the rapidity space between the gluon and quark). With our new amplitude, we can only resum the gluon connecting the effective vertex to the quark line, but for the reweighted qQ case, we can resum the gluon from the top quark line to the triangle loop in the middle of the diagram and then from the triangle loop down to the bottom quark line. Choosing which matrix element we use based on the rapidity of the Higgs makes it clear which resummation we will be doing. Finally, since we have not discussed the case where the Higgs is behind the outgoing quark, we will set this process to zero for the time being. In the full program, we will use the impact factor already in the program for a Higgs emitted close to a quark line. An interesting plot to look at is the Higgs p_T spectra. The infinite top mass limit should not do well at high values of Higgs p_T as discussed in [24] because it breaks the idea of the top quark mass being the largest relevant scale. This distribution is shown in figure 4.14. We see what we expect; at large Higgs p_T , the results obtained with the effective theory and the theory with finite quark mass effects are very different. Another interesting distribution to look at is the rapidity difference between the gluon and the quark. One could expect that the presence of a large rapidity gap (and so a large dijet invariant mass) might break the infinite top mass limit, but [24] showed this not to be the case. The distribution shown in figure 4.15 agrees with their conclusion.

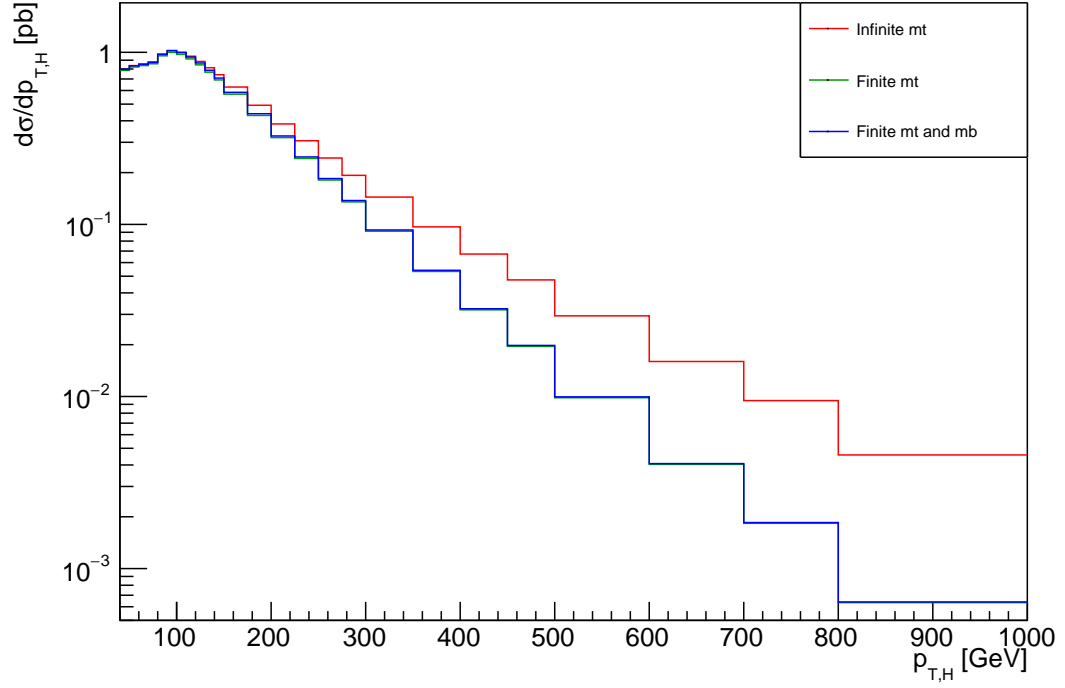


Figure 4.14 *Comparison of infinite top mass, finite top mass and finite top + bottom mass cross sections in $gu \rightarrow guH$, binned in Higgs p_T*

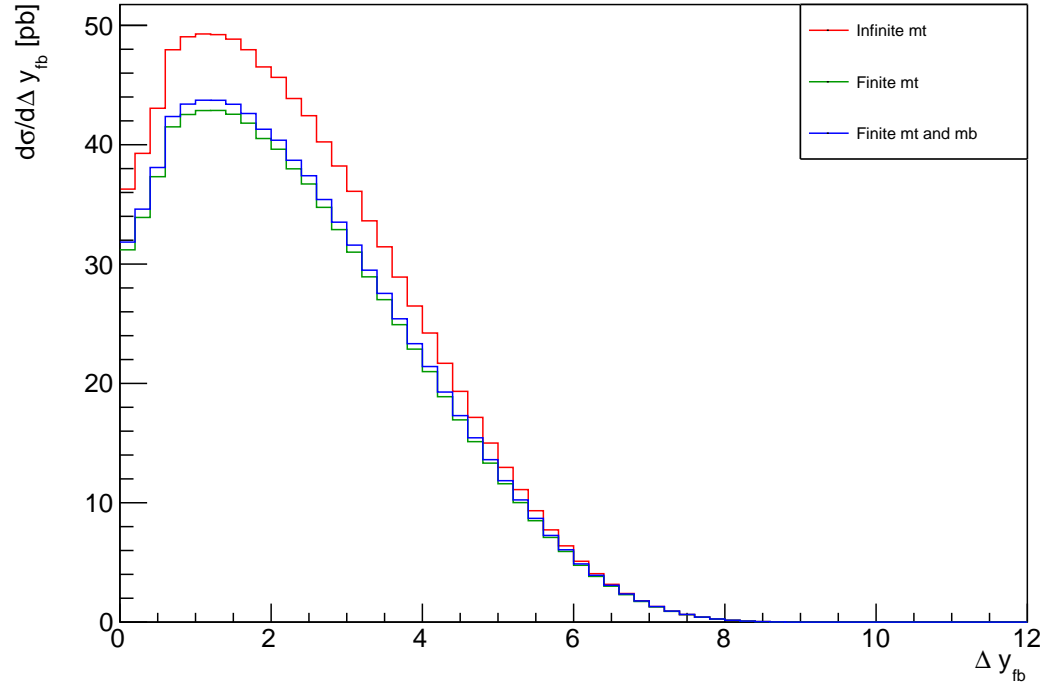


Figure 4.15 *Comparison of infinite top mass, finite top mass and finite top + bottom mass cross sections in $gu \rightarrow guH$, binned in rapidity difference between the gluon and up quark*

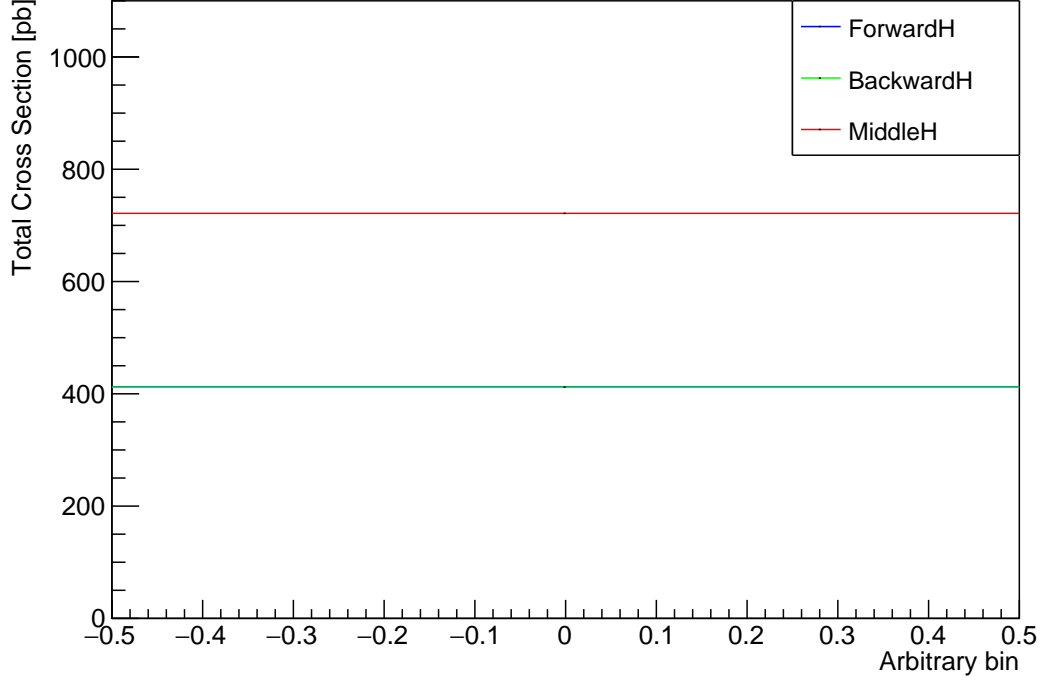


Figure 4.16 *Cross section breakdown in $gg \rightarrow ggH$ into forward Higgs production. backward Higgs production and central Higgs with infinite top mass.*

We should also remember that, given kinematical constraints on the energy of the collider, the high Δ_y region must come with relatively low transverse scales, so it further lends support to the idea that the transverse scales are the defining ones in terms of how well the effective theory does. We can do the same analysis with a gg incoming state, which in the high energy regime is just the qg amplitude reweighted by a colour factor. In this case, the Higgs can be either forward of a forward moving gluon, backward of a backward moving one or in-between. We can describe all of these configurations; the first with our new amplitude, the latter with a reweighted qQ amp and the second with our new matrix element as well so long as we account for phase differences in some calculations we did (all derived results were explicitly considering that the Higgs is emitted forward). If this is considered correctly, then the amount of cross section coming from a forward Higgs should be equal (up to statistical fluctuations) to that coming from a backward Higgs. We show that this is the case in figure 4.16, where the green and blue lines are so close together to be essentially indistinguishable. The results for the Higgs p_T and Δy_{12} distributions are essentially the same as the qg case and we present them here for completeness in figures 4.17 and 4.18.

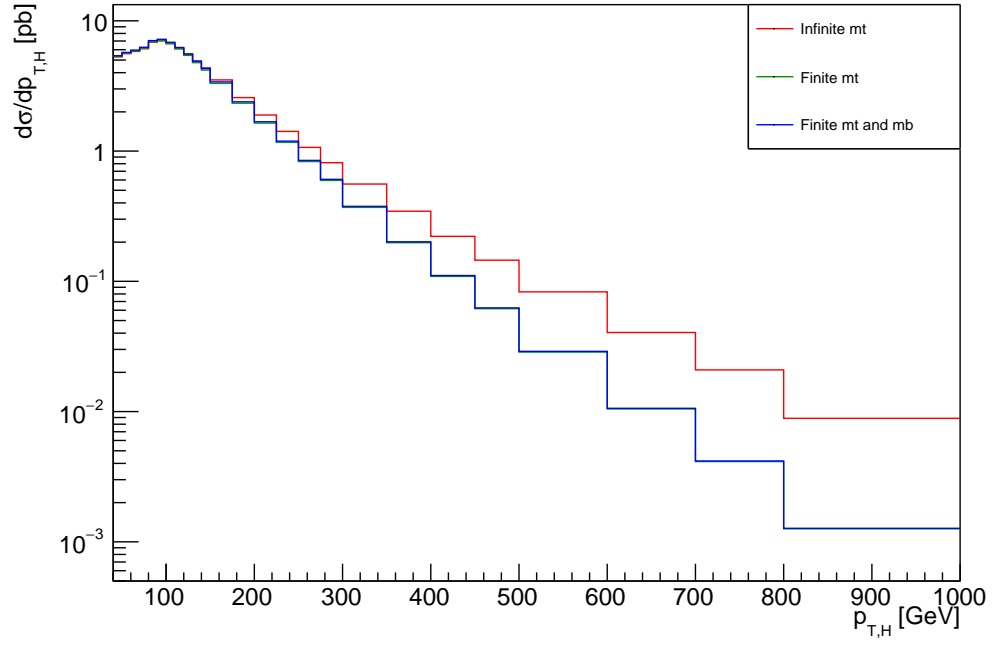


Figure 4.17 *Comparison of infinite top mass, finite top mass and finite top + bottom mass cross sections in $gg \rightarrow ggH$, binned in Higgs p_T .*

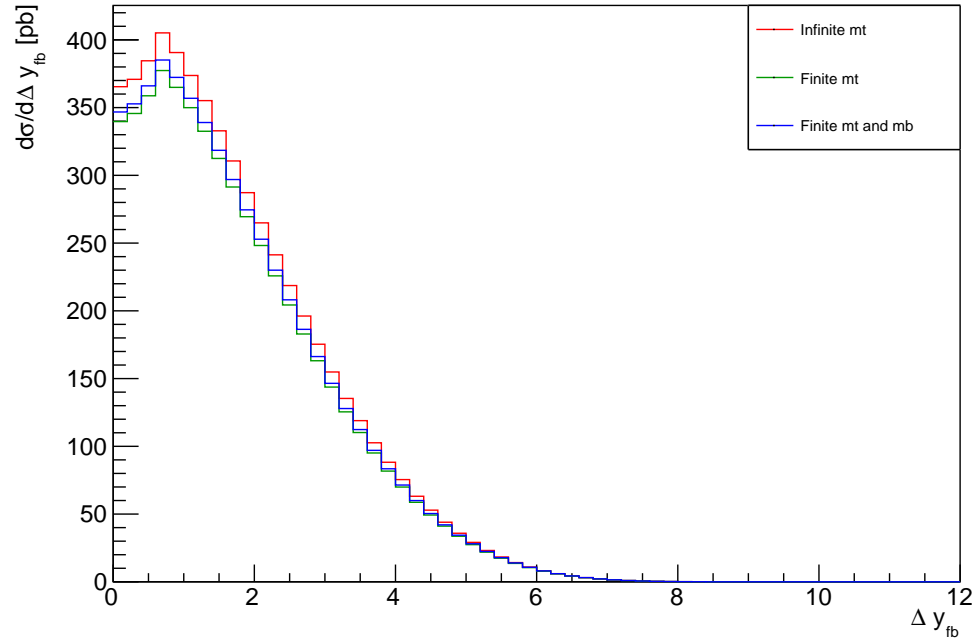


Figure 4.18 *Comparison of infinite top mass, finite top mass and finite top + bottom mass cross sections in $gg \rightarrow ggH$, binned in rapidity difference between the gluon and up quark.*

We also investigate the effect of adding a third jet so as to look at a $gg \rightarrow gggH$ analysis. An interesting plot to show is that again of the Higgs p_T as shown in figure 4.19. We see there is a significant difference between the infinite top mass results and the finite top mass results in all bins - strikingly, at low Higgs p_T . This would seem to contradict our prediction that low transverse scales lead mean that the effective theory is valid. The problem is that, in a three jet event, you can manufacture a situation whereby there is a large hierarchy between the transverse scales that enter the Higgs vertex. If instead we plot the cross section as a function of the largest transverse scale that enters into this vertex, we should then once more again see the agreement in the low p_T end. Figure 4.20 shows this clearly.

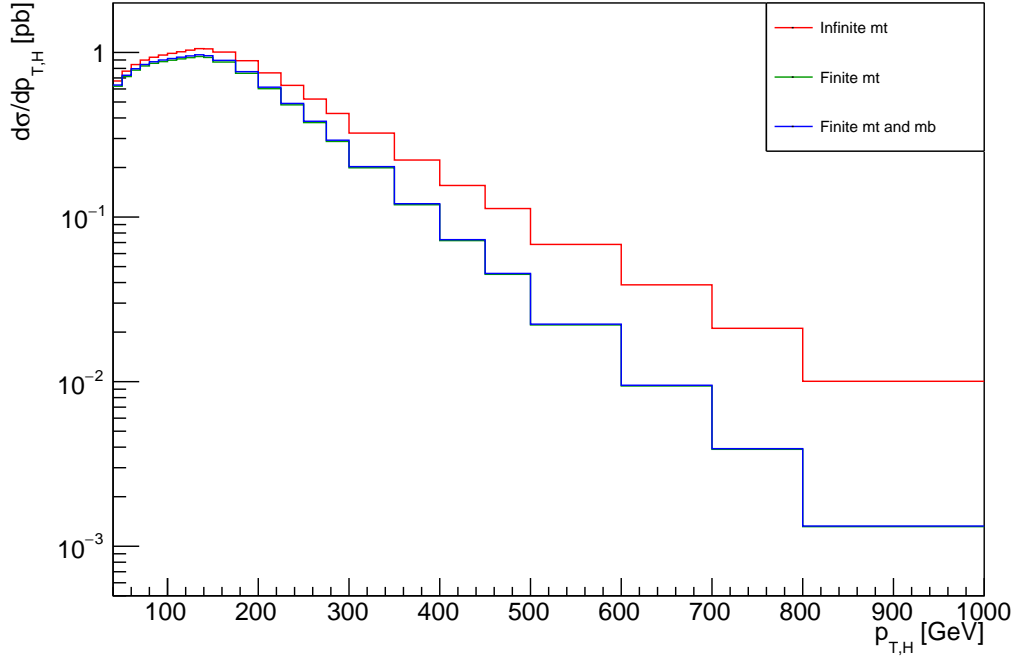


Figure 4.19 *Comparison of infinite top mass, finite top mass and finite top + bottom mass cross sections in $gg \rightarrow gggH$, binned in Higgs p_T .*

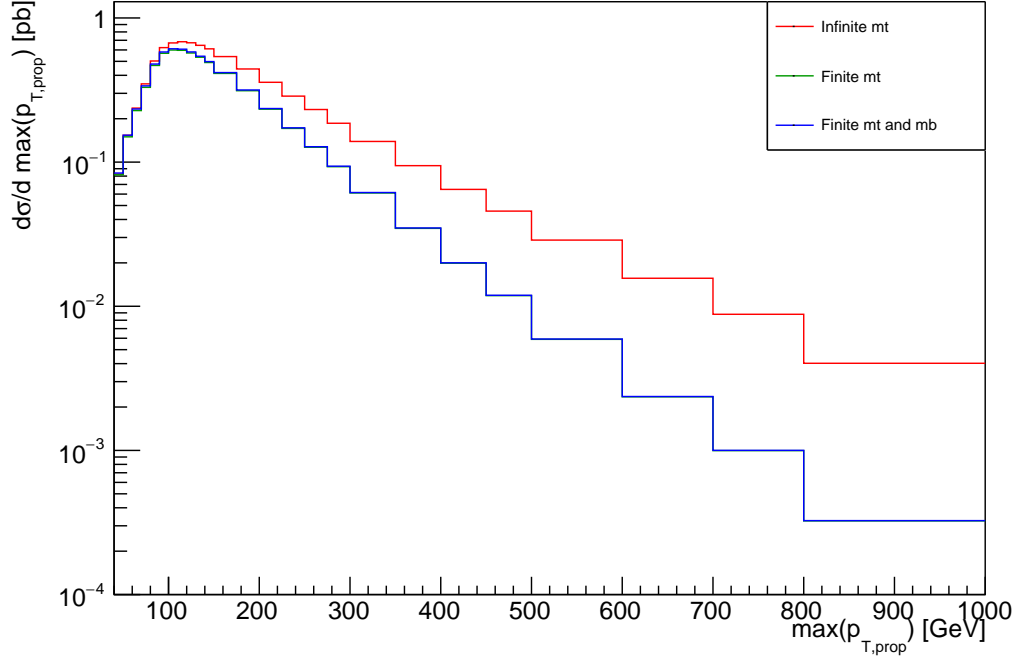


Figure 4.20 *Comparison of infinite top mass, finite top mass and finite top + bottom mass cross sections in $gg \rightarrow gggH$, binned in the maximum p_T of a gluon entering into the Higgs vertex.*

Unfortunately, there has so far not been many analyses of Higgs plus jets physics from the LHC and so we are not able to compare our new predictions against real data. We are, however, now in a prime position to provide predictions for any such data when it arrives. We conclude this section instead with an inclusive Higgs plus dijets prediction and again point out the difference between the full m_t and infinite m_t approaches. The p_T spectra of the Higgs for this case is plotted in figure 4.21, along with the ratio of the finite m_t and finite $m_t + m_b$ lines to the infinite m_t line. We see clearly that the distribution obtained with the effective theory is much different. The same is true if we look at the Δy distribution, shown in figure 4.22.

In all of these distributions, we see that the addition of a bottom loop is having a small overall effect. This would suggest that the Higgs + 1 jet studies of, for example, [40] and [34] where a sizeable difference was seen is an effect of having only one jet accompanying the Higgs.

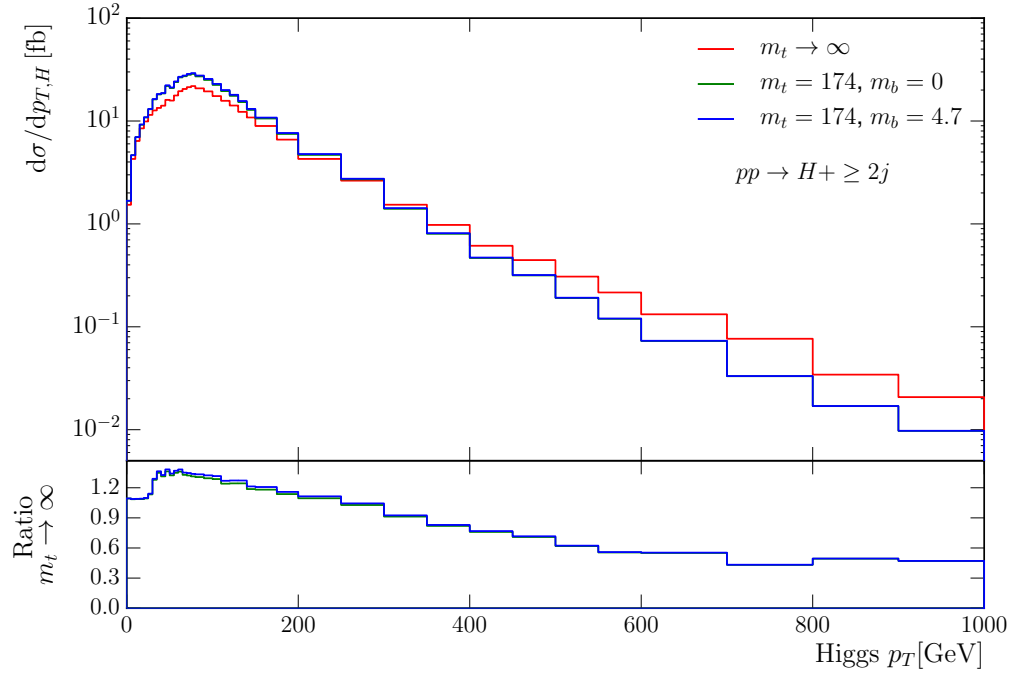


Figure 4.21 Comparison of infinite top mass, finite top mass and finite top + bottom mass cross sections in $pp \rightarrow H + \geq 2j$, binned in the p_T of the Higgs.

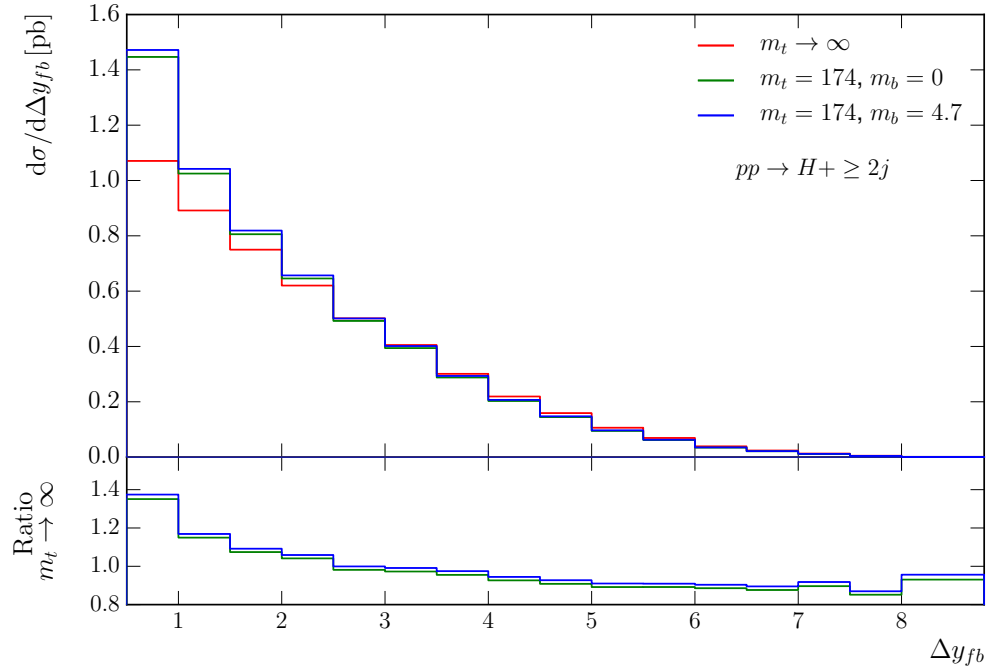


Figure 4.22 Comparison of infinite top mass, finite top mass and finite top + bottom mass cross sections in $pp \rightarrow H + \geq 2j$, binned in the rapidity difference between the most forward/backward jets.

Chapter 5

Conclusions

In this thesis we have studied the perturbative approach to the solution of QCD scattering in the specific context of the Large Hadron Collider and discussed the limitations thereof. In chapter 1, we introduced the base theoretical knowledge needed to understand the technique, which included the discussion of gauge invariance and a general overview of the path integral formulation of Quantum Field Theory. This was used to summarise that calculations could be done by simply following a set of Feynman Rules and we explicitly calculated the $qQ \rightarrow qQ$ amplitude at leading order in α_s using these rules. We saw how this amplitude is converted into the physical cross section which can be measured at the collider and then re-did the calculation with spinor helicity formalism to show how it makes the amplitude calculations neater and quicker.

In chapter 2, we explicitly showed how a truncation in the perturbative series is problematic when high energy particles are involved in the scattering. In particular, it was proved that terms that go like $\alpha_s^n \log^{n-1} \left(\frac{s}{-t} \right)$ appear at higher orders and, given their size, should not be neglected. This naturally led on to the discussion of Regge Theory and the formalism of High Energy Jets in general. The formalism exploits elements of the High Energy Limit in order to write amplitudes as simple current contractions over t -channel poles. By considering real and virtual corrections to processes in that limit, we ended up with a matrix element that can resum the problematic high energy logs to all orders in perturbation theory. In order to be of physical relevance, this matrix element is integrated over the relevant phase space via a Monte Carlo technique and the computational considerations of doing this are discussed. The chapter ends with a selection of

distributions from real LHC analyses, where we show the capture of the high energy logs is already phenomenologically important and will only increase in importance as the centre of mass energy increases.

In chapter 3, we discussed how the formalism can be extended to capture some of the Next-to-Leading Log contributions to jet processes, which will behave like $\alpha_s^n \log^{n-2} \left(\frac{s}{-t} \right)$. The addition of ‘unordered’ gluon emissions allowed us to capture sub-leading contributions from already included partonic channels. The author’s own work focused on the inclusion of matrix elements for entirely new partonic configurations which, although formally sub-leading in the jet process, are leading log in the particular subprocess. As such, the applicability of HEJ was increased and many checks of these new elements are presented along with a discussion of the computational challenges faced in including them within the Monte Carlo program. We concluded the chapter by investigating the effect of the NLL contributions on real data and showed that they provided a significant improvement to our predictions,.

In chapter 4, we introduced how HEJ is also able to describe jet events accompanied by the emission of a Higgs boson. The effective theory where the mass of the top quark is taken to be infinite is discussed and its limitations laid out. The factorisation property that gives HEJ its resummation power does not rely on taking the infinite top mass limit and so amplitudes with full quark mass dependence were derived within the formalism. As a result, HEJ is unique in its ability to provide a prediction for such processes with both a high energy resummation and finite quark mass effects taken into account. By the presentation of a set of distributions, we saw how the effect of finite quark mass loops can lead to significantly different results; most drastically, in the behaviour of tails of the Higgs transverse momentum.

In conclusion, the effects of large logarithmic contributions on QCD amplitudes are seen to be large and we must take them seriously in order to provide accurate Standard Model predictions. As the energy of colliders increase, these effects will only become more significant. It is therefore in the interests of both the HEJ collaboration and the phonological community in general to ensure an accurate inclusion of them. For HEJ, one aspect of this is to include some sub-leading partonic configurations in the resummation, since this reduces our dependence on leading order matching techniques. It remains a long term goal

of the collaboration to include next-to-leading order matrix elements in the matching routine but the process is complicated by ensuring that no ‘double counting’ occurs. Furthermore, the contributions of collinear terms are necessarily ignored by the approximations that underlie HEJ but must be considered for a complete description. This is currently done via an interface to the parton shower ARIADNE and there are plans to extend this to use the state-of-the-art parton shower of Pythia [43]. As well as the discussion of pure jet final states, HEJ also provides predictions for final states involving an electroweak boson. We now have the capability to move away from the currently implemented infinite top mass limit when discussing the emission of a Higgs boson. In order to detect any deviations in the discovered Higgs boson from the Standard Model predictions, it is vitally important that all known effects are correctly accounted for and this new capability of HEJ will help to a great degree towards that goal.

Appendix A

Form of the H Functions in the $gq \rightarrow Hgq$ Box Integral

In the $gq \rightarrow Hgq$ amplitude with full finite quark masses included, the box integral in the gauge where the gluon polarisation vectors are orthogonal to both the incoming and the outgoing gluon momenta can be parametrised as;

$$M^{\mu\nu\rho} = \frac{g_s^3 m_t^2}{v} 2i f^{bac} J^{\mu\nu\rho}, \quad (\text{A.1})$$

with;

$$J^{\mu\nu\rho} = \eta^{\mu\nu}(H_1 k_1^\rho + H_2 k_2^\rho) + \eta^{\mu\rho} H_4 k^\nu + \eta^{\nu\rho} H_5 k^\mu + H_{10} k_2^\rho k^\mu k^\nu + H_{12} k_1^\rho k^\mu k^\nu, \quad (\text{A.2})$$

with the convention that all the k s are taken as outgoing. We have that k_1^μ and k_2^μ are the momenta corresponding to the on-shell gluons with colour indices a, b and $k = -k_1 - k_2 - k_H$ with colour index c . Not all of the H functions above are independent, though;

$$\begin{aligned} H_2 &= -H_1(k_1 \leftrightarrow k_2) \\ H_5 &= -H_4(k_1 \leftrightarrow k_2) \\ H_{12} &= -H_{10}(k_1 \leftrightarrow k_2). \end{aligned} \quad (\text{A.3})$$

We will therefore only give the forms for H_1, H_4 and H_{10} . Since there are three distinct orderings for the box diagram, we present this in the form $H_i = E_i + F_i + G_i$, where each term is a function of the scalar integrals;

$$\begin{aligned}
B_0(k) &= \int \frac{d^4q}{(2\pi)^4} \frac{1}{(q^2 - m_t^2)((q+k)^2 - m_t^2)}, \\
C_0(p, k) &= \int \frac{d^4q}{(2\pi)^4} \frac{1}{(q^2 - m_t^2)((q+p)^2 - m_t^2)((q+p+k)^2 - m_t^2)}, \\
D_0(p, k, v) &= \int \frac{d^4q}{(2\pi)^4} \left[\frac{1}{(q^2 - m_t^2)((q+p)^2 - m_t^2)((q+p+k)^2 - m_t^2)} \right. \\
&\quad \left. \times \frac{1}{((q+p+k+v)^2 - m_t^2)} \right].
\end{aligned} \tag{A.4}$$

The B_0 integral is divergent in four dimensions but will always appear in combinations such that the divergence is cancelled. We will also define;

$$\begin{aligned}
s_{ij} &= (k_i + k_j)^2, \\
S_i &= 2k_i \cdot k, \\
\Delta &= s_{12}s_{34} - S_1S_2, \\
\Sigma &= 4s_{12}s_{34} - (S_1 + S_2)^2.
\end{aligned} \tag{A.5}$$

In terms of these variables, we obtain;

$$\begin{aligned}
E_1 = & -s_{12}D_0(2, 1, 34) \left[1 - \frac{8m_t^2}{s_{12}} + \frac{S_2}{2s_{12}} + \frac{S_2(s_{12} - 8m_t^2)(s_{34} + S_1)}{2s_{12}\Delta} \right. \\
& \left. + \frac{2(s_{34} + S_1)^2}{\Delta} + \frac{S_2(s_{34} + S_1)^3}{\Delta^2} \right] \\
& - [(s_{12} + S_2)C_0(2, 134) - s_{12} + (S_1 - S_2)C_0(12, 34) - S_1C_0(1, 34)] \\
& \times \left(\frac{S_2(s_{12} - 4m_t^2)}{2s_{12}\Delta} + \frac{2(s_{34} + S_1)}{\Delta} + \frac{S_2(s_{34} + S_1)^2}{\Delta^2} \right) \\
& + [C_0(1, 34) - C_0(12, 34)] \left(1 - \frac{4m_t^2}{s_{12}} \right) - C_0(12, 34) \frac{2s_{34}}{S_1} \\
& - [B_0(134) - B_0(1234)] \frac{2s_{34}(s_{34} + S_1)}{S_1\Delta} \\
& + [B_0(34) - B_0(1234) + s_{12}C_0(12, 34)] \left(\frac{2s_{34}(s_{34} + S_1)(S_1 - S_2)}{\Delta\Sigma} + \frac{2s_{34}(s_{34} + S_1)}{S_1\Delta} \right) \\
& + [B_0(12) - B_0(1234) - (s_{34} + S_1 + S_2)C_0(12, 34)] \frac{2(s_{34} + S_1)(2s_{12}s_{34} - S_2(S_1 + S_2))}{\Delta\Sigma},
\end{aligned} \tag{A.6a}$$

$$\begin{aligned}
F_1 = & -S_2D_0(1, 2, 34) \left[\frac{1}{2} - \frac{(s_{12} - 8m_t^2)(s_{34} + S_2)}{2\Delta} \right] - \frac{s_{12}(s_{34} + S_2)^3}{\Delta^2} \\
& + [(s_{12} + S_1)C_0(1, 234) - s_{12}C_0(1, 2) - (S_1 - S_2)C_0(12, 34) - S_2C_0(2, 34)] \\
& \times \left(\frac{S_2(s_{12} - 4m_t^2)}{2s_{12}\Delta} + \frac{S_2(s_{34} + S_2)^2}{\Delta^2} \right) \\
& - [C_0(12, 34) - C_0(1, 234)] \left(1 - \frac{4m_t^2}{s_{12}} \right) - C_0(1, 234) \\
& + [B_0(234) - B_0(1234)] \frac{2(s_{34} + S_2)^2}{(s_{12} + S_1)\Delta} \\
& - [B_0(34) - B_0(1234) + s_{12}C_0(12, 34)] \frac{2s_{34}(s_{34} + S_2)(S_2 - S_1)}{\Delta\Sigma} \\
& + [B_0(12) - B_0(1234) - (s_{34} + S_1 + S_2)C_0(12, 34)] \frac{2(s_{34} + S_2)(2s_{12}s_{34} - S_2(S_1 + S_2))}{\Delta\Sigma},
\end{aligned} \tag{A.6b}$$

$$\begin{aligned}
G_1 = & S_2 D_0(1, 34, 2) \left[\frac{\Delta}{s_{12}^2} - \frac{4m_t^2}{s_{12}} \right] \\
& - S_2 [(s_{12} + S_1)C_0(1, 234) - S_1 C_0(1, 34)] \left(\frac{1}{s_{12}^2} - \frac{s_{12} - 4m_t^2}{2s_{12}\Delta} \right) \\
& - S_2 [(s_{12} + S_2)C_0(13, 2) - S_2 C_0(2, 34)] \left(\frac{1}{s_{12}^2} + \frac{s_{12} - 4m_t^2}{2s_{12}\Delta} \right) \\
& - C_0(1, 34) - [C_0(1, 234) - C_0(1, 34)] \frac{4m_t^2}{s_{12}} + [B_0(134) - B_0(1234)] \frac{2}{s_{12}} \\
& + [B_0(134) - B_0(34)] \frac{2s_{34}}{s_{12}S_1} + [B_0(234) - B_0(1234)] \frac{2(s_{34} + S_2)}{s_{12}(s_{12} + S_1)},
\end{aligned} \tag{A.6c}$$

$$\begin{aligned}
E_4 = & -s_{12} D_0(2, 1, 34) \left[\frac{1}{2} - \frac{(S_1 - 8m_t^2)(s_{34} + S_1)}{2\Delta} - \frac{s_{12}(s_{34} + S_1)^3}{\Delta^3} \right] \\
& + [(s_{12} + S_2)C_0(2, 134) - s_{12}C_0(1, 2) + (S_1 - S_2)C_0(12, 34) - S_1 C_0(1, 34)] \\
& \times \left(\frac{(S_1 - 4m_t^2)}{2\Delta} + \frac{s_{12}(s_{34} + S_1)^2}{\Delta^2} \right) \\
& - C_0(12, 34) + [B_0(134) - B_0(1234)] \left(\frac{2s_{34}}{\Delta} + \frac{2s_{12}(s_{34} + S_1)}{(s_{12} + S_2)\Delta} \right) \\
& - [B_0(34) - B_0(1234) + s_{12}C_0(12, 34)] \left(\frac{2s_{34}(2s_{12}s_{34} - S_2(S_1 + S_2) + s_{12}(S_1 - S_2))}{\Delta\Sigma} \right) \\
& + [B_0(12) - B_0(1234) - (s_{34} + S_1 + S_2)C_0(12, 34)] \\
& \times \left(\frac{2s_{12}(2s_{12}s_{34} - S_1(S_1 + S_2) + s_{34}(S_2 - S_1))}{\Delta\Sigma} \right),
\end{aligned} \tag{A.6d}$$

$$\begin{aligned}
F_4 = & -s_{12}D_0(1, 2, 34) \left[\frac{1}{2} + \frac{(S_1 - 8m_t^2)(s_{34} + S_2)}{2\Delta} + \frac{s_{12}(s_{34} + S_2)^3}{\Delta^3} \right] \\
& - [(s_{12} + S_1)C_0(1, 234) - s_{12}C_0(1, 2) - (S_1 - S_2)C_0(12, 34) - S_2C_0(2, 34)] \\
& \times \left(\frac{S_1 - 4m_t^2}{2\Delta} + \frac{s_{12}(s_{34} + S_2)^2}{\Delta^2} \right) \\
& - C_0(12, 34) - [B_0(234) - B_0(1234)] \frac{2(s_{34} + S_2)}{\Delta} \\
& + [B_0(34) - B_0(1234) + s_{12}C_0(12, 34)] \frac{2s_{34}(2s_{12}s_{34} - S_1(S_1 + S_2) + s_{12}(S_2 - S_1))}{\Delta\Sigma} \\
& - [B_0(12) - B_0(1234) - (s_{34} + S_1 + S_2)C_0(12, 34)] \\
& \times \left(\frac{2s_{12}(2s_{12}s_{34} - S_2(S_1 + S_2) + s_{34}(S_1 - S_2))}{\Delta\Sigma} \right),
\end{aligned} \tag{A.6e}$$

$$\begin{aligned}
G_4 = & -D_0(1, 34, 2) \left[\frac{\Delta}{s_{12}} + \frac{s_{12} + S_1}{2} - 4m_t^2 \right] \\
& + [(s_{12} + S_1)C_0(1, 234) - S_1C_0(1, 34)] \left(\frac{1}{s_{12}} - \frac{S_1 - 4m_t^2}{2\Delta} \right) \\
& + [(s_{12} + S_2)C_0(134, 2) - S_2C_0(2, 34)] \left(\frac{1}{s_{12}} + \frac{S_1 - 4m_t^2}{2\Delta} \right) \\
& + [B_0(1234) - B_0(134)] \frac{2}{s_{12} + S_2},
\end{aligned} \tag{A.6f}$$

$$\begin{aligned}
E_{10} = & -s_{12}D_0(2, 1, 34) \left[\frac{s_{34} + S_1}{\Delta} + \frac{12m_t^2 S_1(s_{34} + S_1)}{\Delta^2} - \frac{4s_{12}S_1(s_{34} + S_1)^3}{\Delta^3} \right] \\
& - [(s_{12} + S_2)C_0(2, 134) - s_{12}C_0(1, 2) + (S_1 - S_2)C_0(12, 34) - S_1C_0(1, 34)] \\
& \times \left(\frac{1}{\Delta} + \frac{4m_t^2 S_1}{\Delta^2} - \frac{4s_{12}S_1(s_{34} + S_1)^2}{\Delta^3} \right) \\
& + C_0(12, 34) \left(\frac{4s_{12}s_{34}(S_1 - S_2)}{\Delta\Sigma} - \frac{4(s_{12} - 2m_t^2)(2s_{12}s_{34} - S_1(S_1 + S_2))}{\Delta\Sigma} \right) \\
& + [B_0(134) - B_0(1234)] \left(\frac{4(s_{34} + S_1)}{(s_{12} + S_2)\Delta} + \frac{8S_1(s_{34} + S_1)}{\Delta^2} \right) \\
& + [B_0(34) - B_0(1234) + s_{12}C_0(12, 34)] \left(\frac{12s_{34}(2s_{12} + S_1 + S_2)(2s_{12}s_{34} - S_1(S_1 + S_2))}{\Delta\Sigma^2} \right. \\
& \left. - \frac{4s_{34}(4s_{12} + 3S_1 + S_2)}{\Delta\Sigma} + \frac{8s_{12}s_{34}(s_{34}(s_{12} + S_2) - S_1(s_{34} + S_1))}{\Delta^2\Sigma} \right) \\
& + [B_0(12) - B_0(1234) - (s_{34} + S_1 + S_2)C_0(12, 34)] \\
& \times \left(\frac{12s_{12}(2s_{34} + S_1 + S_2)(2s_{12}s_{34} - S_1(S_1 + S_2))}{\Delta\Sigma^2} \right. \\
& \left. + \frac{8s_{12}S_1(s_{34}(s_{12} + S_2) - S_1(s_{34} + S_1))}{\Delta^2\Sigma} \right) \\
& + \frac{i}{4\pi^2} \left(\frac{2s_{12}s_{34} - S_1(S_1 + S_2)}{\Delta\Sigma} \right),
\end{aligned}
\tag{A.6g}$$

$$\begin{aligned}
F_{10} = & s_{12}D_0(1, 2, 34) \left[\frac{s_{34} + S_2}{\Delta} - \frac{4m_t^2}{\Delta} + \frac{12m_t^2 s_{34}(s_{12} + S_1)}{\Delta^2} \right. \\
& \left. - \frac{4s_{12}(s_{34} + S_2)^2}{\Delta^2} - \frac{4s_{12}S_1(s_{34} + S_2)^3}{\Delta^3} \right] \\
& + [(s_{12} + S_1)C_0(1, 234) - s_{12}C_0(1, 2) - (S_1 - S_2)C_0(12, 34) - S_2C_0(2, 34)] \\
& \times \left(\frac{1}{\Delta} + \frac{4m_t^2 S_1}{\Delta^2} - \frac{4s_{12}(s_{34} + S_2)}{\Delta^2} - \frac{4s_{12}S_1(s_{34} + S_1)^2}{\Delta^3} \right) \\
& - C_0(12, 34) \left(\frac{4s_{12}s_{34}}{S_2\Delta} + \frac{4s_{12}s_{34}(S_2 - S_1)}{\Delta\Sigma} + \frac{4(s_{12} - 2m_t^2)(2s_{12}s_{34} - S_1(S_2 + S_2))}{\Delta\Sigma} \right) \\
& - [B_0(234) - B_0(1234)] \left(\frac{4s_{34}}{S_2\Delta} + \frac{8s_{34}(s_{12} + S_1)}{\Delta^2} \right) \\
& - [B_0(34) - B_0(1234) + s_{12}C_0(12, 34)] \left(-\frac{12s_{34}(2s_{12} + S_1 + S_2)(2s_{12}s_{34} - S_1(S_1 + S_2))}{\Delta\Sigma^2} \right) \\
& - \frac{4s_{12}s_{34}^2}{S_2\Delta^2} + \frac{4s_{34}S_1}{\Delta\Sigma} - \frac{4s_{34}(s_{12}s_{34}(2s_{12} + S_2) - S_1^2(2s_{12} + S_1))}{\Delta^2\Sigma} \\
& - [B_0(12) - B_0(1234) - (s_{34} + S_1 + S_2)C_0(12, 34)] \\
& \left(-\frac{12s_{12}(2s_{34} + S_1 + S_2)(2s_{12}s_{34} - S_1(S_1 + S_2))}{\Delta\Sigma^2} + \frac{8s_{12}(2s_{34} + S_1)}{\Delta\Sigma} \right. \\
& \left. - \frac{8s_{12}s_{34}(2s_{12}s_{34} - S_1(S_1 + S_2) + s_{12}(S_2 - S_1))}{\Delta^2\Sigma} \right) \\
& + \left(\frac{i}{4\pi^2} \right) \left(\frac{2s_{12}s_{34} - S_1(S_1 + S_2)}{\Delta\Sigma} \right),
\end{aligned} \tag{A.6h}$$

$$\begin{aligned}
G_{10} = & -D_0(1, 34, 2) \left(1 + \frac{4S_1m_t^2}{\Delta} \right) \\
& + [(s_{12} + S_1)C_0(1, 234) - S_1C_0(1, 34)] \left(\frac{1}{\Delta} + \frac{4S_1m_t^2}{\Delta^2} \right) \\
& - [(s_{12} + S_2)C_0(134, 2) - S_2C_0(2, 34)] \left(\frac{1}{\Delta} + \frac{4S_1m_t^2}{\Delta^2} \right) \\
& + [B_0(1234) - B_0(134)] \frac{4(s_{34} + S_1)}{\Delta(s_{12} + S_2)} + [B_0(34) - B_0(234)] \frac{4s_{34}}{\Delta S_2},
\end{aligned} \tag{A.6i}$$

where we have used the notation ij to mean $k_i + k_j$ in writing out the scalar integral arguments.

Bibliography

- [1] ALWALL, J., HERQUET, M., MALTONI, F., MATTELAER, O., AND STELZER, T. MadGraph 5: Going Beyond. *Journal of High Energy Physics* 2011, 6 (jun 2011), 128.
- [2] ANDERSEN, J. R., HAPOLA, T., AND SMILLIE, J. M. W plus multiple jets at the LHC with high energy jets. *Journal of High Energy Physics* 2012, 9 (sep 2012), 47.
- [3] ANDERSEN, J. R., LÖNNBLAD, L., AND SMILLIE, J. M. A parton shower for High Energy Jets. *Journal of High Energy Physics* 2011, 7 (jul 2011), 110.
- [4] ANDERSEN, J. R., MEDLEY, J. J., AND SMILLIE, J. M. Z/ γ plus multiple hard jets in high energy collisions. *Journal of High Energy Physics* 2016, 5 (may 2016), 136.
- [5] ANDERSEN, J. R., AND SMILLIE, J. M. The Factorisation of the t-channel Pole in Quark-Gluon Scattering. *Physical Review D* (oct 2009), 10.
- [6] ANDERSEN, J. R., AND SMILLIE, J. M. Constructing all-order corrections to multi-jet rates. *Journal of High Energy Physics* 2010, 1 (jan 2010), 39.
- [7] ANDERSEN, J. R., AND SMILLIE, J. M. Multiple jets at the LHC with high energy jets. *Journal of High Energy Physics* 2011, 6 (jun 2011), 10.
- [8] AOYAMA, T., HAYAKAWA, M., KINOSHITA, T., AND NIO, M. Tenth-order QED contribution to the electron g-2 and an improved value of the fine structure constant. *Physical review letters* 109, 11 (sep 2012), 111807.
- [9] ATLAS. Measurement of dijet production with a veto on additional central jet activity in pp collisions at $\sqrt{s} = 7$ TeV using the ATLAS detector. *Journal of High Energy Physics* 2011, 9 (sep 2011), 53.
- [10] ATLAS. Observation of a new particle in the search for the Standard Model Higgs boson with the ATLAS detector at the LHC. *Physics Letters B* 716, 1 (sep 2012), 1–29.
- [11] ATLAS. Measurements of jet vetoes and azimuthal decorrelations in dijet events produced in pp collisions at $\sqrt{s}=7\text{TeV}$ using the ATLAS detector.

- The European physical journal. C, Particles and fields* 74, 11 (jan 2014), 3117.
- [12] ATLAS. Measurements of the W production cross sections in association with jets with the ATLAS detector. *The European physical journal. C, Particles and fields* 75, 2 (jan 2014), 82.
 - [13] ATLAS. Measurement of four-jet differential cross sections in $s = 8 \sqrt{s}=8$ TeV proton-proton collisions using the ATLAS detector. *Journal of High Energy Physics* 2015, 12 (dec 2015), 105.
 - [14] BERTONE, G., HOOPER, D., AND SILK, J. Particle dark matter: evidence, candidates and constraints. *Physics Reports* 405, 5 (2005), 279–390.
 - [15] BOGDAN, A., AND FADIN, V. A proof of the reggeized form of amplitudes with quark exchanges. *Nuclear Physics B* 740, 1-2 (apr 2006), 36–57.
 - [16] BUCKLEY, A., FERRANDO, J., LLOYD, S., NORDSTROM, K., PAGE, B., RUEFENACHT, M., SCHOENHERR, M., AND WATT, G. LHAPDF6: parton density access in the LHC precision era.
 - [17] CACCIARI, M., SALAM, G. P., AND SOYEZ, G. FastJet user manual. *The European Physical Journal C* 72, 3 (mar 2012), 1896.
 - [18] CMS. Measurement of the inclusive production cross sections for forward jets and for dijet events with one forward and one central jet in pp collisions at $\sqrt{s} = 7$ TeV. *Journal of High Energy Physics* 2012, 6 (jun 2012), 36.
 - [19] CMS. Ratios of dijet production cross sections as a function of the absolute difference in rapidity between jets in protonproton collisions at $\sqrt{s} = 7$ TeV. *The European Physical Journal C* 72, 11 (nov 2012), 2216.
 - [20] CUTKOSKY, R. E. Singularities and Discontinuities of Feynman Amplitudes Singularities and Discontinuities of Feynman Amplitudes. *Journal of Mathematical Physics J. Math. Phys. J. Math. Phys. J. Math. Phys. Mass Singularities of Feynman Amplitudes J. Math. Phys* 1, 10 (sep 1960), 429–1833.
 - [21] D0. Studies of W boson plus jets production in pp collisions at $\sqrt{s}=1.96$ TeV. *Physical Review D* 88, 9 (nov 2013), 092001.
 - [22] DEL DUCA, V. Equivalence of the Parke-Taylor and the Fadin-Kuraev-Lipatov amplitudes in the high-energy limit. *Physical Review D* 52, 3 (aug 1995), 1527–1534.
 - [23] DEL DUCA, V., KILGORE, W., OLEARI, C., SCHMIDT, C., AND ZEPPEFELD, D. Gluon-fusion contributions to H+2 jet production. *Nuclear Physics B* 616, 1-2 (nov 2001), 367–399.

- [24] DEL DUCA, V., KILGORE, W., OLEARI, C., SCHMIDT, C., AND ZEPPENFELD, D. Kinematical limits on Higgs boson production via gluon fusion in association with jets. *Physical Review D* 67, 7 (apr 2003), 073003.
- [25] DIRAC, P. A. *The Principles of Quantum Mechanics*. No. 4. Birkhäuser-Verlag, dec 1958.
- [26] DIXON, L. Calculating Scattering Amplitudes Efficiently. *arXiv preprint hep-ph/9601359*, Tasi 95 (jan 1996), 45.
- [27] ELLIS, J. Testing the Standard Model and Beyond. 23.
- [28] ELVANG, H., AND HUANG, Y.-T. Scattering Amplitudes. 269.
- [29] ET AL HAGIWARA, K. Review of Particle Physics: Particle data group. *Physical Review D - Particles, Fields, Gravitation and Cosmology* 66, 1 I (jul 2002), 100011–10001958.
- [30] FADIN, V., FIORE, R., KOZLOV, M., AND REZNICHENKO, A. Proof of the multi-Regge form of QCD amplitudes with gluon exchanges in the NLA. *Physics Letters B* 639, 2 (aug 2006), 74–81.
- [31] FADIN, V. S. The gluon Reggeization in perturbative QCD at NLO, nov 2005.
- [32] FADIN, V. S., KOZLOV, M. G., AND REZNICHENKO, A. V. Radiative corrections to QCD amplitudes in quasi-multi-Regge kinematics. *Physics of Atomic Nuclei* 67, 2 (feb 2004), 359–375.
- [33] FORSHAW, J., AND SHAW, D. *Quantum Chromodynamics and the Pomeron*, vol. d. 1997.
- [34] GRAZZINI, M., AND SARGSYAN, H. Heavy-quark mass effects in Higgs boson production at the LHC. *Journal of High Energy Physics*, June 2013 (jun 2013).
- [35] HAHN, T., AND PÉREZ-VICTORIA, M. Automated one-loop calculations in four and D dimensions. *Computer Physics Communications* 118, 2-3 (may 1999), 153–165.
- [36] HIGGS, P. W. Broken Symmetries and the Masses of Gauge Bosons. *Physical Review Letters* 13, 16 (oct 1964), 508–509.
- [37] HÖCHE, S. Introduction to parton-shower event generators. 40.
- [38] HOLMES, S., MOORE, R. S., AND SHILTSEV, V. Overview of the Tevatron collider complex: goals, operations and performance. *Journal of Instrumentation* 6, 08 (aug 2011), T08001–T08001.

- [39] JAROSIK, N., BENNETT, C. L., DUNKLEY, J., GOLD, B., GREASON, M. R., HALPERN, M., HILL, R. S., HINSHAW, G., KOGUT, A., KOMATSU, E., LARSON, D., LIMON, M., MEYER, S. S., NOLTA, M. R., ODEGARD, N., PAGE, L., SMITH, K. M., SPERGEL, D. N., TUCKER, G. S., WEILAND, J. L., WOLLACK, E., AND WRIGHT, E. L. Seven-year Wilkinson Microwave Anisotropy Probe (WMAP) Observations: Sky Maps, Systematic Errors, and Basic Results. *The Astrophysical Journal Supplement Series* 192, 2 (feb 2011), 14.
- [40] LINDERT, J. M., MELNIKOV, K., TANCREDI, L., AND WEVER, C. Top-bottom interference effects in Higgs plus jet production at the LHC.
- [41] OLIVE, K., AND GROUP, P. D. Review of Particle Physics. *Chinese Physics C* 40, 10 (oct 2016), 100001.
- [42] PESKIN, M. E., AND SCHROEDER, D. V. *An Introduction To Quantum Field Theory*, vol. 47. 1995.
- [43] SJÖSTRAND, T., MRENNNA, S., AND SKANDS, P. A Brief Introduction to PYTHIA 8.1.
- [44] SKANDS, P. QCD for Collider Physics.
- [45] SOPER, D. E. Parton distribution functions. *Nuclear Physics B - Proceedings Supplements* 53, 1 (1997), 69–80.
- [46] SREDNICKI, M. Quantum Field Theory. *Quantum* 104 (2007), 129–142.